INTERNATIONAL ATOMIC ENERGY AGENCY
UNITED NATIONS EDUCATIONAL, SCIENTIFIC AND CULTURAL ORGANIZATION
INTERNATIONAL CENTRE FOR THEORETICAL PHYSICS
I.C.T.P., P.O. BOX 586, 34100 TRIESTE, ITALY, CABLE CENTRATOM TRIESTE

H4.SMR/480-19

WORKSHOP ON EARTHQUAKE SOURCES & REGIONAL LITHOSPHERIC STRUCTURES FROM SEISMIC WAVE DATA

19 - 30 November 1990

Observations of Slow Deformation Events and Speculations on their Relationship to Fast Seismic Ruptures

T. H. Jordan

Department of Earth, Atmospheric & Planetary Sciences
Massachusetts Institute of Technology
Cambridge, MA 02139
U.S.A.

Observations of Slow Deformation Events and Speculations on their Relationship to Fast Seismic Ruptures

Notes for Lectures Presented at the International Centre for Theoretical Physics

November 20-22, 1990

by

THOMAS H. JORDAN

Department of Earth, Atmospheric and Planetary Sciences
Massachusetts Institute of Technology
Cambridge, MA 02139 USA

Table of Contents

Summary

These lectures describe some recent research on so-called 'slow earthquakes' and other seismic events characterized by anomalously long durations. In the first lecture, I introduce the subject by reviewing some previous observational work, defining some terminology, and setting up an appropriate phenomenological model for the teleseismic investigation of seismic sources. In the second lecture, I describe a teleseismic procedure for the detection and characterization of anomalous earthquakes using low-frequency free oscillations. The application of this procedure to a continuous, 10-yr record from the International Deployment of Accelerometers (IDA) network of ultra-long-period seismometers has yielded a new catalog of normal-mode excitation events that allows the systematic identification of slow earthquakes on a global scale. It has also led to the discovery of a new kind of teleseism which excites free oscillations but does not generate wave groups observable on long-period or short-period seismograms. Although the provenance of these "quiet earthquakes" is as yet uncertain, the data are consistent with them being tectonic in origin. I describe some novel procedures for locating quiet earthquakes that require no *a priori* estimates of the event hypocenters. Preliminary results show that they are relatively shallow (probably lithospheric), have apparent durations of 200 s or more, occur in a variety of tectonic settings, and are not associated with detectable fast (elastodynamic) ruptures.

In the third lecture, I hypothesize that quiet earthquakes represent episodes of strain release in more ductile parts of the lithosphere, below the seismogenic layer. It is speculated that these unusually slow events may, in some instances, nucleate large, ordinary earthquakes. To test this latter conjecture, I have developed a new methodology for detecting slow precursors to fast ruptures. Results from the preliminary application of this procedure lend credence to the precursor hypothesis. I will examine the implications of these results for dynamical models of slow deformation events and show how further work along these lines may allow seismologists to address the question, "Which earthquakes, if any, are short-term predictable?"

Lecture 1. Episodic Deformation of the Lithosphere: Fast Ruptures, Slow Earthquakes, and Subseismic Events

1.1 Some Definitions. Although motion in the Earth's interior presumably is accomplished by quasi-steady creep, the non-elastic deformation of the lithosphere tends to occur as discrete events localized about some space-time centroid ($\mathbf{r}$, t). The finite size of a deformation event can be measured by a characteristic length L_c and characteristic duration τ_c, defined in terms of the second central moments of the stress-glut-rate tensor [*Backus and Mulcahy*, 1976a,b; *Backus*, 1977a,b]. The particular definitions we shall use are those given in eqns. A13-14 of *Silver and Jordan* [1983], which is reproduced as Appendix A. The ratio of these dimensions defines a characteristic rupture velocity,

$$v_c = L_c/\tau_c \qquad (1)$$

Figure 1 summarizes the distribution of deformation events on a plot of characteristic length versus characteristic time. The most familiar are 'ordinary' earthquakes: elastodynamic cracks propagating at a significant fraction (typically about three-fourths) of the the shear-wave velocity; i.e., at speeds of kilometers per second. It is indicated by a variety of data, however, that deformation events occur over a broad spectrum of temporal and spatial scales, some having characteristic velocities orders of magnitude less than fast elastodynamic ruptures.

In addition to ordinary earthquakes, seismologists distinguish two other types of seismic events: 'slow' and 'silent' earthquakes. Like an ordinary earthquake, a slow earthquake includes one or more episodes of high-speed rupture propagation, so that it produces an ordinary train of high-frequency body waves; however, its overall duration is unusually long relative to ordinary events of comparable total moment, and its level of low-frequency excitation is anomalously high [*Benioff and Press*, 1958; *Sacks et al.*, 1978; *Kanamori and Stewart*, 1979]. Documented examples include the 1946 Aleutians earthquake ($v_c \approx 200$ m/s), which generated a strong tsunami [*Kanamori*, 1972; *Abe*, 1973]; several events on the Gibbs fracture zone [*Kanamori and Stewart*, 1976]; the 6 Jun 60 Chilean transform event, which ruptured for about an hour as a series of earthquakes of relatively small seismic moment ($\sim 5 \times 10^{20}$ Nm) [*Kanamori and Stewart*, 1979]; the Izu-Oshima earthquake of 14 Jan 78 [*Sacks et al.*, 1981]; several oceanic transform fault earthquakes [*Okal and Stewart*, 1982; *Stewart and Okal*, 1983]; the Banda Sea event of 21 Feb 78 [*Silver and Jordan*, 1983]; and the tsunamogenic Peru earthquake of 20 Nov 60 [*Pelayo and Wiens*, 1990].

Silent earthquake is the oxymoron used to designate a deformation event which has no episodes of high-velocity rupture propagation, so that it does not generate teleseismically detectable high-frequency radiation [*Dziewonski and Gilbert*, 1974; *Gilbert and Dziewonski*, 1975; *Yamashita*, 1980; *Bonafede et al.*, 1983]. Hence, silent earthquakes not identified during the routine construction of earthquake catalogs. The documented examples of silent earthquakes include creep episodes along the San Andreas fault in California [*Scholz et al.*, 1969; *King et al.*, 1973], low-frequency signals observed at the Trieste tide station preceding the 1976 Friuli earthquake [*Bonafede et al.*, 1983], and deformation events detected by strainmeters in the near field in Japan [*Sacks et al.*, 1978; *Linde et al.*, 1988].

We arbitrarily choose $v_c = 1$ km/s to distinguish slow earthquakes from ordinary seismic ruptures. Slow earthquakes identified from teleseismic data exhibit characteristic velocities as low as 100 m/s. The characteristic velocities of silent earthquakes determined from near-field observations range from 10 m/s for the Friuli precursors [*Bonafede et al.*, 1983] to 10 mm/s for San Andreas creep events [*Scholz et al.*, 1969; *King et al.*, 1973]. Deformation events with lower characteristic velocities, as slow as 1 mm/s, are estimated to be typical of strain migration [*Kasahara*, 1973; *Rundle*, 1978]. Apparently, deformation of the lithosphere is episodic and complex, with characteristic velocities varying by six orders of magnitude or more. At present, the constitutive equations that govern slow deformation events are not well understood, and the spatial and temporal relationships between slow deformation and fast seismic ruptures are obscure.

By applying a novel detector to the records from the IDA network of ultra-long-period seismometers, we have recently discovered a new class of teleseismic events, earthquakes which excite the earth's low-order free oscillations but do not generate wave groups observable on either long-period or short-period seismograms. We shall call these excitation anomalies "quiet earthquakes" to distinguish them from transseismic slow earthquakes and subseismic silent earthquakes. As discussed in Lecture 2, novel procedures are being developed to locate and analyze quiet earthquakes. Their provenance is as yet uncertain; we cannot yet exclude meteorological disturbances as the cause of some of them, for example. However, the data are consistent with them being tectonic in origin, and we shall adopt this as a working hypothesis. Novel procedures requiring no *a priori* estimates of the event hypocenters are being developed to locate quiet earthquakes. Preliminary results show that they are relatively shallow, probably within the lithosphere, and that they have characteristic velocities on the order of 10-100 m/s. Speculation on the relationship between these unusual events and ordinary fast seismic ruptures is the subject of Lecture 3.

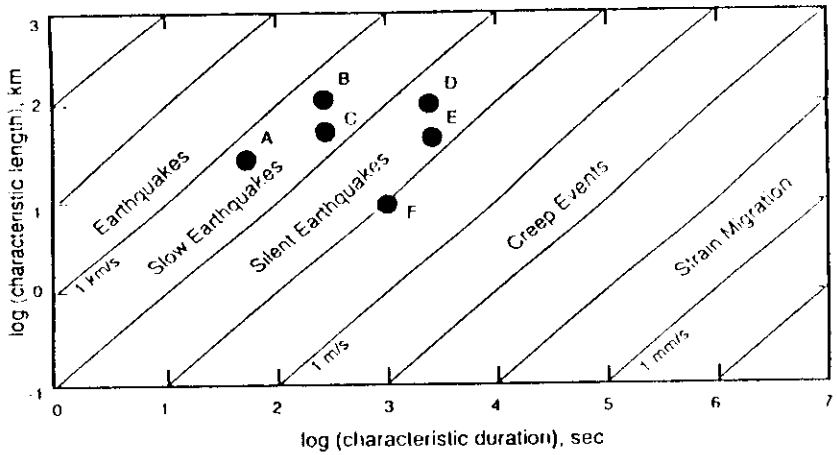

FIGURE 1. A plot of the characteristic time versus characteristic length for lithospheric deformation events. 'Ordinary earthquakes' occur at rupture velocities that are a substantial fraction of the shear wave velocity. Creep events on the San Andreas fault occur at less than 1 m/s and strain migration events occur at less than 1 mm/s. Between main sequence earthquakes and creep events are some documented examples of slow and silent earthquakes. They are **A**, the 21 Feb 78 Banda Sea earthquake [*Silver and Jordan*, 1983]; **B**, the 1896 Sanriku earthquake [*Kanamori*, 1972]; **C**, the 1946 Aleutian earthquake [*Kanamori*, 1972; *Abe*, 1973]; **D**, the 6 Jun 60 Chilean earthquake [*Kanamori and Stewart*, 1979]; **E**, the 14 Jan 78 Izu-Oshima earthquake [*Sacks et al.*, 1981]; and **F**, precursors to the 1976 Friuli earthquake [*Bonafede et al.*, 1983].

1.2 Moment-Tensor Representation. The excitation of low-frequency waves by an earthquake can be represented by its stress glut $\dot{\mathbf{T}}(\mathbf{r},t)$, a second-order tensor density whose integral over the source volume is a time-varying moment tensor $\mathbf{M}(t)$ [*Backus and Mulcahy*, 1976]. We assume the orientation of the moment tensor does not vary with time and adopt the form $\mathbf{M}(t) = \sqrt{2}\, M_I^0\, \hat{\mathbf{M}}\, F(t)$. In this factorization, M_I^0 is the total scalar moment, $\hat{\mathbf{M}}$ is a time-independent source-mechanism tensor with unit Euclidean norm ($\hat{\mathbf{M}}$:$\hat{\mathbf{M}}$ = 1), and $F(t)$ is a scalar-valued time function such that $\lim_{t\to\infty} F(t) = 1$. We consider finite-duration sources with no slip reversals; i.e., we assume that $F(t)$ is zero prior to some starting time t_*, unity after some stopping time $t_* + T$, and nondecreasing (monotone) in the interval $t_* \le t \le t_* + T$. The derivative $f(t) \equiv dF/dt$, if it exists, is called the source time function, and $\dot{\mathbf{M}}(t) = \sqrt{2}\, M_I^0\, \hat{\mathbf{M}}\, f(t)$ is called the moment rate tensor.

1.3 Low-Order Moments of the Source Time Function. Without loss of generality we can choose $t_* = 0$. Then the polynomial moments of the source time function defined by the Lebesgue-Stieltjes integrals

$$\mu_p = \int_0^\infty t^p\, dF(t) \tag{2}$$

are positive, bounded numbers for all $p = 0, 1, 2, \ldots$. By definition, $\mu_0 = 1$. The central moments, defined with respect to the source centroid time $t_1 \equiv \mu_1$,

$$\hat{\mu}_p = \int_0^\infty (t - t_1)^p\, dF(t) \tag{3}$$

are related to the ordinary moments by

$$\hat{\mu}_p = \sum_{q=0}^{p} \binom{p}{q} (-t_1)^{p-q}\, \mu_q \tag{4a}$$

$$\mu_p = \sum_{q=0}^{p} \binom{p}{q} t_1^{p-q}\, \hat{\mu}_q \tag{4b}$$

where the quantity in brackets is a binomial coefficient. The second central moment defines what *Silver and Jordan* [1982] have termed the characteristic duration of the source: $\tau_c = 2\sqrt{\hat{\mu}_2}$. This parameter is the measure of source duration employed in equation (1); the reader is referred to Appendix A for its relationship to other definitions, such as the 'source process time' used by some seismologists. Central moments with $p > 2$ describe the higher-order properties of its time history and are, correspondingly, more difficult to estimate. In Lecture 3, we shall make particular use of the third central moment, $\hat{\mu}_3$, which measures the skewness of the source time function. Equation (3a) yields $\hat{\mu}_3 = \mu_3 - 3t_1\mu_2 + 2t_1^3$.

We have developed methods for estimating the first few polynomial moments of the source time function from the low-frequency, far-field data recorded by ultra-long period seismometers. To describe these methods we introduce the complex Fourier spectrum

$$f(\omega) = \int_{-\infty}^{\infty} e^{-i\omega t}\, dF(t) = |f(\omega)|\, e^{-i\omega\Delta(\omega)} \tag{5}$$

If the time origin corresponds to the start time, i.e. $t_* = 0$, then $\mu_p = i^p(d^p f/d\omega^p)_{\omega=0}$, and the Taylor series expansion of this spectrum about zero frequency is

$$f(\omega) = 1 - i\mu_1\omega - \mu_2\omega^2/2! + \cdots + (-i)^p\mu_p\omega^p/p! + \cdots \quad (6)$$

Because $F(t)$ is real, $f(\omega)$ has Hermitian symmetry, and the two real-valued spectra $|f(\omega)|$ and $\Delta t(\omega)$ are even functions of frequency; hence, their Taylor series expansions about $\omega = 0$ can be written in the form:

$$|f(\omega)| = 1 + f_2\omega^2/2! + f_4\omega^4/4! + \cdots + f_{2n}\omega^{2n}/(2n)! + \cdots \quad (7)$$

$$\Delta t(\omega) = \Delta t_1 + \Delta t_3\omega^2/2! + \cdots + \Delta t_{2n+1}\omega^{2n+1}/(2n)! + \cdots \quad (8)$$

1.4 Total-Moment Spectrum. In the terminology of *Silver and Jordan* [1983], $M_T(\omega) \equiv M_T^0 |f(\omega)|$ is the total-moment spectrum. A little algebra shows that the coefficients in (7) are given by the even-order central moments of $F(t)$ [Appendix A, eqn. 5]:

$$f_{2n} = (-1)^n\hat{\mu}_{2n}, \quad n = 0, 1, 2, \ldots \quad (9)$$

Therefore, the zero-frequency intercept of $M_T(\omega)$ is the total moment released during the event, and the zero-frequency curvature is proportional to the square of its characteristic duration τ_c. We estimate $M_T(\omega)$ from observed seismograms using the procedure developed by *Silver and Jordan* [1982, 1983], described in Appendix A. The data functionals employed by their method are values of the power spectra and cross spectra integrated over discrete frequency bands. The estimation algorithm is optimized to account for errors in the transfer functions due to incorrect earth structure (e.g., aspherical heterogeneity), errors in the assumed source mechanism, and random noise. For large earthquakes ($M_T^0 \geq 10^{19}$ Nm) recorded by the IDA network, 1-mHz averages of $M_T(\omega)$ can be obtained across the frequency band 1 to 11 mHz with standard errors typically less than 20%. *Riedesel et al.* [1986] have applied this method to the 1985 Michoacan earthquakes; their paper is reproduced in Appendix B.

To recover the parameters M_T^0 and τ_c, we follow *Silver and Jordan* [1983] and fit the observations of frequency-dependent moment with an Aki-type spectrum of the form

$$M_T(\omega) = M_T^0 (1 + \omega^2\tau_c^2/8)^{-1} \quad (10)$$

which scales as ω^{-2} at high frequencies. For the earthquakes we have studied, this spectrum provides a fair representation of the total-moment spectra out to 11 mHz. However, it fixes a series of relationships between the second central moment of the source time function, $\hat{\mu}_2 = \tau_c^2/4$, and those of higher even order; i.e.,

$$\hat{\mu}_{2n} = (2n)!\,\hat{\mu}_2^n/2^n, \quad n = 2, 3, \ldots \quad (11)$$

The estimate of τ_c derived from this empirical procedure will thus be conditional on these relationships being correct, at least to some approximation. It can be shown, however, that, if $\tilde{\tau}_c$ is such an estimate, its expected value is bounded by the approximate inequality

$$\langle\tilde{\tau}_c\rangle \leq \tau_c\left[1 + \frac{5}{288}(\omega_{max}\tau_c)^2\right] \quad (12)$$

where ω_{max} is the maximum frequency of the seismic waves employed in the empirical procedure. For example, taking $\omega_{max}/2\pi = 11$ mHz, the actual value used in the data analysis presented below, and a fairly long characteristic duration of $\tau_c = 50$ s, we find that the relative bias in $\tilde{\tau}_c$ is less than ~20% for even the most extreme deviations from our assumed form of the total-moment spectrum.

The total moment at zero frequency, M_T^0, scales as the cube of the characteristic length L_c. Therefore, a plot of τ_c versus M_T^0 can be used to distinguish slow events from ordinary fast earthquakes. The use of such plots for this purpose is illustrated in Figure 20 of Appendix A and Figure 18 of Appendix C. In both of these cases, the scaling between L_c and M_T^0 is that of *Kanamori and Given* [1981].

Lecture 2. A Ten-Year Catalog of Normal-Mode Excitations: Evidence for a New Type of Teleseism

Our knowledge of earth structure can be used to distinguish far-field seismic signals from near-field noise. At most seismic stations, the spectrum of the ambient noise is observed to be a smooth function of frequency. In contrast, teleseismically recorded earthquakes excite ground motion only in very narrow bands centered on the eigenfrequencies of the Earth's normal modes. By observing the spectral levels within these known eigenfrequency bands and comparing them to the spectral levels of ambient noise, it is possible to observe when the normal modes are excited, even if the level of excitation is very small. We have used this fact to develop a sensitive teleseismic detector [*Beroza and Jordan*, 1990a; reproduced as Appendix C].

2.1 Detection of Mode Excitation Events. The detection algorithm is based upon a robust, two-stage statistical test. We consider a particular station in this network having a vertical-component time series $u(t)$ whose complex Fourier transform over a time interval $[t,t+T]$ is $u(\omega)$. As our basic datum, we employ the zeroth-order moment of the Fourier spectrum for a particular fundamental spheroidal mode; i.e., the complex number $a(\omega_l)$ given by the integral of $u(\omega)$ over a bandwidth $2w_l$ centered at frequency ω_l. This spectral averaging enhances coherent signals relative to random noise. In the case of an isolated normal-mode multiplet with an eigenfrequency ω_l and a damping parameter $\omega_l/2Q_l$ whose magnitude is not much larger than w_l, the zeroth moment $a(\omega_l)$ is proportional to the excitation amplitude of the mode but is relatively insensitive to the distortions of the peak shape caused by attenuation [*Gilbert*, 1973] and lateral heterogeneities [*Jordan*, 1978]. Moreover, it can be efficiently computed as a single time-domain integral (see equation 8 of Appendix C).

Suppose the time series $u(t)$ consists entirely of stationary Gaussian noise with zero mean and a power spectrum $\nu^2(\omega)$ which varies slowly with frequency. Then the spectral level in the l^{th} mode band, centered at frequency ω_l, will have an expected value approximately equal to the average of the levels in two noise bands centered at nearby frequencies $\omega_l^- < \omega_l$ and $\omega_l^+ > \omega_l$. We choose the center frequencies ω_l^- and ω_l^+ to be on either side of the resonance peak of interest and compute $a(\omega_l^\pm)$ by integrating the spectrum over the same halfwidth w_l used in the mode bands. When no modes are excited, the random variable

$$\gamma^2 = 2|a(\omega_l)|^2/[\,|a(\omega_l)|^2 + |a(\omega_l^+)|^2] \tag{13}$$

will be governed by an F-distribution with two degrees of freedom in the numerator and four in the denominator. We define γ_α^2 to be the critical value for the $100\alpha\%$ upper tail of $F(2,4)$ and reject the null hypothesis $H_0 \equiv$ {the spectral level in the mode band $\omega_l \pm w_l$ is due only to random noise} in favor of the alternative $H_1 \equiv$ {the mode has been excited by a seismic event} when

$$\gamma^2 > \gamma_\alpha^2 \tag{14}$$

If our assumptions about the noise statistics are justified, then the probability of making a Type-I error (false positive) is α, and we say that H_0 is tested against H_1 at the $100(1-\alpha)\%$ confidence level.

The probability of making a Type-I error is a parameter we are free to choose. By making simple assumptions about the behavior of γ^2 in the presence of the signal, we can also calculate the probability β of failing to detect an excitation when one has occurred; i.e., a Type-II error, or false negative. The Type-II error rate β depends strongly on the signal-to-noise ratio (snr) R. For a specified value of α, we define the detectability threshold R_d to be the value of the snr at which $\beta = .5$; that is, R_d is the excitation level when half of the anomalous events are detected and half are not. At the 99.9% confidence level ($\alpha = .001$), the detectability threshold is $R_d = 8.5$ for a single mode recorded at a single station.

A mode-excitation detector can be made more powerful and more robust by requiring that a particular mode be simultaneously detected by a subset of seismic stations in a global network. Our algorithms for mode and event detection by a network are formulated in terms of sums across an array of zeros and ones I_{ilp}, which we call the detection matrix. When a detection is registered at the $100(1-\alpha)\%$ confidence level in the lth mode band for some time interval $[t_i, t_i+T_l]$ recorded by the pth station, then I_{ilp} is assigned a value of unity; otherwise, it is set at zero. Suppose there are N_{il} stations available for fixed i and l. If the time series is dominated by noise, then the sum

$$J_{il} = \sum_{p=1}^{N_{il}} I_{ilp} \tag{15}$$

will be a sample of a binomially distributed random variable with sample size N_{il} and success probability α. We say the network has detected the excitation of the lth mode at time t_i at the $100(1-\alpha')\%$ confidence level if J_{il} exceeds the critical value for the $100\alpha'\%$ upper tail of this binomial distribution.

Because decisions are made on the basis of a summed-score statistic rather than, say, a sum over γ^2, the network mode detector is more robust with respect to nonstationarity and non-Gaussian behavior of the noise. Moreover, we place at our disposal the parameter α, which can be set at the value that minimizes the Type-II error level β' for a specified Type-I error level α' and snr R. This optimization procedure is discussed in Appendix C. The value we choose is $\alpha = 0.5$, near the optimum for the range of parameters encountered in our work with IDA data. For $\alpha' = .001$, the network detectability threshold for a single mode is $R_d' = 1.7$, a factor of five reduction from the single-station/single-mode case.

A time-localized seismic event will excite modes across a broad frequency spectrum. To test for significant seismic activity localized near a time t_i, we sum the detection matrix over all N_{il} stations and all observed modes between a lower cutoff l_{min} and an upper cutoff l_{max}:

$$K_i = \sum_{l=l_{min}}^{l_{max}} J_{il} = \sum_{l,p} I_{ilp} \tag{16}$$

If each element in the sum is an independent random variable, then K_i is binomially distributed with sample size

$$N_i = \sum_{l=l_{min}}^{l_{max}} N_{il} \tag{17}$$

and success probability α. We say the network has detected an event at time t_i at the $100(1-\alpha'')\%$ confidence level if K_i exceeds the critical value for the $100\alpha''\%$ upper tail of the binomial distribution. (As discussed in Appendix C, practical considerations dictate that the noise bands for adjacent modes overlap, which introduces correlations among elements of the detection matrix, and the distribution law for K_i is not binomial but must be calculated using Markov statistics.)

In the case of a 10 station network recording 36 modes with equal snr ($N_i = 360$), the detectability threshold for $\alpha' = .001$ is $R_d'' = 0.51$. This represents a gain of 3.3 over the network/single-mode example and a gain of 17 over the single-station/single-mode example

quoted above. Hence, using seismic networks of only modest size, we can detect an even having an snr less than unity with very little risk of making a false detection. Theoretica calculations and numerical experiments with both real and simulated data sets (Appendix C indicate that fundamental spheroidal modes recorded at frequencies less than 5 mHz by a sparse (~10-station) network of vertical-component seismometers can achieve a magnitude detection threshold of $M_W \approx 6.0$, corresponding to a seismic moment of $\sim 1 \times 10^{18}$ Nm The spheroidal modes excited by an event of this magnitude have signal-to-noise ratios tha are less than unity, so it is possible to detect mode-excitation events that are not obvious from a visual inspection of individual records.

2.2 Application to IDA Data. The detector has been applied at 3-hr intervals to a full decade (1978-87) of IDA network data [*Beroza and Jordan*, 1990b]. By trying to associate individual mode-excitation events in this catalog with earthquakes in the ISC and Harvard CMT catalogs, we can search systematically for anomalous events. Over the entire ten-year period, we register a total of 1503 distinct mode-excitation events. Of these, 1339 can be plausibly associated with earthquakes in the ISC or CMT catalogs. A subset of these events shows an anomalously strong excitation of the Earth's free oscillations. A more detailed analysis of their low-frequency spectra indicates that these are slow earthquakes with unusually low characteristic velocities, as determined from the M_T^0-τ_c scaling discussed in Lecture 1. Many of these slow earthquakes occur on oceanic transform faults, which is consistent with the results of previous workers [e.g., *Kanamori and Stewart*, 1976, 1979; *Okal and Stewart*, 1982; *Stewart and Okal*, 1983]. Further work on the temporal characteristics of slow earthquakes such as these will be the subject of Lecture 3.

Over the 10-year period we would expect to register ~29 false positive detections. Instead, we find 164 mode-excitation events that are not associated with cataloged seismicity of sufficient size to explain the detections. It is not yet certain what these anomalous excitations represent. Theoretical and empirical estimates of the detection threshold fluctuate about an average level of $M_W \sim 6.0$, which argues against the possibility that the excitations are due to regular earthquakes with fast seismic rupture that are not located by the ISC. One possibility is that some are caused by the meteorological generation of seismic waves, such as when a major storm hits a coastline. A more likely explanation is that they are caused by slow seismic rupture: either slow events with very low instrumental magnitudes, or slip events of large seismic moment with very low characteristic velocities, significantly less than for typical slow earthquakes. We shall adopt this hypothesis for the remainder of our analysis.

2.3 Analysis of Excitation Anomalies. The upper panel of Figure 2 shows the detection diagram for the month of October, 1980. In addition to the usual run of ordinary large earthquakes there are two excitations significant at the 99.9% level which are unassociated with Harvard CMT solutions. The first corresponds to a M_S 5.7 earthquake in the New Britain region identified by the ISC but not incorporated into the CMT catalog. The size of the mode-excitation peak indicates that this event is probably a slow earthquake, and we have confirmed this hypothesis using the M_I^0-τ_c analysis procedures. There is no obvious cataloged event associated with the second anomaly, and this event may be a quiet earthquake.

A third excitation peak, on 22 Oct 80, is incorrectly associated with a very small (m_b 5.0) Borneo event at 14:00 on 23 Oct for which Harvard obtained a CMT solution. Instead, it appears to be generated by a slow earthquake on the Chile Rise at 23:00 on 22 Oct 80, located by the ISC but not analyzed by Harvard.

To obtain an independent epicenter for this and other excitation anomalies, we have developed a new location procedure that uses only information from the low-frequency (< 5 mHz) mode band. Like in the detection algorithm itself, the basic data functional employed by this procedure is $a(\omega_l)$, the integral of the Fourier spectrum over a narrow band centered on the degenerate eigenfrequencies. For fundamental modes, the dependence of $a(\omega_l)$ on epicentroidal distance Δ_1 and centroid time t_1 has the asymptotic form

$$a(\omega_l) \sim \exp[\, i|(l+1/2)\Delta_1 + \zeta_l + \omega_l t_1|] \qquad (18)$$

where ζ_l is a source term that depends on the event mechanism and depth. For shallow-focus earthquakes, ζ_l will not be a strong function of angular degree l. We have constructed a search procedure which assumes ζ_l to be constant over the band 1-5 mHz and determines the centroid time t_1 and epicentral coordinates $[\theta_1, \phi_1]$ by maximizing the cross-correlation of the theoretical sequences from equation (18) with the actual sequences $\{a(\omega_l) : l = 8\text{-}43\}$ observed at many stations. This method has the advantage that the nonlinearities are much less severe than those encountered when theoretical time series are cross-correlated with data time series (as in the CMT location procedures, for example). Its disadvantage is that the epicentroid obtained is not very precise (errors of ± 500 km are not uncommon). However, once a preliminary location has been obtained by this robust procedure, a refined solution can be sought using standard linearized, phase-sensitive methods.

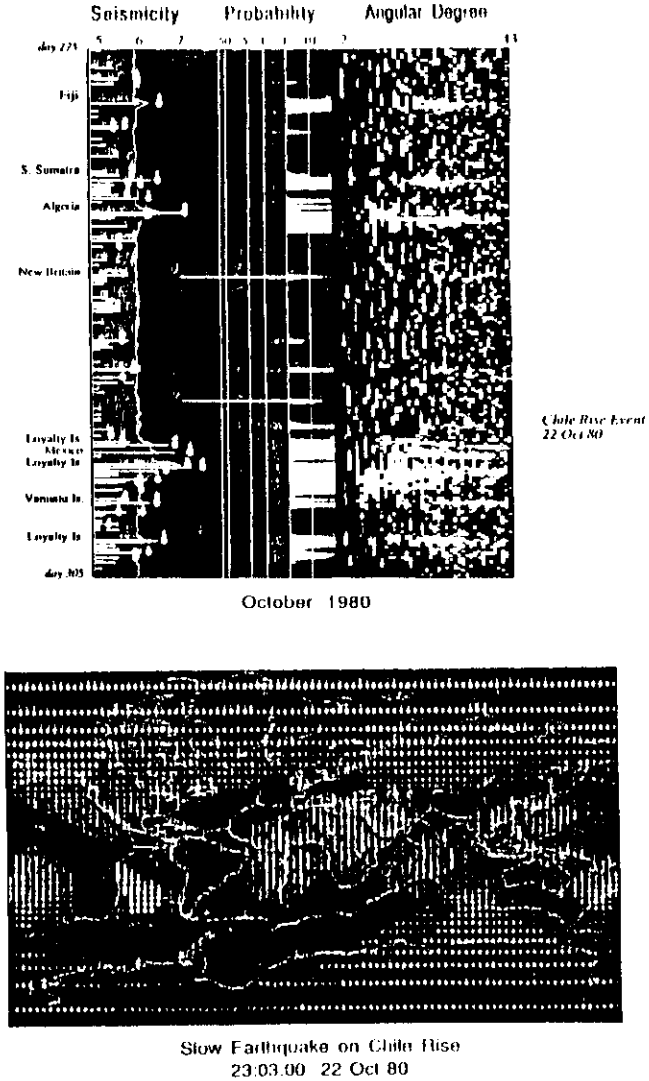

FIGURE 2. *Top.* Detection diagram for October, 1980. Time increases from top to bottom. Right panel shows the excitation confidence level of individual spheroidal modes ${}_0S_2$-${}_0S_{43}$ as determined from the IDA network; excitations with confidence levels greater than 50% are colored blue, with lighter shades corresponding to higher values. Middle panel is a plot of the probability that the excitation observed over the modes ${}_0S_8$-${}_0S_{43}$ at all stations is due to random noise. Values below the 0.1% line – excitation peaks significant at the 99.9% level – are registered as detections and shaded yellow. Left panel shows the event magnitudes from the ISC (white lines) and CMT (dots) seismicity catalogs. Yellow dots represent CMT events associated with significant excitation peaks according to the criteria given in *Beroza and Jordan* [1990]; red dots are unassociated events, and white dots are "unassociatable" because of signal interference with a larger event. Green field indicates nominal detection threshold for ordinary (fast) earthquakes. Unassociated mode excitation detections are flagged by a question mark. *Bottom.* Location peak (yellow) obtained for the Chile Rise slow earthquake of 22 Oct 80 using the phase insensitive, nonlinear location procedure discussed in the text. Once this crude location is obtained, the event can be located using a standard phase sensitive, linearized method, such as the CMT technique of *Dziewonski et al.* [1980].

The lower panel of Figure 2 shows the results for the 22 Oct 80 excitation peak. As anticipated, it does indeed locate on the Chile Rise, confirming our hypothesis that the ISC-located earthquake was a very slow event. The centroid time t_1 determined by our procedure is 23:03, three minutes later than the high-frequency origin time. (It is interesting to note that a second small earthquake occurred 27 min later at a position 300 km to the west, suggesting that the slow deformation event propagated along the transform fault at a velocity of ~200 m/s.) Figure 3 shows the time series for this event at six of the quieter IDA stations. During the first several hours following the event, distinct Rayleigh-wave packets can be clearly seen as "high-frequency" arrivals (out to R_5-R_6 at the low-noise station GAR, which is nearly antipodal). A power spectrum stacked over these same six stations (lower panel of Figure 3) shows energy in the fundamental spheroidal modes. The SNR is especially high in the 4-5 mHz band; it is this energy which builds up the Rayleigh wave groups evident on the time series.

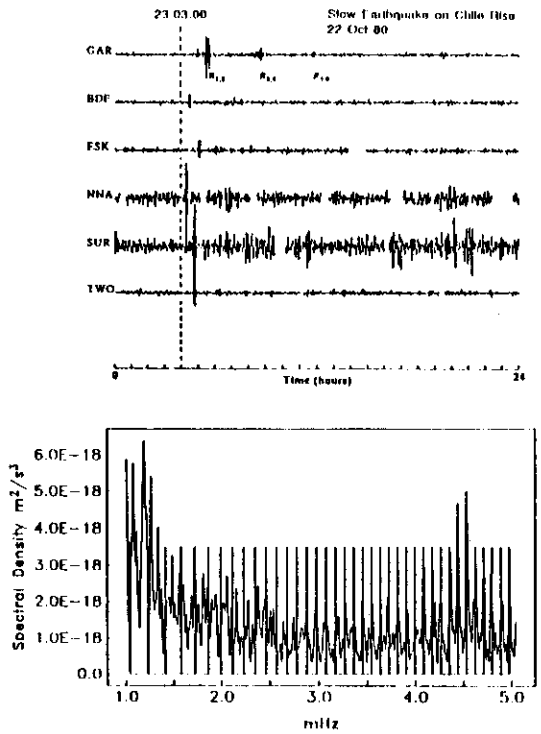

FIGURE 3. Time series (top) and the stacked power spectrum (bottom) at six IDA stations for the Chile Rise slow earthquake of 22 Oct 80. The centroid time determined by our low-frequency location procedure is 23:03. Distinct Rayleigh-wave packets can be clearly seen as "high-frequency" arrivals following this time; these are marked on the GAR record, which is nearly antipodal. The power spectrum stacked over these same six stations shows energy in the fundamental spheroidal modes; the SNR is especially high in the 4-5 mHz band, which corresponds to the wave groups evident on the time series. Degenerate eigenfrequencies for ${}_0S_6$-${}_0S_{43}$ are indicated by the vertical lines.

The top panel of Figure 4 is the detection diagram for July, 1978. Near the end of this month there is a strong, double-peaked mode excitation event which occurs during a period almost devoid of seismicity: the largest ISC-recorded earthquake in the one-day interval centered on the excitation peak is a M_S 4.4, shallow focus event in central Italy. Applying our location procedure to the IDA data yields an epicentroid in a mid-plate region off the southwest coast of Africa (Figure 4, lower panel) and a centroid time of 23:21:00 on 29th July. A plot of the IDA time series (Figure 5, top) shows no obvious surface-wave packets, but the power stack (Figure 5, bottom) reveals well excited fundamental spheroidal modes across the 2-5 mHz band.

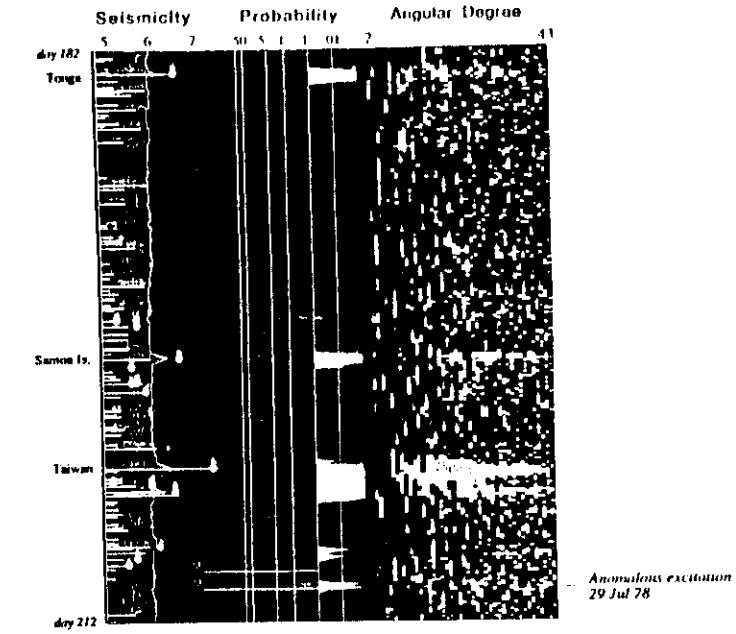

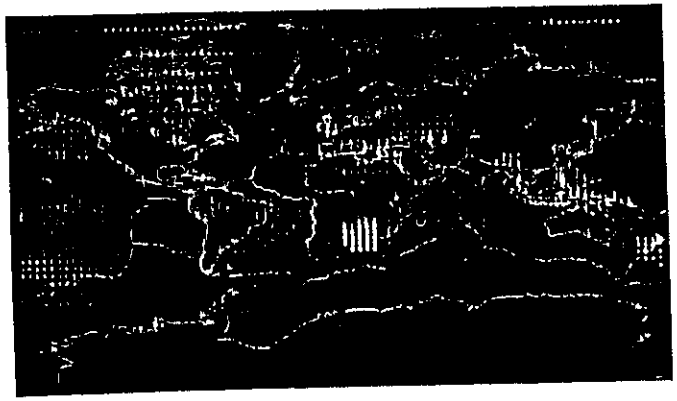

FIGURE 4. *Top.* Detection diagram for July, 1978, plotted according to the conventions of Figure 2. The anomalous excitation of 29 Jul 78 is marked. *Bottom.* Location peak (yellow) obtained for the excitation anomaly of 29 Jul 78 using the nonlinear location procedure discussed in the text. The ISC and CMT catalogs detected no earthquake at this location and time, indicating that the excitation anomaly corresponds to a "quiet" event with a very long characteristic duration.

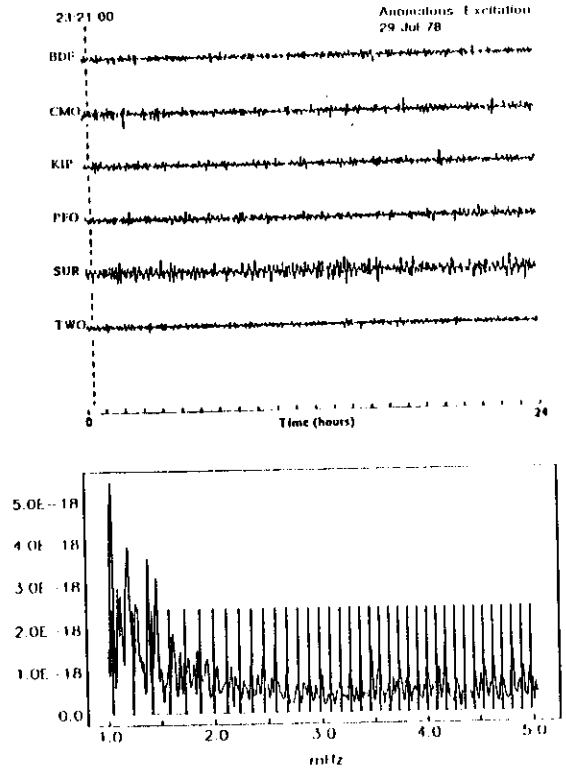

FIGURE 5. *Top.* Time series at six IDA stations for the excitation anomaly of 29 Jul 78. The centroid time determined by our low-frequency location procedure is 23:21. No distinct Rayleigh or body waves can be seen following this time on either these records or higher frequency GDSN seismograms. *Bottom.* The power spectrum stacked over these same six IDA stations shows energy in the fundamental spheroidal modes across the 2–5-mHz band. Degenerate eigenfrequencies for ${}_0S_6$–${}_0S_{43}$ are indicated by the vertical lines.

Therefore, we identify the 29 Jul 78 event as a quiet earthquake. We have not yet had the opportunity to refine the location of this event or determine its mechanism, and until we have some corroboration using phase-sensitive methods, the location shown in Figure 4 should be considered tentative. In particular, we are suspicious that the mid plate location for this event is spurious.

We have done some experimentation with synthetic seismograms, however, and the results allow us to draw the following conclusions:

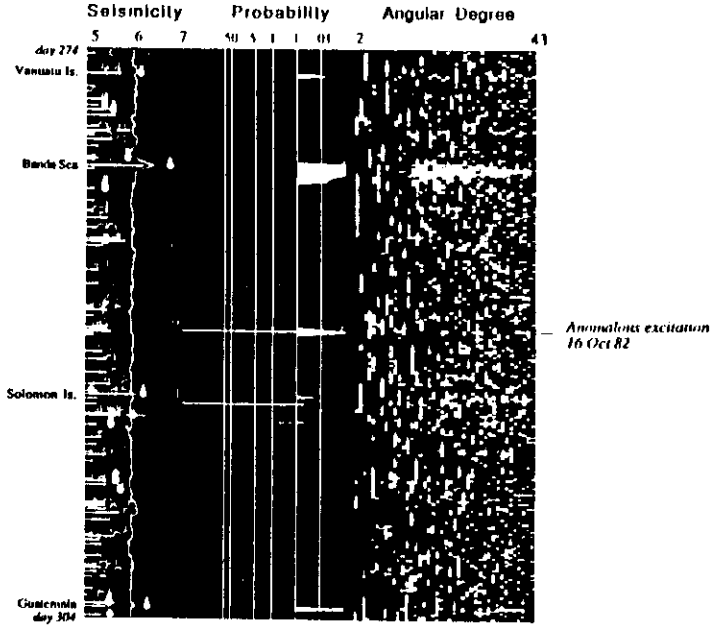

October 1982

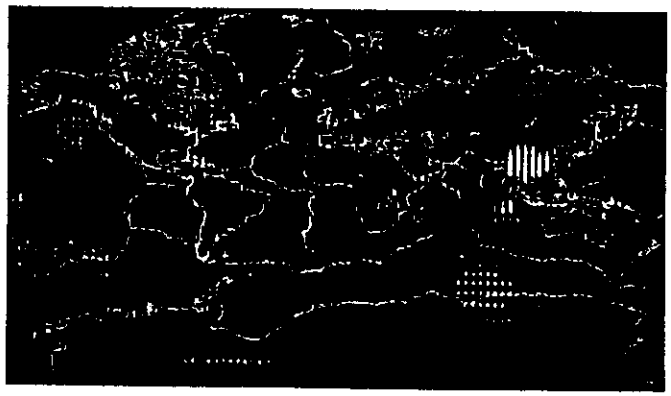

Anomalous Excitation
01:15:00 16 Oct 82

FIGURE 6. *Top*. Detection diagram for October, 1982, plotted according to the conventions of Figure 2. The anomalous excitation of 16 Oct 82 is marked. *Bottom*. Location peak (yellow) obtained for the excitation anomaly of 16 Oct 82 using the nonlinear location procedure discussed in the text. The ISC and CMT catalogs detected no earthquake at this location and time, indicating that the excitation anomaly corresponds to a "quiet" event with a very long characteristic duration.

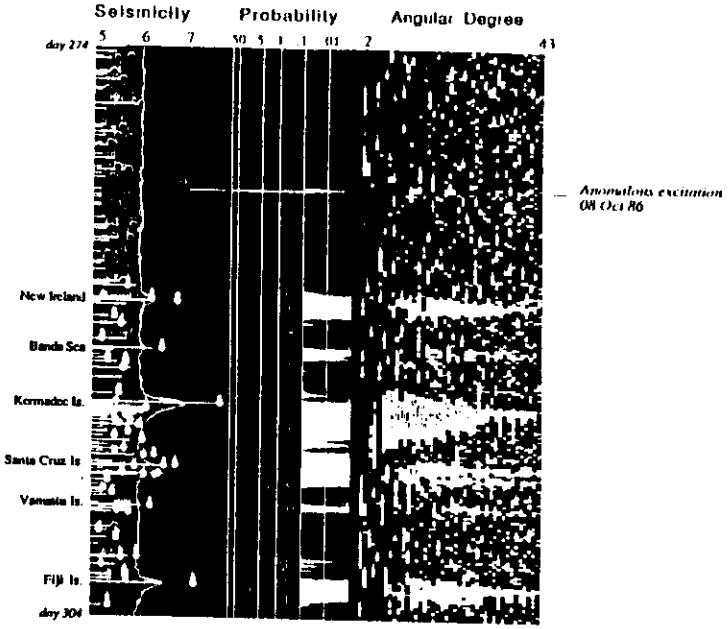

October 1986

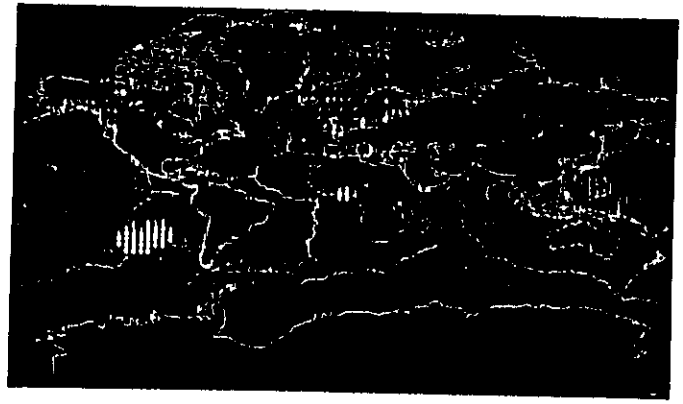

Anomalous Excitation
11:48:00 08 Oct 86

FIGURE 7. *Top*. Detection diagram for October, 1986, plotted according to the conventions of Figure 2. The anomalous excitation of 08 Oct 86 is marked. *Bottom*. Location peak (yellow) obtained for the excitation anomaly of 08 Oct 86 using the nonlinear location procedure discussed in the text. The ISC and CMT catalogs detected no earthquake at this location and time, indicating that the excitation anomaly corresponds to a "quiet" event with a very long characteristic duration.

We have done some experimentation with synthetic seismograms, however, and the results allow us to draw the following conclusions:

- The relatively strong excitation of fundamental spheroidal modes at frequencies > 3 mHz compared to lower frequencies, in conjunction with the lack of observable body-wave groups, indicates that the hypocentroid of the event is probably in the upper 300 km of the earth and is likely to be within the upper lithosphere.

- The level of mode excitation in conjunction with the lack of visible Rayleigh-wave groups can be reproduced on synthetic spectra and time series, but for sources with asymptotic roll-off rates of ω^3 or less, only if the characteristic source duration τ_c is greater than ~200 s.

These inferences, like our preliminary locations, should be considered tentative until they can be corroborated by a more refined analysis of this and other hypothesized quiet earthquakes. Such an analysis is currently underway at MIT.

Figures 6 and 7 show detection and location diagrams for two other quiet earthquakes, 16 Oct 82 and 08 Oct 86. Again, there are clear mode excitations observable in the power spectra but no wave groups observable on the time series. The 16 Oct 82 event locates is Southeast Asia, and the 08 Oct 86 event near the Easter Island triple junction. Neither epicentroid is very reliable, and the sidelobes on the location diagram of the second are particularly large; we reiterate the need for additional work on the location problem. Nevertheless, these preliminary results and those for additional events suggest that quiet earthquakes may occur in a variety of tectonic settings.

Many quiet-earthquake candidates have been identified by our detector, and most of these are eligible for future study. A overview of the ten-year catalog is displayed in Figure 8. The top panel shows a time line punctuated by the 1503 CMT earthquakes that have been associated with mode-excitation events. As discussed in Appendix C, the 50% detection threshold for ordinary earthquakes is $M_W \approx 6.0$. The bottom panel shows the 164 excitation anomalies that cannot plausibly be explained by either ordinary or slow earthquakes; i.e., those for which neither the CMT or ISC catalog yields candidate earthquakes. At the 99.9% confidence level chosen to specify the false-positive error rate, we would expect fewer than 30 of these to be spurious; hence, many, if not most, of the anomalies may be quiet earthquakes.

Quiet earthquakes could contribute substantially to plate-tectonic deformations. Since we can only put a lower bound of ~200 s on the duration of a typical quiet earthquake (and then only assuming a spectral roll-off rate), we can fix only a lower bound of $\sim 2 \times 10^{18}$ Nm on the moment released by such an event. Clearly, if the time constants are larger, the event will radiate less energy into the mode band, and the moment release may be

substantially larger. Moreover, there are at least three reasons why the number of anomalies shown in Figure 8 is likely to severely underestimate the actual number of quiet earthquakes: (1) Much of the ten-year period is not available for detections owing to interference by large, ordinary earthquakes. (2) Because the confidence level for picking an excitation is very high, the false-negative error rate will be high. (3) Our event association algorithm is very conservative [see Appendix C], so that some of the excitation anomalies caused by quiet earthquakes will be incorrectly assigned to ordinary events. Consequently, it is plausible that the number of quiet earthquakes big enough to significantly excite free oscillations during 1978-87 is several times larger than the number shown in Figure 8.

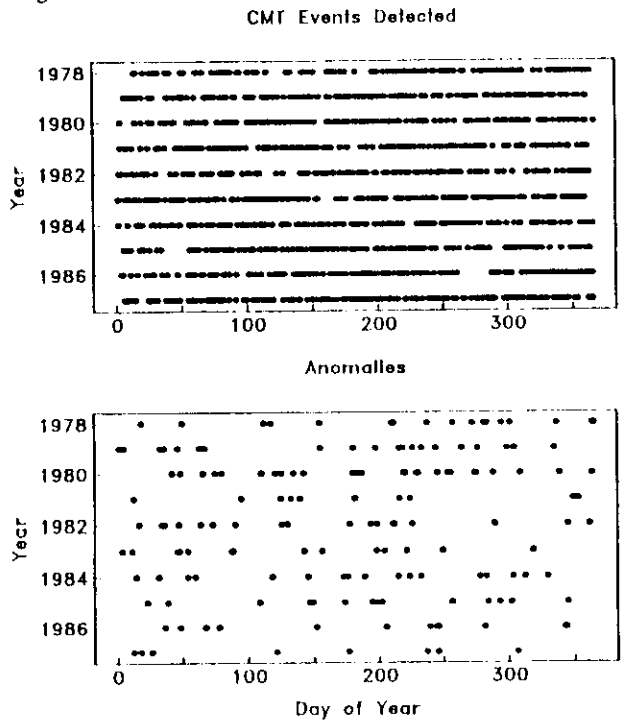

FIGURE 8. *Top.* Time line for the decade 1978-87 showing the 1503 earthquakes listed in the CMT catalog that were identified as significant mode-excitation events by the Berroza-Jordan detector. At the 99.9% confidence level employed in this analysis, the 50% detection threshold for the IDA network for most of this period was $M_W \approx 6.0$. *Bottom.* Time line for the decade 1978-87 showing the 164 anomalous excitations detected at the 99.9% confidence level that could not be associated with significant earthquakes in either the CMT or ISC catalogs. Since fewer than 30 false-positive errors are expected for this period, most of these anomalies may by quiet earthquakes similar to the 29 Jul 78 excitation event. Further analysis of these events is proposed for the next two years.

Lecture 3: Slow Precursors to Fast Seismic Ruptures and their Implications for Earthquake Prediction

3.1 Some Working Hypotheses. Our detection and subsequent analysis of normal-mode excitation anomalies has suggested the following hypothesis:

Hypothesis 1. Low-velocity deformation events (episodes of accelerated creep) occur within the lithosphere with characteristic time scales too long to radiate significant high-frequency seismic energy, but short enough to excite low-frequency free oscillations; that is, there are 'quiet' earthquakes which propagate with characteristic velocities of 10-100 m/s.

We return now to the problem of slow earthquakes; i.e., events which produces an ordinary train of high-frequency body waves, but whose overall duration is unusually long relative to ordinary earthquakes of comparable total moment [e.g., *Sacks et al.*, 1978; *Kanamori and Stewart*, 1979]. What is a slow earthquake? As we and others have shown [Appendix C], slow earthquakes are very common on a global scale, but it must be admitted that their mechanics is not well understood (see the recent book by *Scholz* [1990] for a review). In the light of our discovery of quiet earthquakes, we believe the most plausible explanation is that they are 'compound' events; that is,

Hypothesis 2. Slow earthquakes occur when a quiet earthquake (creep episode) accompanies an ordinary earthquake (high-velocity rupture) of comparable moment.

One possible geometry is to locate the creep component in a plastic layer ('plastosphere' of *Scholz* [1990]) below the brittle-ductile transition that delimits the seismogenic layer (Scholz's 'schizosphere'), as illustrated in Figure 9.

If this conjecture is true, then it is conceivable that, in some instances, a low-velocity deformation event of significant moment may precede and thus initiate the ordinary fast rupture, in which case the latter is said to have a slow precursor. We therefore erect, and seek to test, the following hypothesis:

Hypothesis 3. Quiet earthquakes are precursors to some large ordinary earthquakes.

This hypothesis bears directly on the problem earthquake prediction, because near-field observations of slow precursors, e.g. by geodetic methods, offer one hope for short-term earthquake prediction. No such precursors have yet been detected by near-field methods for intermediate-size earthquakes in California ($M_W \leq 7.1$), implying that the nucleation zones for such events are typically small [*Scholz*, 1990]. It would be imprudent

to generalize this conclusion to other regions, or even to assert it too categorically for California, however, because the amount of data thus far collected is small and only a handful of significant events have been sampled. The problem is that few seismically active regions are well equipped with the appropriate near-field instrumentation. A long observation period will be required before enough data on nearby earthquakes are available to understand the frequency and size statistics of slow precursors, especially for large, infrequent events.

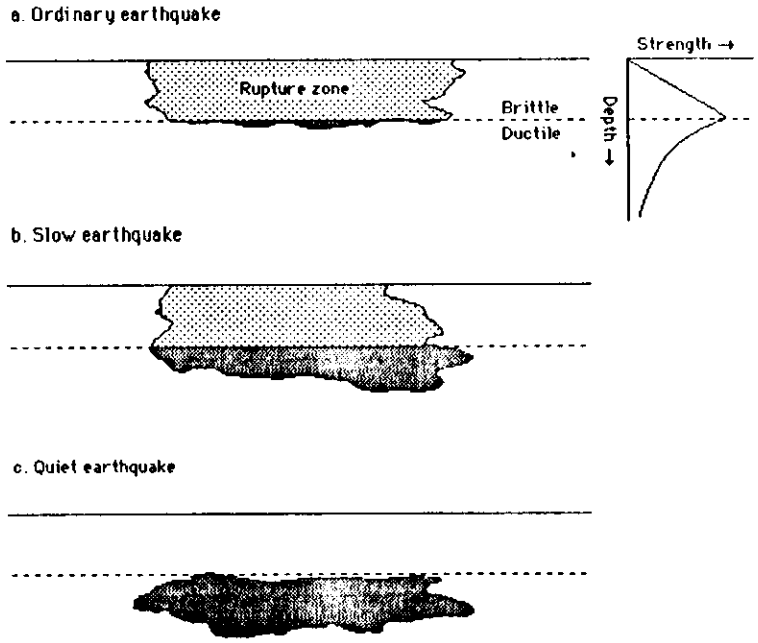

FIGURE 9. Three types of seismic events. (*a*) Ordinary earthquake: a fast rupture propagating as an elastodynamic crack in the brittle (seismogenic) layer. (*b*) Slow earthquake: a compound event comprising a fast rupture in the brittle layer and a creep event of comparable moment in the plastic layer below the brittle-ductile transition. (*c*) Quiet earthquake: an accelerated creep event in the plastic layer that does not initiate a fast rupture in the brittle layer.

3.2 Teleseismic Detection of Slow Precursors to Fast Seismic Ruptures. We would like to be able to detect if fast seismic ruptures have slow precursors using only *far-field* radiation, because such a far-field analysis can be applied to a much larger, global sample of seismic activity, and the dependence of precursory moment release on earthquake size, tectonic region, seismic history, etc., could be assessed without having to wait for several earthquake cycles to occur in a particular region. The utility of far-field analysis of the precursor problem has been indicated by several previous studies. Slow precursors have been identified for the great 1960 Chilean earthquake [*Kanamori and Cipar*, 1974; *Cifuentes and Silver*, 1989] and, with less certainty, for the large 1963 Peru-Brazil and 1970 Columbia deep-focus events [*Gilbert and Dziewonski*, 1975].

The author has developed a technique for the detection of slow precursors at teleseismic distances, based on observations of the earth's free oscillations [*Jordan*, 1990]. The far-field source model is that introduced in Lecture 1. It is assumed the volume-integrated moment-rate tensor can be factored in the form $\dot{\mathbf{M}}(t) = \sqrt{2}\, M_T^0\, \hat{\mathbf{M}}\, f(t)$, where M_T^0 is the total scalar moment, $\hat{\mathbf{M}}$ is a time-independent source-mechanism tensor with unit Euclidean norm, and $f(t)$ is a scalar-valued source time function. We consider finite-duration sources with no slip reversals; i.e., we assume that $f(t)$ is zero prior to some starting time t_* and nonnegative for $t_* \le t$. According to our definitions, the zeroth polynomial moment of $f(t)$ is unity, $\mu_0 = 1$, and its first polynomial moment defines the centroid time $\mu_1 = t_1$. The second central moment of $f(t)$ about this centroid time defines an event's characteristic duration: $\tau_c = 2\sqrt{\hat{\mu}_2}$.

An earthquake is said to have a slow precursor if its starting time t_* occurs significantly before t_0, the origin time of the event determined from high-frequency P waves. The technique for detecting a slow precursor is based on the observation that the low-order polynomial moments of $f(t)$ cannot be specified independently; rather, their relative values are constrained by certain inequality relationships deeply rooted in functional analysis. In particular, a theorem due to Stieltjes [1894] implies that if $t_0 = t_*$ (no precursor), then the time parameters must satisfy the inequality

$$\tau_c \;<\; 2\Delta t_1 \left(1 + (1 + 4\hat{\mu}_3/\Delta t_1^{\,3})^{1/2} \right)^{1/2} \tag{19}$$

where $\Delta t_1 = t_1 - t_0$ is the shift of the centroid relative to the high-frequency origin time and $\hat{\mu}_3$ is the third central moment of $f(t)$, which measures its skewness. If it can be shown that

the data for a particular event are inconsistent with this inequality, then we have a basis for hypothesizing the existence of a slow precursor.

The quantities t_1, τ_c, and $\hat{\mu}_3$ can be bounded from the analysis of low-frequency seismic waves in such a way that this hypothesis test can be usefully applied to real earthquakes. The recovery of the source duration τ_c from the total-moment spectrum $M_T(\omega)$ has been discussed in Lecture 1 (see also Appendices A and B). The two other parameters Δt_1 and $\Delta t_3 = -\hat{\mu}_3/3$ (cf. eqn. 8) are obtained from the zero-frequency intercept and curvature of the time-shift spectrum $\Delta t(\omega)$. We estimate $\Delta t(\omega)$ using a narrow-band cross-correlation method developed by M. A. Riedesel and T. H. Jordan [unpublished manuscript; see *Riedesel and Jordan*, 1989]. We then fit this spectrum with a function of the form

$$\Delta t(\omega) \;=\; \Delta t_\infty + (\Delta t_1 - \Delta t_\infty)\, (\xi/\omega) \arctan \omega/\xi \tag{20}$$

which rolls off at high frequencies as ω^{-1} and satisfies appropriate causality constraints (provided Δt_1 and Δt_∞ are greater than t_*, which, by hypothesis, equals t_0). Equation (8) yields $\hat{\mu}_3 = 2(\Delta t_\infty - \Delta t_1)/\xi^2$.

The primary problem encountered in the recovery of the time-shift spectrum by this (or any other) technique is aspherical heterogeneity. We have found that our spectral integration procedures reduce the sensitivity to heterogeneity to the point where averaging the spectral estimates over a 15-station network yields estimates precise enough to be useful in testing for slow precursors. It is clear, however, that much additional work can be done to account for asphericities; we can, for example, incorporate transfer functions computed from laterally heterogeneous earth models into our processing scheme.

3.3 Application to IDA Data. In a preliminary study, we have applied our slow-precursor detector to a sample of 29 large earthquakes recorded by the IDA Network over the last decade. Some events have time parameters that are consistent with moment release beginning at the high-frequency origin time. These include the 1985 Michoacan main shock and principal aftershock and the 1987 Superstition Hills earthquake. The latter is constrained by near-field recordings to have very little precursory strain release, and the fact that it shows no teleseismic evidence for a slow precursor is a check on the method. However, we have found that other events appear to fail the Stieltjes test given by equation (19) and are thus suspected to have slow precursors. A plot of τ_c versus Δt_1 for these events is given in Figure 10. The earthquakes which fail the test are typically those with high values of the ratio $\alpha = \tau_c/\Delta t_1$. In the case where the skewness $\hat{\mu}_3$ is small or

negative, i.e. the time-shift spectrum is fairly flat or curves upward, the Stieltjes test requires that $\alpha < 2\sqrt{2}$.

An example of an event which appears to have a slow precursor is the Peru-Ecuador intermediate-focus earthquake of April 12, 1983. It has a very large characteristic duration, $\tau_c = 70 \pm 3$ s (Figure 11, *upper panel*) and a small centroid time shift, $\Delta t_1 = 5.1 \pm 1.5$ s (our estimate is almost identical to Harvard's CMT solution), but it shows no obvious frequency variation in its time-shift spectrum (Figure 11, *lower panel*), indicating that $\hat{\mu}_3$ is small. In fact, in order to satisfy the Stieltjes condition, $\Delta t(\omega)$ would have to decrease by more than 20 s between 1 and 11 mHz, which is not consistent with the data. Examination of IDA, GDSN and RSTN records reveals no obvious precursor on the time series. Therefore, we hypothesize that the fast rupture was in this case preceded by a quiet earthquake of the sort discussed in the previous section.

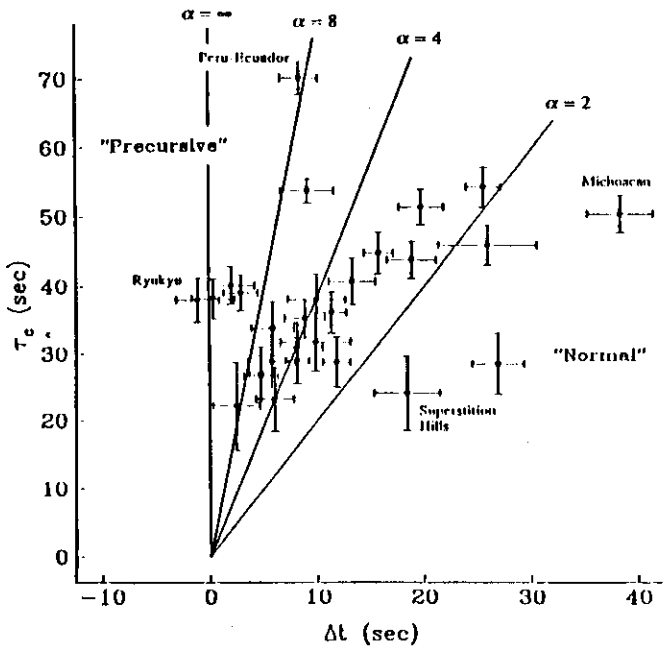

FIGURE 10. Plot of characteristic duration τ_c versus centroid time shift Δt_1 for 29 large earthquakes recorded by the IDA network between 1977 and 1987. Events with large values of $\alpha = \tau_c/\Delta t_1$ are candidates for having slow precursors. Examples of events which formally fail the Stieltjes condition given by *Jordan* [1990] are the 12 Apr 83 Peru-Ecuador and 4 Jul 82 Ryukyu earthquakes.

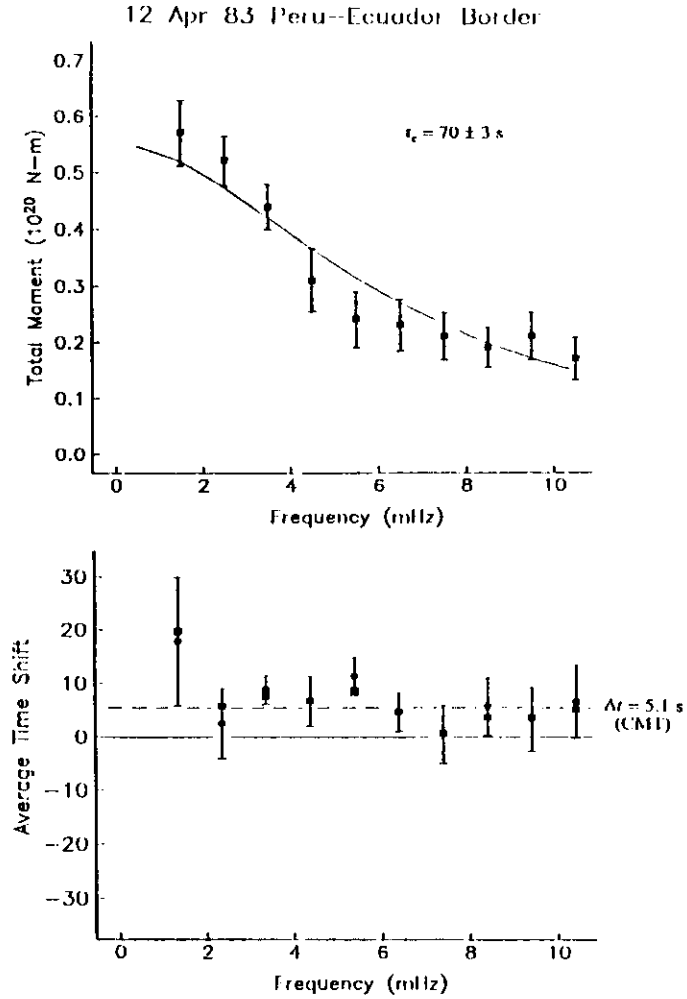

FIGURE 11. *Top.* Total-moment spectrum $M_3(\omega)$ for the 12 Apr 83 Peru-Ecuador earthquake, calculated by the method of *Silver and Jordan* [1982, 1983]. The rapid fall-off of moment with frequency indicates that the characteristic duration is large. The fit by an Aki-type spectrum (solid line) yields $\tau_c = 70 \pm 3$ s. *Bottom.* Time-shift spectrum $\Delta t(\omega)$ calculated by the method of M. A. Riedesel and T. H. Jordan (manuscript in preparation, 1990). The reference time is the NEIC origin time for this event. Our data are consistent with the centroid time shift $\Delta t_1 = 5.1$ s obtained by Harvard's CMT solution. There is no obvious frequency variation in its time-shift spectrum, indicating that the skewness parameter $\hat{\mu}_3$ is small. This event formally fails the Stieltjes test, and we hypothesize it has a quiet earthquake as a slow precursor.

3.4 Physical Mechanisms. The mechanics of slow deformation is not well understood, and the primary motivation for undertaking these seismological studies is to provide new types of data that may improve that understanding. Although seismological research on slow-earthquake phenomena has been vigorous for over ten years, the full variety of strain release mechanisms with characteristic velocities in the range from 10 m/s to 1 km/s has not yet been assessed (cf. Figure 1). A number of physical mechanisms have been postulated to explain the stabilization of slip at low rupture velocities, including strain-weakening effects [*Dieterich*, 1979; *Das and Scholz*, 1981], strain-hardening effects [*Rice and Cleary*, 1976; *Rice and Simons*, 1976; *Tse and Rice*, 1986; *Rudnicki and Chen*, 1988], viscoelastic mechanisms [*Yamashita*, 1980; *Bonafede et al.*, 1983], and ductile instabilities [*Hobbs et al.*, 1986]. Non-dislocation sources having low characteristic velocities, such as phase changes [*Benioff*, 1963; *Dziewonski and Gilbert*, 1974] and the large-scale slumping of soft sediments or landslides [*Kanamori*, 1988; *Kawakatsu*, 1989], may also be seismologically significant. Laboratory experiments have shown that stable aseismic slip precedes unstable stick-slip [*Scholz et al.*, 1972]. *Dieterich* [1978] has found that in addition to this slow aseismic slip, there is a second stage of more rapid slip occurring immediately prior to failure. Laboratory measurements of this deformation yield propagation velocities in the range 20-200 m/s, within the field of slow and silent earthquakes shown in Figure 1.

The data collected from our studies should provide new constraints on the physical models of slow deformation in the lithosphere and deeper regions of the earth's interior. Because we are able to collect a global sample of earthquake activity, we can look for correlations among the data that describe the slow components of deformation, as well as between these data and the geological variables that might control the deformation processes. The latter include both state variables (pressure, temperature, composition) and parameters describing the region's deformation history (e.g., its other large earthquakes).

References

Abe, K., Tsunami and mechanism of great earthquakes, Phys. Earth and Planet. Int., 7, 143-153, 1973.

Aki, K., Generation and propagation of G waves from the Niigata earthquake of June 16, 1964, 2, estimation of earthquake moment, released energy, and stress-strain drop from the G wave spectrum, Bull. Earthquake Res. Inst. Univ. Tokyo, 44, 23-88, 1966.

Backus, G., Interpreting the seismic glut moments of total degree two or less, *Geophys. J. R. Astron. Soc.*, **51**, 1-25, 1977a.

Backus, G., Seismic sources with observable glut moments of spatial degree two, *Geophys. J. R. Astron. Soc.*, **51**, 27-45, 1977b.

Backus, G., and M. Mulcahy, Moment tensors and other phenomenological descriptions of earthquake sources, I, continuous displacements, *Geophys. J. R. Astron. Soc.*, **46**, 341-361, 1976a.

Backus, G., and M. Mulcahy, Moment tensors and other phenomenological descriptions of earthquake sources, II, discontinuous displacements, *Geophys. J. R. Astron. Soc.*, **46**, 301-329, 1976b.

Benioff, H., Source waveforms of three earthquakes, *Bull. Seismol. Soc. Am.*, *53*, 893-903, 1963.

Benioff, H. and F. Press, Progress report on long period seismographs, *Geophys. J. R. Astron. Soc.*, *1*, 208-215, 1958.

Beroza, G. C., and T. H. Jordan, Searching for slow and silent earthquakes using free oscillations, *J. Geophys. Res.*, **95**, 2485-2510, 1990a.

Beroza, G. C., and T. H. Jordan, Evidence for anomalous seismic events from a decade of continuous normal-mode observations, *Eos*, **71**, 559 (abstract), 1990b.

Bonafede, M., E. Boschi, and M. Dragoni, Viscoelastic stress relaxation on deep fault sections as a possible source of very long period elastic waves, *J. Geophys. Res.*, **88**, 2251-2260, 1983.

Cifuentes, I. L., and P. G. Silver, Low-frequency characteristics of the great 1960 Chilean earthquake, *J. Geophys. Res.*, **94**, 1989.

Dahlen, F. A., The effect of data windows on the estimation of free oscillation parameters, *Geophys. J. R. Astron. Soc.*, **69**, 537-549, 1982.

Das, S. and C. H. Scholz, Theory of time-dependent rupture in the earth, *J. Geophys. Res.*, *86*, 6039-6051.

Dieterich, J. H., Presesismic fault slip and earthquake prediction, *J. Geophys. Res.*, *83*, 3940-3948, 1978.

Dieterich, J. H., Modeling of rock friction 1. experimental results and constitutive equations, *J. Geophys. Res.*, *84*, 2161-2168, 1979.

Dziewonski, A. M., and F. Gilbert, Temporal variation of the seismic moment tensor and evidence of precursive compression for two deep earthquakes, *Nature*, *247*, 185-188, 1974.

Dziewonski, A. M., T. A. Chou, and J. H. Woodhouse, Determination of earthquake source parameters from waveform data for studies of global and regional seismicity, *J. Geophys. Res.*, **86**, 2825-2852, 1980.

Gilbert, F. and A. M. Dziewonski, An application of normal mode theory to the retrieval of structural parameters and source mechanisms from seismic spectra, *Phil Trans. R. Soc. Lond., A, 278*, 187-269, 1975.

Hanks, T. C., and H. Kanamori, A moment magnitude scale, *J. Geophys. Res.*, **84**, 2348-2350, 1979.

Hobbs, B. E., A. Ord, and C. Teyssier, Earthquakes in the ductile regime?, *PAGEOPH*, *124*, 309-336, 1986.

Jordan T. H., A procedure for estimating lateral variations from low-frequency eigenspectra data, *Geophys. J. R. Astron. Soc.*, *52*, 441-455, 1978.

Jordan, T. H., A method for detecting slow precursors to fast seismic ruptures, *Eos*, **71**, 559, 1990.

Kanamori, H., Mechanism of tsunami earthquakes, *Phys. Earth and Planet. Int.*, **6**, 346-359, 1972.

Kanamori, H., and J. W. Given, Use of long period surface waves for rapid determination of earthquake source parameters, *Phys. Earth and Planet. Int.*, **27**, 8-31, 1981.

Kanamori, H., and J. Cipar, Focal processes of the great Chilean earthquake May 22, 1960, *Phys. Earth. Planet. Int.*, **9**, 128-136, 1974.

Kanamori, H. and G. S. Stewart, A slow earthquake, *Phys. Earth and Planet. Int.*, **18**, 167-175, 1979.

Kasahara, K., Earthquake fault studies in Japan, *Phil. Trans. Roy. Soc. London, Ser. A*, **274**, 287, 1973.

Kawakatsu, H., Centroid single-force inversion of seismic waves generated by landslides, *J. Geophys. Res.*, *94*, 12363-12374, 1989.
King, C-Y., R. D. Nason, and D. Tocher, Kinematics of fault creep, *Phil. Trans. Roy. Soc. London, Ser. A*, **274**, 355-360, 1973.
Linde, A. T., K. Suyehiro, S. Miura, I. S. Sacks, and A. Takagi, Episodic aseismic earthquake precursors, *Nature, 334*, 513-515, 1988.
Okal, E. A., and L. M. Stewart, Slow earthquakes along oceanic fracture zones: evidence for asthenospheric flow away from hotspots?, *Earth and Plant. Sci. Lett.*, **57**, 75-87, 1982.
Pelayo, A. M., and D. A. Wiens, The November 20, 1960 Peru Tsunami earthquake: source mechanism of a slow event, *Geophys. Res. Lett.*, **17**, 661-664, 1990.
Rice, J. R., and M. P. Cleary, Some basic stress-diffusion solutions for fluid-saturated elastic porous media with compressible constituents, *Rev. Geophys. Space Phy., 14(2)*, 227-241, 1976.
Rice, J. R., and D. A. Simons, The stabilization of spreading shear faults by coupled deformation-diffusion effects in fluid-infiltrated porous materials, *J. Geophys. Res., 81*, 5322-5334, 1976.
Rice, J. R., The mechanics of earthquake rupture, in: *Proc. Int. School Phys. Enrico Fermi, Course LXXVIII, Phys. Earths Int.*, North Holland, 555-649, 1980.
Rice, J. R., and D. A. Simons, The stabilization of spreading shear faults by coupled deformation-diffusion effects in fluid-infiltrated porous materials, *J. Geophys. Res.*, **81**, 5322-5334, 1976.
Riedesel, M. A., and T. H. Jordan, Display and assessment of seismic moment tensors, *Bull. Seismol. Soc. Am., 79*, 85-100, 1989.
Riedesel, M. A., T. H. Jordan, A. F. Sheehan, and P. G. Silver, Moment-tensor spectra of the 19 Sept 85 and 21 Sept 85 Michoacan, Mexico, earthquakes, *Geophys. Res. Lett.*, **13**, 609-612, 1986.
Rudnicki, J. W., and C. H. Chen, Stabilization of frictional slip on a weakening fault by dilatant hardening, *J. Geophys. Res., 93*, 4745-4757, 1988.
Rundle, J. B., Viscoelastic crustal deformation by finite quasi-static sources, *J. Geophys. Res.*, **83**, 5937-5945, 1978.
Sacks, I. S., S. Suyehiro, A. T. Linde, and J. A. Snoke, Slow earthquakes and stress redistribution, *Nature*, **275**, 599-602, 1978.
Sacks, I. S., A. T. Linde, J. A. Snoke, and S. Suyehiro, A slow earthquake sequence following the Izu-Oshima earthquake of 1978, in: *Earthquake Prediction an International Review*, AGU ,617-628, 1981.
Scholz, C. H., *The Mechanics of Earthquakes and Faulting*, Cambridge, 439 pp., 1990.
Scholz, C. H., M. Wyss, and S. W. Smith, Seismic and aseismic slip on the San Andreas fault, *J. Geophys. Res.*, **74**, 2049-2069, 1969.
Scholz, C. H., P. Molnar, and T. Johnson, Detailed studies of frictional sliding of granite and implications for earthquake mechanism, *J. Geophys. Res., 77*, 6392-6406, 1972.
Silver, P. G., A. Linde, and D. T. Sandwell, Apparent strain migration and the coupling of earthquake activity, *EOS Trans. AGU*, **67**, 1087, 1986.
Silver, P. G., and T. H. Jordan, Optimal estimation of scalar seismic moment, *Geophys. J. R. Astron. Soc.*, **70** 755-787, 1982.
Silver, P. G., and T. H. Jordan, Total-moment spectra of fourteen large earthquakes, *J. Geophys. Res.*, **88**, 3273-3293, 1983.
Stewart, L. M., and E. A. Okal, Seismicity and aseismic slip along the Eltanin fracture zone, *J. Geophys. Res., 88*, 10495-10507, 1983.
Tse, S. T. and J. R. Rice, Earthquake instability in relation to the depth variation of frictional slip properties, *J. Geophys. Res., 91*, 9452-9472, 1986.
Yamashita, T., Quasistatic crack extension in an inhomogeneous viscoelastic medium - a possible mechanism for the occurrence of aseismic faulting, *J. Phys. Earth., 28*, 309-326, 1980b.

Appendicies

A. "Total-moment spectra of fourteen large earthquakes"
by P.G. Silver and T.H. Jordan

B. "Moment-tensor spectra of the 19 Sept 85 and
21 Sept 85 Michoacan, Mexico, earthquakes"
by M.A. Riedesel, T.H. Jordan, A.F. Sheehan, and P.G. Silver

C. "Searching for slow and silent earthquakes using free oscillations"
by G.C. Beroza and T.H. Jordan

JOURNAL OF GEOPHYSICAL RESEARCH, VOL. 88, NO. B4, PAGES 3273–3293, APRIL 10, 1983

Total-Moment Spectra of Fourteen Large Earthquakes

PAUL G. SILVER[1] AND THOMAS H. JORDAN

Geological Research Division, Scripps Institution of Oceanography, La Jolla, 92093 California

Total-moment spectra $M_T(\omega) = ||\mathbf{M}(\omega)||/\sqrt{2}$, where $\mathbf{M}$ is the moment rate tensor, are computed for 14 large earthquakes recorded by the International Deployment of Accelerometers (IDA) network using the scalar-moment retrieval method proposed by *Silver and Jordan* [1982]. For each event we obtain estimates of M_T averaged over the 10 disjunct, 1-mHz intervals in the low-frequency band 1–11 mHz; typical IDA record sets from events with $M_T \geq 0.2$ A (1 A = 10^{27} dyne · cm) yield standard errors on the 1-mHz averages that are generally less than 20%. Our multiple-band estimates of M_T are usually consistent with comparable single-band values found by other investigators. From the total-moment spectra we derive the zero-frequency (static) moment $M_T^0 \equiv M_T(0)$ and the characteristic source duration $\tau_c \equiv 2\,(\mathrm{Var}\,[f(t)])^{1/2}$, where $f(t)$ is the time function of the moment rate tensor, assumed to be the same for all components. The parameter τ_c formally depends on the second-degree temporal, spatial, and mixed spatial-temporal moments of an extended source, but calculations with realistic source geometries indicate that the interpretation of τ_c strictly in terms of the second temporal moment leads to very little error. A plot of τ_c against M_T^0 shows considerable scatter; some events lie significantly above the empirical scaling curve of *Kanamori and Given* [1981] ('slow earthquakes') and some below ('fast earthquakes'). Examples of the former include all three deep-focus events analyzed here as well as the 1970 Colombia and 1963 Peru-Bolivia deep-focus earthquakes, whose total-moment spectra are calculated from the moment tensor solutions of *Gilbert and Dziewonski* [1975]. An example of the latter is the great Sumbawa earthquake of August 9, 1977 ($M_T^0 = 24 \pm 3$ A), which is inferred to have a relatively shallow spatial centroid (< 20 km) and a nearly flat moment spectrum, suggesting that the faulting was confined to the upper, more brittle portion of the oceanic lithosphere. Three other large earthquakes — Tonga (June 22, 1977; $M_T^0 = 23 \pm 2$ A), Kuril Islands (December 6, 1978; $M_T^0 = 3.6 \pm 0.2$ A), and Tumaco (December 12, 1979; $M_T^0 = 25 \pm 2$ A) — exhibit moment spectra which significantly decrease toward higher frequencies, indicating larger values of τ_c. The aftershocks of both the Tonga and Kuril Islands events are distributed over a considerable range of depths, consistent with rupture into the lower, more ductile portions of the oceanic lithosphere. We speculate that the characteristic source duration may be causally related to the depth of coseismic rupturing within the lithosphere.

INTRODUCTION

In a recent paper [*Silver and Jordan*, 1982; hereinafter called SJ] we have defined two scalar measures of seismic moment based on the first and second invariants of the moment rate tensor $\mathbf{M}(\omega)$:

Total moment

$$M_T(\omega) = \frac{1}{\sqrt{2}}\,||\mathbf{M}(\omega)|| = [\frac{1}{2}\,\mathbf{M}^*(\omega) : \mathbf{M}(\omega)]^{1/2} \qquad (1)$$

Isotropic moment

$$M_I(\omega) = \frac{1}{\sqrt{6}}\,|\,tr\mathbf{M}(\omega)\,| \qquad (2)$$

(the colon represents the tensor double dot product and the asterisk denotes complex conjugation). In principle, these scalar moment spectra can be calculated from estimates of tensor moment, but successful attempts to retrieve the entire moment rate tensor $\mathbf{M}(\omega)$ over a broad frequency band have been rare. An exception is the study of *Gilbert and Dziewonski* [1975], who used over 100 hand-digitized records from the World-Wide Standardized Seismographic Network (WWSSN) to determine $\mathbf{M}(\omega)$ from 2 to 14 millihertz (mHz) for two deep-focus South American events. They found a slow, precursive (by about 80 s), isotropic component to the 1970 Colombia earthquake and a similar, though statistically less significant, result for the 1963 Peru-Bolivia event. The total-moment spectra $M_T(\omega)$ derived from their estimates of $\mathbf{M}(\omega)$ are displayed in Figure 1. A strong frequency dependence is observed in both cases, corresponding to a drop in total moment of more than 70% across the band.

Subsequent work on the problem of moment-tensor retrieval at low frequencies has been largely based on data recorded by recently installed global digital arrays, such as the International Deployment of Accelerometers (IDA) network. Efforts to retrieve $\mathbf{M}(\omega)$ from these sparse (<20 stations) networks over a frequency band comparable to the *Gilbert and Dziewonski* [1975] study have been severely hampered by the effects of lateral heterogeneity. Determinations of the moment rate tensor have typically been limited to single-band estimates in the interval 2–6 mHz [*Kanamori and Given*, 1981; G. Masters and F. Gilbert, unpublished material, 1982].

In SJ we have discussed a method for estimating the scalar moment spectra of (1) and (2) without first having to determine the entire moment rate tensor. From an

[1]Now at Carnegie Institute of Washington, Department of Terrestrial Magnetism, Washington, D.C. 20015

Paper number 2B1959.
0148-0227/83/002B-1959$05.00.

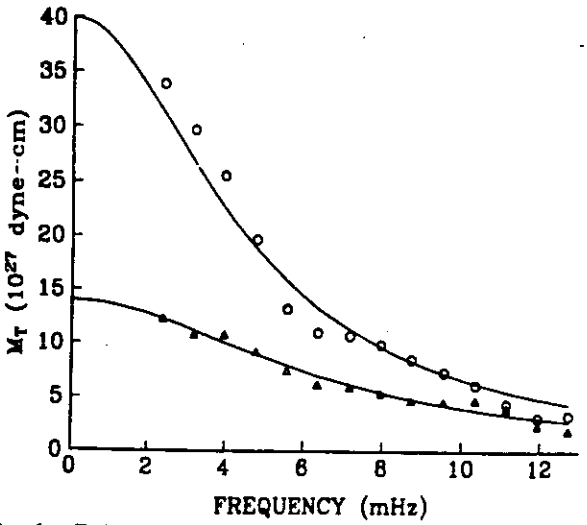

Fig. 1. Estimates of total moment obtained by *Gilbert and Dziewonski* [1975] for the Colombia event of July 31, 1970 (circles), and for the Peru-Bolivia event of August 15, 1963 (triangles). Curves are theoretical spectra (equation (22)) corresponding to $M_T^f = 40$ A and $\tau_c = 100$ s for the former and to $M_T^f = 14$ A and $\tau_c = 70$ s for the latter.

examination of two events, the shallow-focus Oaxaca earthquake of November 29, 1978, and the deep-focus Honshu earthquake of March 7, 1978, we showed that as many as 10 estimates of total moment could be obtained from IDA data in the 1–11 mHz band with standard errors generally less than 20%. Thus anomalous frequency dependence of the sort shown in Figure 1 or associated with other 'slow' earthquakes [*Kanamori and Cipar*, 1974; *Kanamori and Stewart*, 1976; *Sacks et al.*, 1978, 1981] should be detectable with this method.

The present study constitutes an extension of our work on total moment. Total-moment spectra over the band 1–11 mHz are estimated for 14 large earthquakes recorded by the IDA network during the period 1977–1979. From each of these spectra we derive estimates of two important spectral parameters, the static moment and the characteristic time of the source.

The zero-frequency, or static, moment $M_T^f \equiv M_T(0)$ is a scalar measure of the final state of the stress glut $\Gamma(\mathbf{r},t)$ [*Backus and Mulcahy*, 1976*a*, *b*] integrated over the source volume:

$$M_T^f = \frac{1}{\sqrt{2}} \| \int_V \Gamma(\mathbf{r},\infty)\, d\mathbf{r} \| \tag{3}$$

M_T^f is an appropriate measure of the size of an event not necessarily adequately described by a dislocation (double couple) source model. In the case of a double couple with a step function time history, M_T^f reduces to the ordinary seismic moment. All estimates of $M_T(\omega)$ and M_T^f quoted in this paper are given in units of 10^{27} dyne cm $= 10^{20}$ N m, which we abbreviate by A, after the first investigator to measure this quantity [*Aki*, 1966].

The variation of $M_T(\omega)$ with frequency can be related to the time history of the source, placing constraints on the source duration and other parameters of the source time function. Throughout our analysis we shall assume the moment-rate tensor has the form

$$\mathbf{M}(t) = \mathbf{M}\, f(t) \tag{4}$$

where $\mathbf{M}$ is constant tensor with $\| \mathbf{M} \| = \sqrt{2}\, M_T^f$; this is a special case of a synchronous source, one for which every element of $\mathbf{M}(t)$ has the same temporal centroid (SJ). It is then straightforward to show that at low frequency $M_T(\omega)$ can be expressed in terms of the first few even central moments $\hat{\mu}^{(2n)}$ $(n = 1,2,\cdots)$ of $f(t)$:

$$M_T(\omega) = M_T^f[1 - \omega^2\hat{\mu}^{(2)}/2 + \omega^4\hat{\mu}^{(4)}/24 - O(\omega^6)] \tag{5}$$

From the variance $\hat{\mu}^{(2)}$ we can define the characteristic source time

$$\tau_c = 2(\hat{\mu}^{(2)})^{1/2} \tag{6}$$

to be a measure of source duration. Unlike the measures of source duration used by some authors, this definition is general and can be applied to any source time function. For example, a *Haskell* [1964] source, employed by *Furumoto* [1979], has a time function characterized by a rise time τ_R and rupture time τ_L, which yields a characteristic time

$$\tau_c = [(\tau_R^2 + \tau_L^2)/3]^{1/2} \tag{7}$$

Kanamori and Given [1981] assume a 'boxcar' source time function ($\tau_R = 0$) and define the 'source process time' to be τ_L, the length of the boxcar; to compare their estimates of source duration with those derived in this paper one must divide the former by 1.73.

While it is convenient to interpret the frequency dependence of total moment strictly in terms of the temporal extent of the source, it has been pointed out by *Backus* [1977*a*, *b*] that a consistent interpretation requires the inclusion of higher spatial moments of the glut rate tensor $\dot{\Gamma}(\mathbf{r},t) \equiv \partial_t \Gamma(\mathbf{r},t)$, in particular,

$$\mathbf{M}^{(2)}(\omega) = \int_V \dot{\Gamma}(\mathbf{r},\omega)\, (\mathbf{r} - \mathbf{r}_o)(\mathbf{r} - \mathbf{r}_o)\, d\mathbf{r}$$

which depends on the spatial extent of the source. We show in the appendix that for a reasonable class of source models little error is incurred by ignoring these higher spatial moments in the interpretation of τ_c.

If the point $\mathbf{r}_o$ differs from the source centroid, the first spatial moment

$$\mathbf{M}^{(1)}(\omega) = \int_V \dot{\Gamma}(\mathbf{r},\omega)(\mathbf{r} - \mathbf{r}_o)\, d\mathbf{r}$$

also contributes to the estimate of total seismic moment, thus introducing a frequency-dependent bias. Errors in

hypocentroidal depth are the main source of location bias. This problem is discussed in the context of individual events.

METHODOLOGY

The moment-tensor representation of a double-couple point source with step function time dependence $H(t)$ can be written as the product of a scalar seismic moment M_0 and a source mechanism specified by unit vectors $\hat{\mathbf{s}}$ and $\hat{\mathbf{f}}$ defining the slip direction and normal to the fault plane (double couple):

$$\mathbf{M}(\omega) = M_0[\hat{\mathbf{f}}\hat{\mathbf{s}} + \hat{\mathbf{s}}\hat{\mathbf{f}}] \tag{8}$$

A general moment rate tensor can be expressed in a similar fashion using $M_T(\omega)$, the frequency-dependent extension of M_0 defined in (1):

$$\mathbf{M}(\omega) = \sqrt{2}\, M_T(\omega)\hat{\mathbf{M}}(\omega) \tag{9}$$

We refer to the unit tensor $\hat{\mathbf{M}}$ satisfying $\hat{\mathbf{M}}^* : \hat{\mathbf{M}} = 1$ as the source mechanism, generalizing the terminology usually reserved for the bracketed expression in (8).

To facilitate the following discussion, we introduce an isomorphism between three-dimensional, second-order, symmetric tensors $\mathbf{M}$ and vectors of dimension six

$$m_1 = M_{11} \quad m_2 = M_{22} \quad m_3 = M_{33}$$

$$m_4 = \sqrt{2}\, M_{12} \quad m_5 = \sqrt{2}\, M_{13} \quad m_6 = \sqrt{2}\, M_{23} \tag{10}$$

This particular isomorphism, written $\mathbf{M} <=> \mathbf{m}$, has the advantage of preserving the Euclidian norm (SJ). Thus the familiar representation of the seismogram $u_p(\omega)$ in terms of the moment rate tensor $\mathbf{M}(\omega)$ and tensor-valued transfer function $\mathbf{G}_p(\omega)$, usually written

$$u_p(\omega) = \mathbf{G}_p(\omega) : \mathbf{M}(\omega) \tag{11}$$

can be expressed by this isomorphism as the vector dot product

$$u_p(\omega) = \mathbf{g}_p(\omega) \cdot \mathbf{m}(\omega) \tag{12}$$

where p refers to the p th seismic station and $\mathbf{G}_p <=> \mathbf{g}_p$. Similarly, the definition of $M_T(\omega)$ can be written

$$M_T^2 = \tfrac{1}{2}\, \mathbf{m}^* \cdot \mathbf{m} = \mathbf{m}^* \cdot \mathbf{C} \cdot \mathbf{m} \tag{13}$$

i.e., as a vector norm defined by the 6×6 matrix $\mathbf{C} = (1/2)\mathbf{I}$.

The basic datum employed by this method is the frequency-averaged cross spectrum between Fourier-transformed seismograms at the p th and q th stations,

$$U_{pq} = \int_{\omega_a}^{\omega_b} u_p^*(\omega)\, u_q(\omega)\, d\omega \tag{14}$$

We assume that $\mathbf{m}(\omega)$ is slowly varying in the interval $[\omega_a, \omega_b]$, in which case, (14) can be rewritten

$$U_{pq} = \mathbf{m}^* \cdot \mathbf{H}_{pq} \cdot \mathbf{m} \tag{15}$$

in terms of the outer product matrix

$$\mathbf{H}_{pq} = \int_{\omega_a}^{\omega_b} \mathbf{g}_p^*(\omega)\, \mathbf{g}_q(\omega)\, d\omega \tag{16}$$

Consider a linear combination of U_{pq}'s denoted by

$$\tilde{M}_T^2 = \sum_{p,q} a_{pq} U_{pq} \tag{17}$$

Equation (15) allows us to write this sum as

$$\tilde{M}_T^2 = \mathbf{m}^* \cdot \Big[\sum_{p,q} a_{pq}\, \mathbf{H}_{pq}\Big] \cdot \mathbf{m} \tag{18}$$

Noting the similarity between the defining expression (13) for M_T^2 and (18), we see that if coefficients $\{a_{pq}\}$ can be found which solve

$$\sum_{p,q} a_{pq}\, \mathbf{H}_{pq} = \mathbf{C} \tag{19}$$

then $\tilde{M}_T^2 = M_T^2$; that is, the sum (17) will be exactly equal to squared total moment. Hence, the solution of (19) represents a linear method for retrieving M_T^2 without first having to determine the entire moment tensor.

In the case of error-free data, solving (19) exactly clearly yields the optimal estimate of squared total moment. Barring accidental degeneracies, this can be done with as few as six stations (SJ), so that the method is feasible for sparse digital networks such as IDA. In practice, the data are not exact but contaminated by various sources of observational error, including ambient seismic noise and 'signal-generated' noise caused by lateral heterogeneity. For any specified set of coefficients $\{a_{pq}\}$ these observational errors introduce an error e_a into the estimate of squared total moment. Theoretical expressions for e_a in terms of parameters describing ambient seismic noise and the effects of lateral heterogeneity are given by SJ. The analysis of lateral heterogeneity, typically the largest source of observational error, is done in the context of normal mode perturbation theory; the effects of aspherical structure are characterized by empirically derived rms deviations in the apparent amplitudes, center frequencies, and half widths of the resonance functions.

To optimize the estimate of squared total moment in

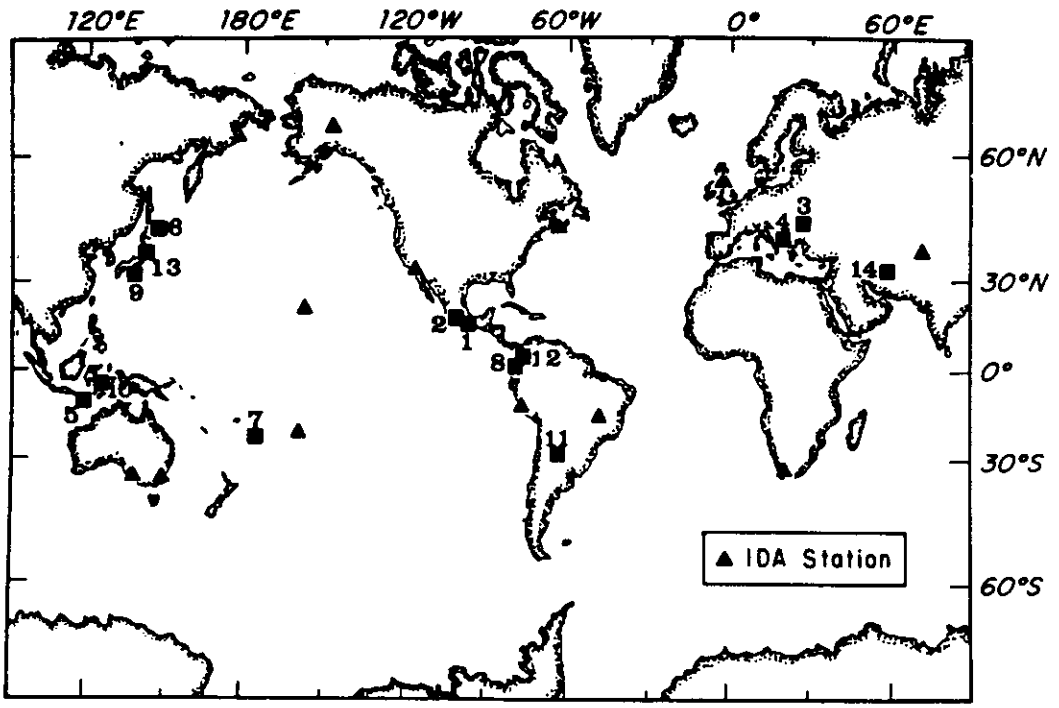

Fig. 2. Location of IDA stations (triangles) and earthquakes (squares) used in study. Event numbers correspond to those in Table 1.

the presence of observational errors, we must consider the error incurred by forming a matrix

$$\tilde{\mathbf{C}} = \sum_{p,q} a_{pq} \mathbf{H}_{pq}$$

which only approximates C. This latter error, referred to as modeling error, is defined by

$$\hat{e}_m = \hat{\mathbf{m}}^* \cdot (\tilde{\mathbf{C}} - \mathbf{C}) \cdot \hat{\mathbf{m}} \tag{20}$$

The statistics of $\hat{e}_m$ are determined from our knowledge of the source mechanism $\hat{\mathbf{m}}$. If $\hat{\mathbf{m}}$ were known exactly, $\hat{e}_m$ could be calculated and used to correct the estimate $\hat{M}_T^2$. In any practical situation the source mechanism is unknown, or only an estimate $\hat{\mathbf{m}}_o$ is available. In either case, we can treat $\hat{\mathbf{m}}$ as a stochastic variable and use this information (or lack of it) to form a probability distribution for the orientation of $\hat{\mathbf{m}}$. For each of the events studied below, we have obtained a most probable mechanism $\hat{\mathbf{m}}_o$ from a fault plane solution or moment tensor inversion, along with estimates of the uncertainties from which we have constructed a covariance matrix $\hat{\mathbf{V}}_m$; under the Gaussian approximations discussed by SJ, these are sufficient to determine the statistics of $\hat{e}_m$.

The a_{pq}'s defining the squared-moment estimate are found by minimizing a linear combination of the mean squared observational error $\langle e_o^2 \rangle$ and the mean squared modeling error

$$\langle \hat{e}_m^2 \rangle = (\tilde{\mathbf{C}} - \mathbf{C})^* : \langle \hat{\mathbf{m}}\,\hat{\mathbf{m}}^*\,\hat{\mathbf{m}}^*\hat{\mathbf{m}} \rangle : (\tilde{\mathbf{C}} - \mathbf{C}) \tag{21}$$

The minimization leads to a system of normal equations given by SJ (equations 5.5-5.7), which are then solved by generalized inverse methods. The solution yields an unbiased, optimal estimate of M_T and its formal uncertainty.

Our procedure for estimating squared total moment can be thought of as an application of the *Backus and Gilbert* [1970] method of inference to a discrete problem: we seek a linear combination of the data which is an estimate of a particular model average. In this problem, the 'model' is the outer-product matrix $\mathbf{mm}^*$, and the desired property is one half its trace, the squared Euclidean norm of $\mathbf{m}$. The matrix $\tilde{\mathbf{C}}$ is analogous to the 'averaging kernel' of the Backus-Gilbert theory, whose construction is based on a trade-off curve analysis, as discussed by SJ.

TOTAL-MOMENT SPECTRA OF 14 EVENTS

The moment estimation procedure described above and elaborated on by SJ has been applied to 14 large earthquakes occurring in the years 1977–1979. These events span the moment range 0.19–25 A and the depth range 7–614 km. Figure 2 shows their epicenters; their location parameters are listed in Table 1. The earthquakes were recorded on vertical-component accelerometers of the IDA network. Of the 12 stations shown in Figure 2, the records from between 5 and 10 were available for any one event, and 8 or more of the stations could be utilized for most (11 out of 14) of the events. The cross spectra U_{pq} for each record pair were obtained by fast-Fourier transforming Hanning-windowed seismograms of 10-hour length beginning at the origin time of the event or, in cases where the instruments were initially saturated (e.g., the Sumbawa event), after the first good data point; the two spectra were then integrated over the 10 disjunct 1-mHz bands in the frequency interval 1–11 mHz. Time domain transfer functions were generated using the location parameters in Table 1, the 1066A model of *Gilbert*

TABLE 1. Earthquakes Studied

Event	Location	Date	Origin Time, UT	Latitude, deg	Longitude, deg	Depth, km	m_b	M_s
1	Oaxaca, Mexico	Nov. 29, 1978	1952:47.6	16.01 N	96.59 W	18	6.4	7.7
2	Petalan, Mexico	March 14, 1979	1107:16.3	17.81 N	101.28 W	20	6.5	7.6
3	Romania	March 4, 1977	1921:54.1	45.77 N	26.76 E	94	6.4	--
4	Montenegro, Yugoslavia	April 15, 1979	0619:44.1	42.10 N	19.21 E	17	6.2	6.9
5	Sumbawa, Indonesia	Aug. 19, 1977	0608:55.2	11.09 S	118.46 E	15	7.0	7.9
6	Kuril Islands	Dec. 6, 1978	1402:01.0	44.59 N	146.58 E	150	6.7	--
7	Tonga	June 22, 1977	1208:33.4	22.88 S	175.90 W	65	6.8	--
8	Tumaco, Colombia	Dec. 12, 1979	0759:03.3	1.60 N	79.36 W	29	6.4	7.7
9	Honshu, Japan	March 7, 1978	0248:47.6	32.00 N	137.61 E	439	6.9	--
10	Banda Sea	Feb. 21, 1978	0714:54.4	4.84 S	125.41 E	510	6.3	--
11	Argentina	Oct. 22, 1977	1757:17.4	27.95 S	62.97 W	614	6.1	--
12	Colombia	Nov. 23, 1979	2340:29.8	4.81 N	76.22 W	108	6.4	--
13	Miyagi-Oki, Japan	June 12, 1978	0814:26.4	38.19 N	142.03 E	44	6.8	7.7
14	Tabas, Iran	Sept. 16, 1978	1535:56.6	33.39 N	57.43 E	7	6.8	7.4

and Dziewonski [1975], and the radial Q model recently derived by *Masters and Gilbert* [1983]. These time series were processed exactly as the observed seismograms to yield the matrices $\mathbf{H}_{pq}$.

The total moment averaged over each of the ten 1-mHz bands between 1 and 11 mHz was computed for each event, corrected for bias, and assigned a standard error according to the procedures discussed by SJ. The event mechanism was assumed to be synchronous (in the sense of SJ, equation 2.13) and a sample from a hyperspherical normal distribution on the six-dimensional unit sphere. In all cases, the prior uncertainties of the mechanisms were small enough to permit the Gaussian approximation to the hyperspherical normal distribution. The most probable mechanisms $\hat{\mathbf{m}}_o$ adopted in the inversions are listed in Table 2 with references to the studies from which they were taken. The variance matrices $\hat{\mathbf{V}}_m$ were derived from the uncertainties in the moment tensor components quoted in the original studies or, in cases where only fault plane solutions were available, from a subjective assessment of the observational errors. A typical value of the marginal variance associated with an individual mechanism component was of the order of 0.03. As demonstrated by SJ, this is well within the range of the Gaussian approximation.

From the total-moment estimates for the 14 earthquakes we have estimated the static moments M_T^0 and characteristic times τ_c by fitting these estimates with moment spectra conforming to (5). The even central moments $\hat{\mu}^{(2n)}$ with $n \geqslant 2$ are often not well determined by the low-frequency data used in this study; we have therefore specified these in terms of $\hat{\mu}^{(2)}$ by adopting a moment spectrum of the form

$$M_T(\omega) = M_T^0 \, (1 + \omega^2 \tau_c^2/8)^{-1} \tag{22}$$

Equation (22) is consistent with the definition of the characteristic time given in (6) and implies that $\hat{\mu}^{(4)} = 6(\hat{\mu}^{(2)})^2$ in (5). Far-field source spectra of this type

TABLE 2. Source Mechanisms $\mathbf{m}$

Event	$\hat{m}_{rr}$	$\hat{m}_{\theta\theta}$	$\hat{m}_{\phi\phi}$	$\hat{m}_{r\theta}$	$\hat{m}_{r\phi}$	$\hat{m}_{\theta\phi}$	Reference*
1	0.262	-0.260	-0.002	0.717	-0.574	0.141	1
2	0.332	-0.274	-0.057	0.792	-0.391	0.177	2
3	0.637	-0.136	-0.503	-0.411	-0.392	0.006	3
4	0.354	-0.241	-0.112	0.746	-0.439	0.234	5
5	-0.680	0.680	0.000	0.000	-0.195	0.195	4
6	-0.468	0.207	0.261	0.425	-0.698	-0.055	3
7	-0.230	-0.004	0.234	0.383	0.863	0.018	3
8	0.260	0.043	-0.303	0.033	-0.908	-0.117	5
9	0.489	0.053	-0.541	0.384	-0.551	-0.121	3
10	-0.515	0.221	0.294	0.729	-0.208	0.156	3
11	0.127	-0.080	-0.047	-0.282	0.885	-0.335	3
12	-0.360	-0.289	0.648	-0.337	-0.485	0.146	6
13	0.460	-0.022	-0.437	0.118	0.745	-0.169	5
14	0.565	-0.194	-0.369	-0.506	0.220	0.450	7

*References: 1, *Stewart et al.* [1981]; 2, *Chael and Stewart* [1982]; 3, G. Masters and F. Gilbert (unpublished material, 1982); 4, G.S. Stewart (personal communication, 1982); 5, *Kanamori and Given* [1981]; 6, *Dziewonski et al.* [1981]; 7, *Niazi and Kanamori* [1981].

TABLE 3. Parameters Determined From Total-Moment Spectra

Event	M_0^f, A	Standard Error, A	τ_c, s	Standard Error, s	No. of Stations
1	2.7	0.3	3	15	9
2	1.9	0.2	13	15	10
3	1.4	0.1	4	15	5
4	0.37	0.06	7	15	10
5	24.	3.0	1	14	6
6	3.6	0.2	52	2	10
7	23.	2.0	66	2	7
8	25.	2.0	65	2	10
9	0.52	0.04	32	4	9
10	0.19	0.01	54	3	8
11	0.19	0.01	49	3	9
12	0.71	0.06	33	5	10
13	2.1	0.25	32	6	8
14	1.3	0.15	43	5	9

have been discussed by *Aki* [1967] and *Brune* [1970], among others.

The parameters M_0^f and τ_c and their standard errors, determined by regression fitting (22) to the observed moment spectra, are given in Table 3; in these calculations the total-moment estimates were assumed to be uncorrelated. Occasionally, the estimates of M_T averaged over the 1–2 mHz band had such low signal-to-noise ratios (SNR's) and such high standard errors (>30%) that doubt was cast on the validity of the estimation procedure, which assumes that the SNR is large. These points are displayed in the figures by a dashed error bar but were excluded from the determinations of M_0^f and τ_c.

Oaxaca

The Oaxaca earthquake of November 29, 1978, was a large thrust (M_s = 7.8) occurring along the Middle America Trench. It has been studied by a variety of investigators and thus serves as a good calibration event for the moment estimation procedure used in this study. Estimates of M_T obtained previously by SJ are presented in Figure 3. The moment spectrum is nearly flat, giving a static value of $M_0^f = 2.8 \pm 0.3$ A and a characteristic time of $\tau_c = 3 \pm 15$ s. In comparison, both *Stewart et al.* [1981] and M. Reichlie et al. (unpublished manuscript, 1982) find relatively short source times ($\tau_c < 15$ s), consistent with our results. The moment estimates of these two studies, obtained at approximately 5 mHz from surface wave data, are M_T = 3.2 A and M_T = 2.9 A, respectively, neither significantly different from our value for M_0^f.

Petalan

The Petalan earthquake of 1979 was located about 540 km northwest of the Oaxaca event and had nearly the same mechanism, depth, and source duration [*Chael and Stewart*, 1982; M. Reichlie et al., unpublished manuscript, 1982]. The moment spectrum shown in Figure 4 does not exhibit significant frequency dependence, which is reflected in the source duration estimate of $\tau_c = 13 \pm 15$

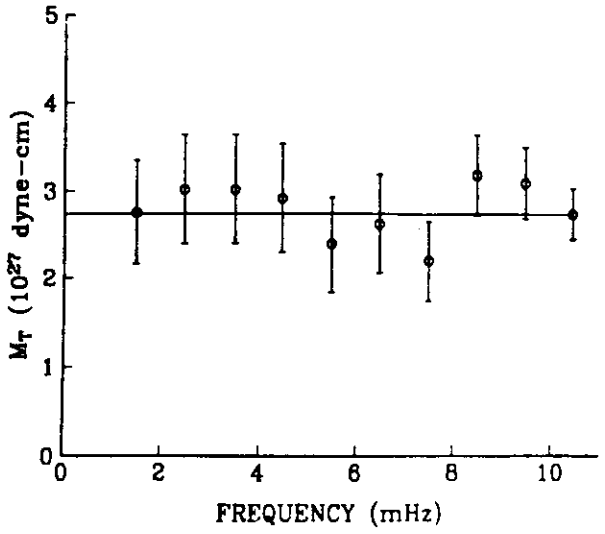

Fig. 3. Estimates of total moment averaged over 1-mHz bands for the Oaxaca, Mexico, event of November 29, 1978. Error bars represent one standard deviation. Curve corresponds to $M_0^f = 2.8$ A and $\tau_c = 3$ s.

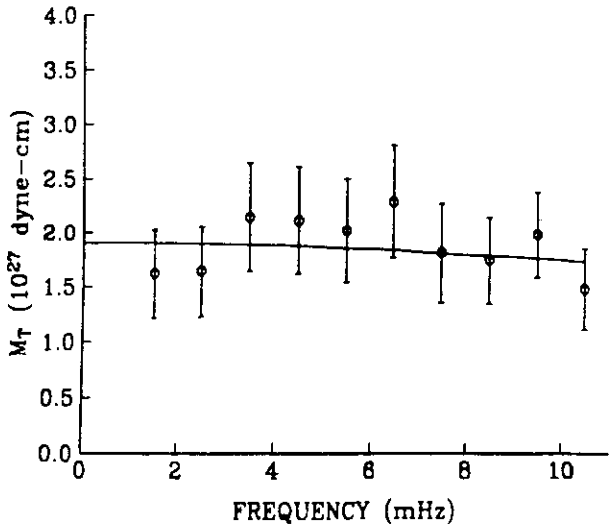

Fig. 4. Estimates of total moment averaged over 1-mHz bands for the Petalan, Mexico, event of March 14, 1979. Error bars represent one standard deviation. Curve corresponds to $M_0^f = 1.9$ A and $\tau_c = 13$ s.

s, and yields a static moment estimate of $M_0^f = 1.9 \pm 0.2$ A. While in agreement with the value of $M_T = 1.7$ A found by M. Reichlie et al. (unpublished manuscript, 1982), our estimate is somewhat below the total moment of $M_T = 2.7$ A given by *Chael and Stewart* [1982]. Both previous studies used surface waves at about 5 mHz.

Romania

The intermediate focus Romanian earthquake of March 4, 1977, was a complex thrust event found by *Müller et al.* [1978] to consist of three shocks occurring over a 15-s interval; the third and strongest event marked the abrupt termination of the sequence. These investigators obtained a high rupture velocity (near the shear wave speed) with a fault length of about 60 km. The 'fast' nature of this event is evident in the nearly constant moment spectrum shown in Figure 5; we find a characteristic source duration of $\tau_c = 4 \pm 15$ s. Our estimate of static moment $M_0^f = 1.4 \pm 0.1$ A falls within the range 1 A $\leqslant M_T \leqslant$ 2 A obtained by *Hartzell* [1979] from surface waves at approximately 18 mHz.

Montenegro

This 1979 earthquake occurred near the Montenegro region of Yugoslavia, just off the Adriatic coast. The moment tensor inversion of *Kanamori and Given* [1981] shows it to be a thrust event with both planes striking more or less parallel to the coastline. Although the National Earthquake Information Service (NEIS) placed the hypocenter at 10 km, we instead used the slightly greater depth of 17 km based on the study of *Console and Favali* [1981], who found most of the aftershocks occurring within the depth range 15–20 km. Our results for this event are shown in Figure 6. The nearly flat moment spectrum gives a short source duration of $\tau_c = 7 \pm 15$ s with a static moment of $M_0^f = 0.37 \pm 0.06$ A. The results of *Kanamori and Given* [1981] from Rayleigh waves at 4 mHz are in general agreement with these values; by correcting back to zero frequency using a source duration of $\tau_c = 6$ s, they find a slightly higher static moment of $M_0^f = 0.47$ A.

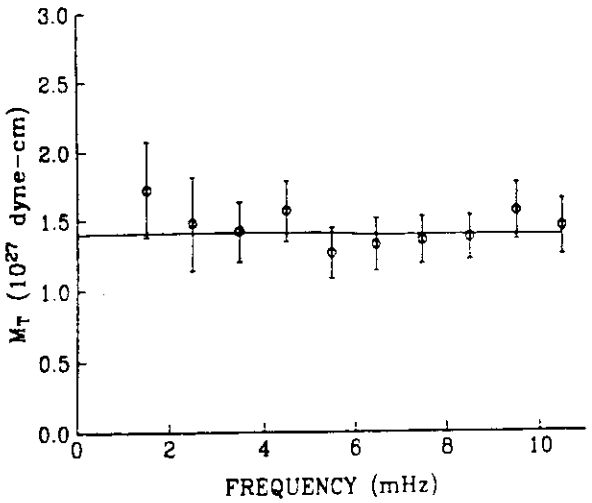

Fig. 5. Estimates of total moment averaged over 1-mHz bands for the Romania event of March 4, 1977. Error bars represent one standard deviation. Curve corresponds to $M_0^f = 1.4$ A and $\tau_c = 4$ s.

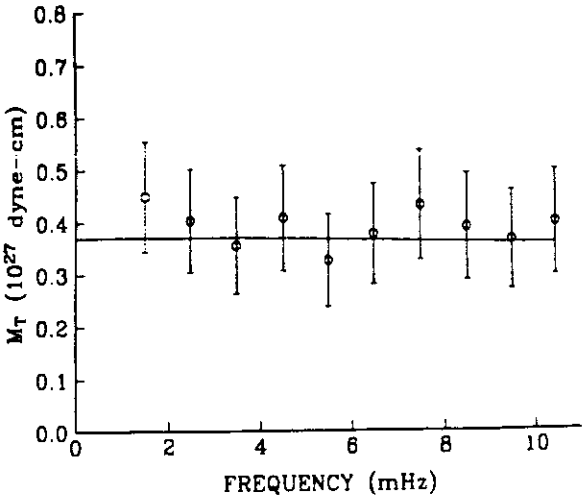

Fig. 6. Estimates of total moment averaged over 1-mHz bands for the Montenegro, Yugoslavia event of April 15, 1979. Error bars represent one standard deviation. Curve corresponds to $M_0^f = 0.37$ A and $\tau_c = 7$ s; first point of diagram was not used in its determination.

Sumbawa

The Sumbawa earthquake of August 19, 1977, was an unusually large normal-faulting event which occurred near the eastern end and seaward of the Java trench. There has been some question as to whether this event represented complete fracturing of the lithosphere, as proposed by *Given and Kanamori* [1980], or was associated with stresses due to plate bending and thus limited to the upper portion of the lithosphere [*Hanks*, 1979].

In performing the inversion for total moment we first placed the source centroid at 40 km, near the value of 43 km suggested by *Given and Kanamori* [1980]; these results are shown in Figure 7*c*. Instead of a flat spectrum or one which decreases monotonically with frequency, we find an unusual pattern characterized by a prominent peak between 4 and 6 mHz. A similar pattern is found in synthetic experiments for this event when the source depth is overestimated (Figure 8). Using $h = 25$ km yielded essentially the same pattern, although its amplitude was substantially diminished (Figure 7*b*), whereas moving the source depth to 15 km succeeded in removing the pattern (Figure 7*a*). These results suggest that the source centroid was probably shallower than 25 km. Of course, this does not preclude the possibility of some displacement occurring below, say, 50 km; it only suggests that the faulting was concentrated at shallow depths, a conclusion supported by the 8–24 km depth range of aftershocks found by *Fitch et al.* [1981] for this event. Our results are thus consistent with a plate-bending interpretation of the Sumbawa event.

The estimates of total moment found for our preferred depth of 15 km (Figure 7*a*) yield a value of $M_0^f = 24 \pm 3$ A, which, although somewhat lower that previously reported [*Given and Kanamori*, 1980], represents one of the largest static moments in this study. The surprising absence of any significant frequency dependence in the

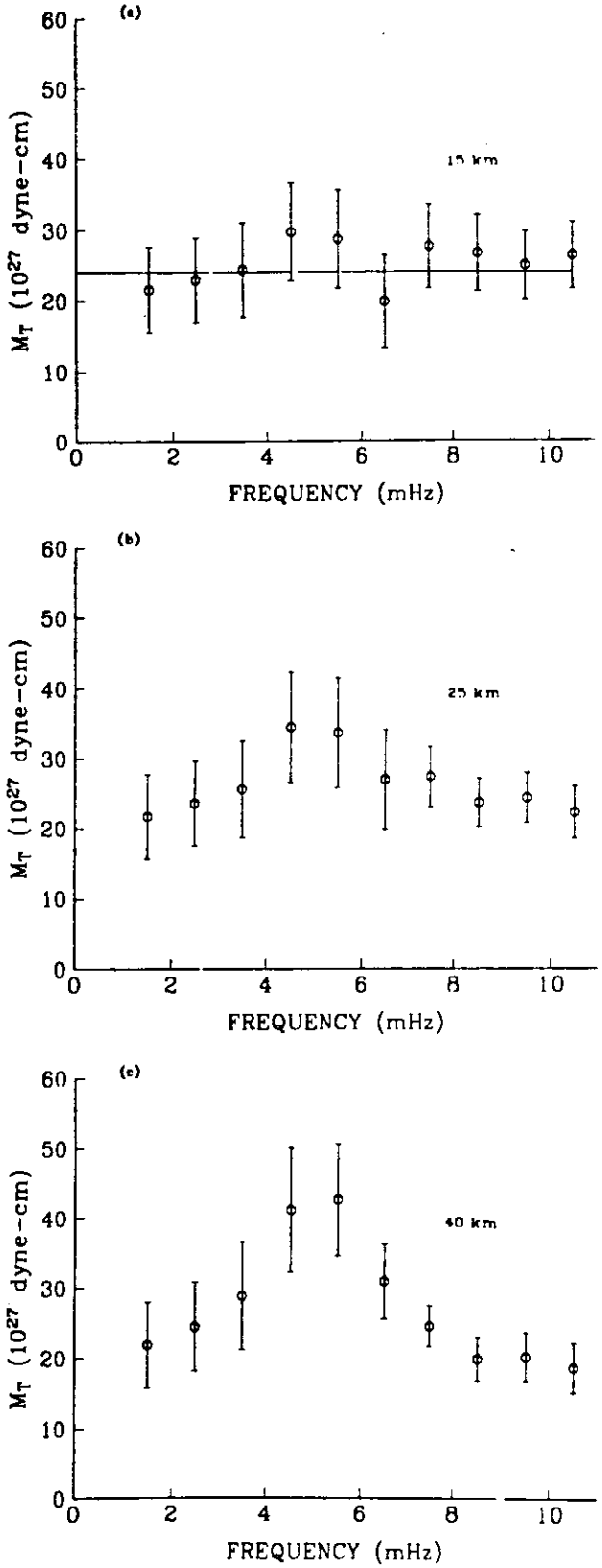

Fig. 7. Estimates of total moment averaged over 1-mHz bands for the Sumbawa, Indonesia, event of August 19, 1977, assuming focal depths of 15 km (*a*), 25 km (*b*), and 40 km (*c*). Error bars represent one standard deviation. Curve corresponds to $M\dot{\beta} = 24$ A and $\tau_c = 1$ s.

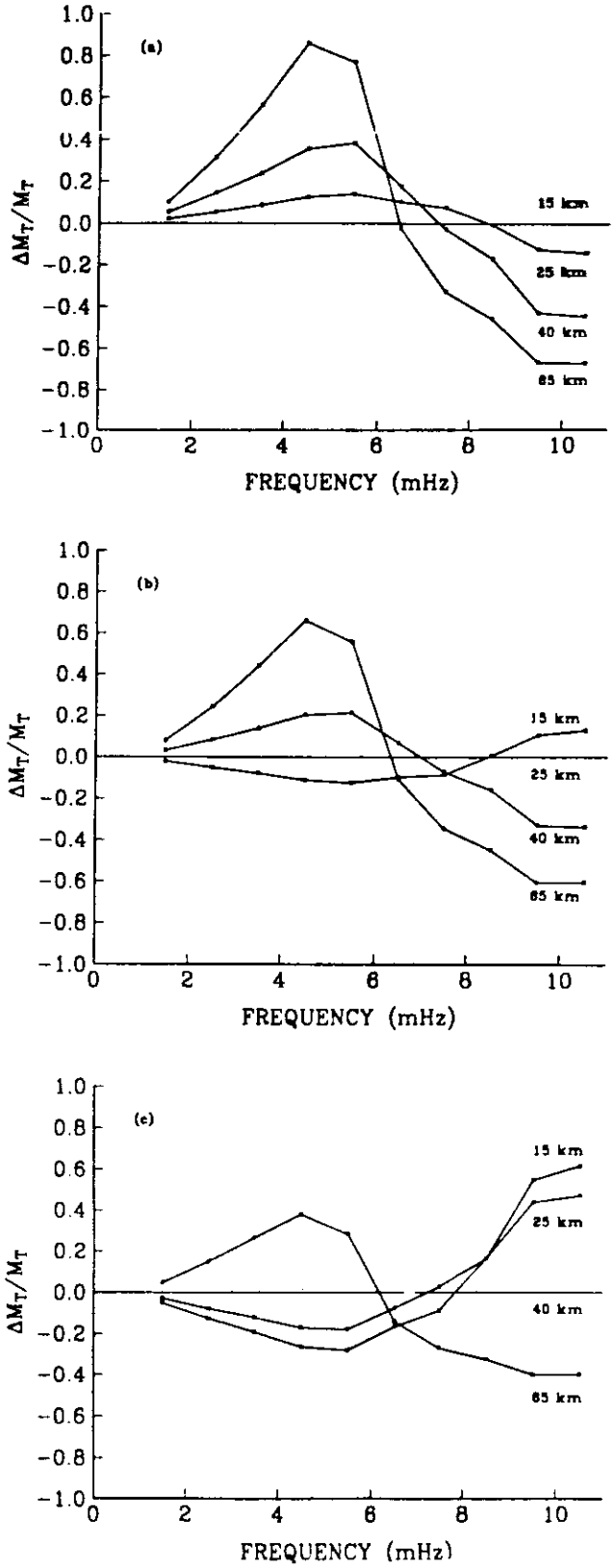

Fig. 8. Relative bias in total moment caused by displacement of the assumed source depth from its true value; curves computed from synthetic data generated at 15 km (*a*), 25 km (*b*), and 40 km (*c*) and inverted assuming focal depths of 15, 25, 40, and 65 km.

moment spectrum suggests that Sumbawa earthquake is unusually fast for its size: we obtain a characteristic source time of $\tau_c = 1 \pm 14$ s. From the fault length estimate of 100 km [*Fitch et al.*, 1981], this short duration is suggestive of a rupture velocity approaching the shear speed. One consequence of the relatively small source dimensions and large moment is a stress drop of several hundred bars, one of the largest ever computed for a major earthquake [*Hanks*, 1979; *Fitch et al.*, 1981].

Kuril Islands

The epicenter of the Kuril Islands earthquake of December 6, 1978, was north east of the island of Hokkaido, Japan (Figure 2); this general area is known as the Hokkaido corner and marks the juncture of the Kuril and North Honshu arcs. The event is one of the larger examined in this study and exhibits several interesting characteristics. Using the ISC depth of 118 km, we obtain the moment spectrum shown in Figure 9*a*. It is marked

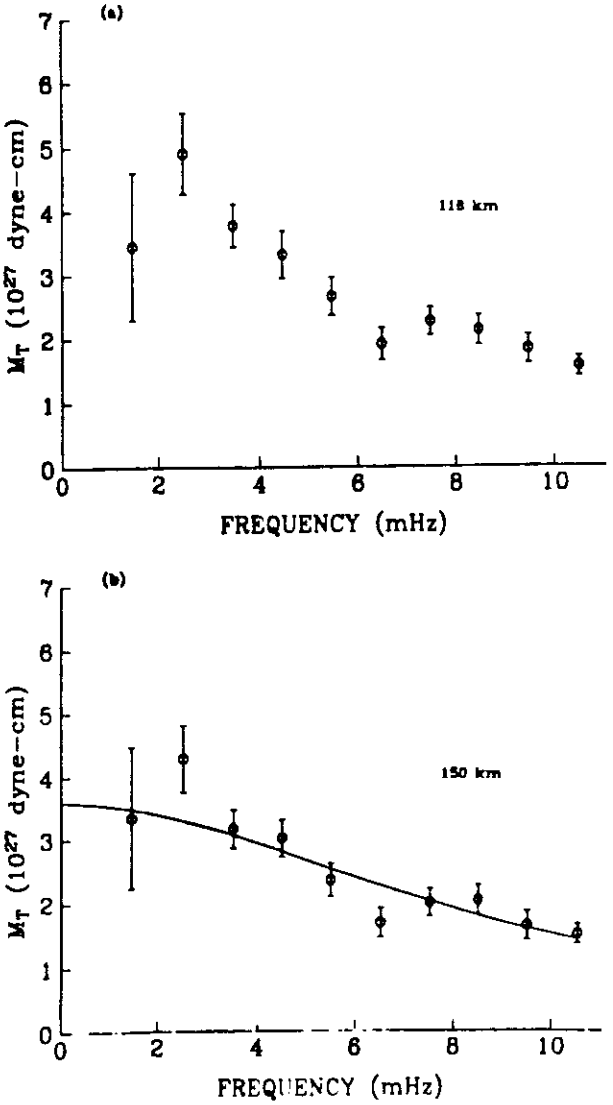

Fig. 9. Estimates of total moment averaged over 1-mHz bands for the Kuril Islands event of December 6, 1978, assuming focal depths of 118 km (*a*) and 150 km (*b*). Error bars represent one standard deviation. Curve in Figure 9*b* corresponds to $M_0^A = 4.3$ A and $\tau_c = 57$ s.

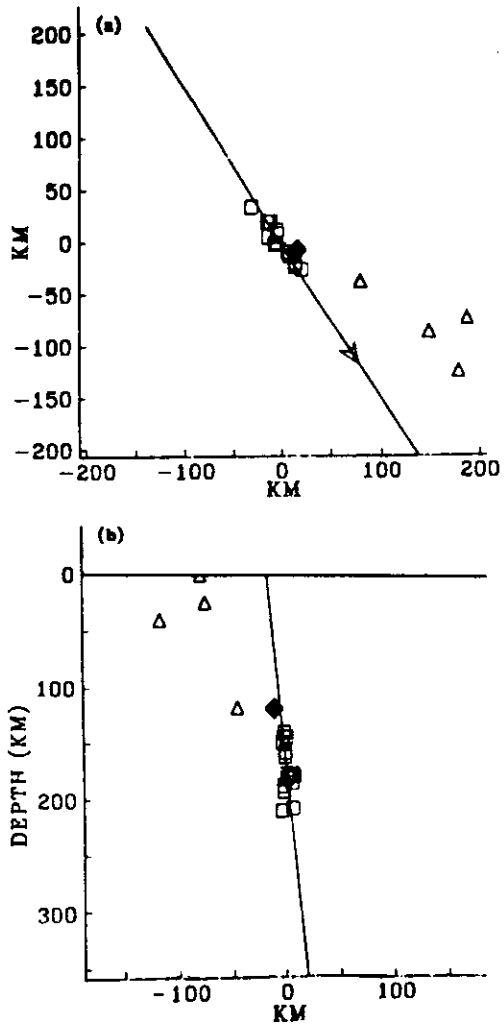

Fig. 10. (*a*) Map view of the 3-week aftershock distribution for the Kuril Islands earthquake; locations are from the ISC bulletins. Solid diamond denotes main event; squares and triangles represent events shallower and deeper than main event, respectively. Line is the strike of the best fitting plane to the main event and deeper aftershocks. (*b*) Vertical cross section of the aftershock distribution in the plane perpendicular to the best fitting plane, whose intersection is indicated by the solid line.

by a strong frequency dependence corresponding to a drop of nearly a factor of 3 across the band. These estimates give a static moment of $M_0^A = 4.3 \pm 0.3$ A and a large characteristic time of $\tau_c = 57 \pm 2$ s.

The ISC locations for the aftershocks occurring in the 3-week period following the main event are shown in Figure 10. It appears that there are two distinct aftershock populations, above (triangles) and below (squares) the depth of the main event, with the deeper aftershocks confined to a nearly planar region. In order to identify this plane we computed the sample covariance matrix V of the locations $\mathbf{r}_i$ of the deeper aftershocks and the main event, defined by

$$\mathbf{V} = \frac{1}{N-1} \sum_{i=1}^{N} (\mathbf{r}_i - \bar{\mathbf{r}})(\mathbf{r}_i - \bar{\mathbf{r}}) \qquad (23)$$

where $\bar{\mathbf{r}}$ is the aftershock centroid. The eigenvalues λ_i of V satisfying $\lambda_1 \geq \lambda_2 \geq \lambda_3$ are measures of the three

characteristic dimensions of the aftershock zone, whose corresponding principal directions are given by the eigenvectors $\hat{\mathbf{u}}_j$. For aftershocks distributed on a plane, λ_3 will equal zero and the corresponding eigenvector $\hat{\mathbf{u}}_3$ will define the normal to the plane. In realistic cases where $\lambda_3 > 0$, $\hat{\mathbf{u}}_3$ represents the plane for which there is maximum variance reduction. The strike of the best fitting plane shown in Figure 10*a* is 146°, nearly perpendicular to the Kuril Trench. Figure 10*b*, which is a view down strike, shows that its dip is steep ($\delta = 84°$) and that the aftershocks extend over a vertical distance of nearly 100 km. The best fitting plane appears to be the fault plane of the main event, since it corresponds to one of the nodal planes determined from the first motions and from the moment tensor inversion of G. Masters and F. Gilbert (unpublished material, 1982).

Most of the deeper events are probably in the descending slab. Estimates of the depth of the seismic zone, presumably associated with the top part of the slab, are between 100 and 150 km in the vicinity of the epicenter of this event [*Isacks and Molnar*, 1971; *Veith*, 1974]. This puts the main shock near the top of the slab with the shallow aftershocks in the overriding Eurasian plate and the deeper aftershocks in the subducted portion of Pacific plate. Assuming that the deeper aftershocks represent the spatial extent of the main event and estimating the lithospheric thickness to be not more than about 100 km [*Yoshii*, 1975; *Leeds*, 1975], we infer that the Kuril earthquake probably represents a rupture which originated near the top of the slab and propagated downward, fracturing the entire lithosphere. Because of the presence of shallower shocks, the possibility of an upward rupture into the overlying plate cannot be ruled out, although these events seem to be less directly related to the main event. Since the mechanism is consistent with the steeply dipping Kuril segment of the slab dropping with respect to the shallowly dipping North Honshu segment, this event probably represents 'hinge' or 'tear' faulting, as discussed by *Isacks and Molnar* [1971]. This kind of faulting has been hypothesized to take place in the Hokkaido corner, and several investigators have reported the existence of such events [*Stauder and Mualchin* 1976; *Sasatani*, 1976].

The aftershocks of the Kuril Islands earthquake suggest that the low-frequency centroid may actually be deeper than the ISC depth of 118 km. To see how this might affect the moment spectrum, we reinverted the data using a depth of 150 km, near the aftershock centroid. The results in Figure 9*b* show that there is little change in the shape of the spectrum compared to Figure 9*a*, although most of the moment estimates are shifted slightly downward. From this inversion we find that $M_0^{\dagger} = 3.6 \pm 0.2$ A and $\tau_c = 52 \pm 2$ s. These latter values are listed in Table 3.

Tonga

The Tonga earthquake of June 22, 1977, occurred at the south end of the Tonga Arc approximately 150 km west of the trench. It was a very large ($M_s = 7.2$) normal-faulting event (G. Masters and F. Gilbert, unpublished material, 1982; J.W. Given, personal communication, 1982) with the steeply dipping nodal plane, presumably the fault plane, striking parallel to the trench axis. There is some disagreement in the literature about the depth of this event. The NEIS and ISC estimates are 65 and 69 km, respectively; however, *Talandier and Okal* [1979] suggested a depth of less than 50 km, based on readings of *pP-P* times at stations of the Polynesian network. They conclude that the event occurred above the descending slab and was not related to the subduction process. On the other hand, the locations of aftershocks by the ISC for the 3-week interval following the event indicate that faulting took place over a substantial depth range of more than 150 km (Figure 11). In Figure 11*b*, significant aftershock activity shallower than the main event is evident, but there are also five aftershocks below

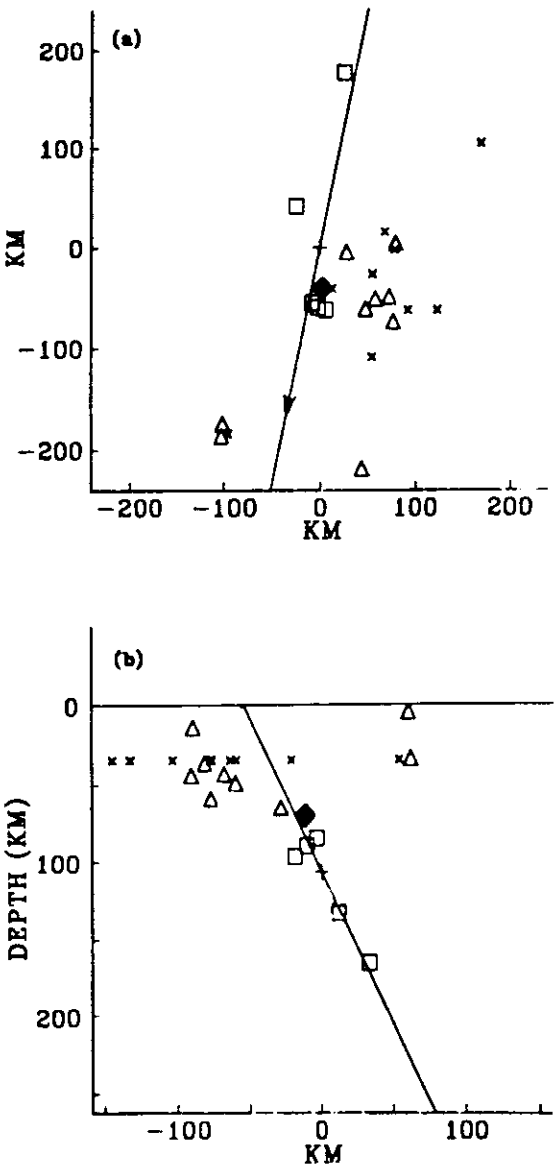

Fig. 11. (*a*) Map view of 3-week aftershock distribution for the Tonga earthquake; locations are from the ISC bulletins. Solid diamond denotes main event; squares and triangles represent events shallower and deeper than the main event, respectively; crosses correspond to events located at the default depth of 33 km. Line is the strike of best fitting plane to the main event and deeper aftershocks. (*b*) Vertical cross section of the aftershock distribution in the plane perpendicular to the best fitting plane, whose intersection is indicated by the solid line.

the main event extending to a depth of 166 km. These deeper events appear to be directly related to rupture process of the main event. The best fitting plane characterizing the main shock and deeper aftershocks is indicated on Figures 11*a* and 11*b*; this plane, with a strike of $\phi_s = 192°$ and dip of $\delta = 53°$, is in good agreement with the nodal plane of $\phi_s = 200°$ and $\delta = 70°$ found by J.W. Given (personal communication, 1982) from first motions. The depth to the seismic zone appears to be about 60 km near the epicenter of the main event [*Mitronovas et al.*, 1969], suggesting that the main event was near the top of the slab. If true, it implies that as in the case of the Kuril event, there was a downward rupture through much of the oceanic lithosphere.

Moment estimates for the Tonga earthquake were made using three different depths: 33, 100, and 65 km, which roughly correspond to the aftershock centroids for events above 65 km, events below 65 km, and all of the events, respectively. The results for $h = 33$ km are shown in Figure 12*a*. The moment spectrum is somewhat jagged, characterized by a low point at 1–2 mHz and a steep descent between 5 and 9 mHz; it yields a static moment of 24 ± 2 A and a characteristic time of 44 ± 3 s. For a depth of 100 km we obtain the moment spectrum shown in Figure 12*c*, which exhibits a much stronger frequency dependence, nearly an 80% drop across the band, and gives $M_T^f = 23 \pm 2$ A and $\tau_c = 84 \pm 2$ s. Our preferred depth of 65 km yields the moment spectrum shown in Figure 12*b*; it possesses a frequency dependence between the two extreme cases and implies $M_T^f = 23 \pm 2$ A and $\tau_c = 66 \pm 2$ s. *Talandier and Okal* [1979] obtained a value of $M_T = 15$ A using Rayleigh waves at about 5 mHz from the station PPT and a source depth presumably between 45 and 50 km. Their value of moment is in general agreement with our estimates at this frequency.

Tumaco

The Tumaco earthquake of December 12, 1979, took place on the continental shelf just seaward of the Colombia-Ecuador border. It was a very large thrust event with one steep and one shallow nodal plane, both striking roughly parallel to the axis of the Colombia trench [*Kanamori and Given*, 1981; *Herd et al.*, 1981]. The event caused extensive subsidence on the coast of Colombia, up to 1.6 m along a 200 km length of coastline, as well as uplift offshore on the continental shelf; it also generated a tsunami [*Herd et al.*, 1981]. The ISC bulletin puts the source depth at 29 km. Based on the refraction study of *Meyer et al.* [1976] in this region, the event appears to be near the boundary between the subducting Nazca plate and overriding South American plate; the shallow dipping nodal plane has been interpreted as the fault plane along which the underthrusting of the Nazca plate is presumably taking place [*Herd et al.*, 1981; *Kanamori and McNally*, 1982].

An inversion for total moment based on the source depth of 29 km is shown in Figure 13*b*. We observe a rapid roll-off of the moment spectrum between 2 and 11 mHz, resulting in about a factor of 3 decrease across this band. The point at 1–2 mHz is somewhat smaller than the other low-frequency (2–6 mHz) estimates; a low SNR does not seem to be the cause since the event was very

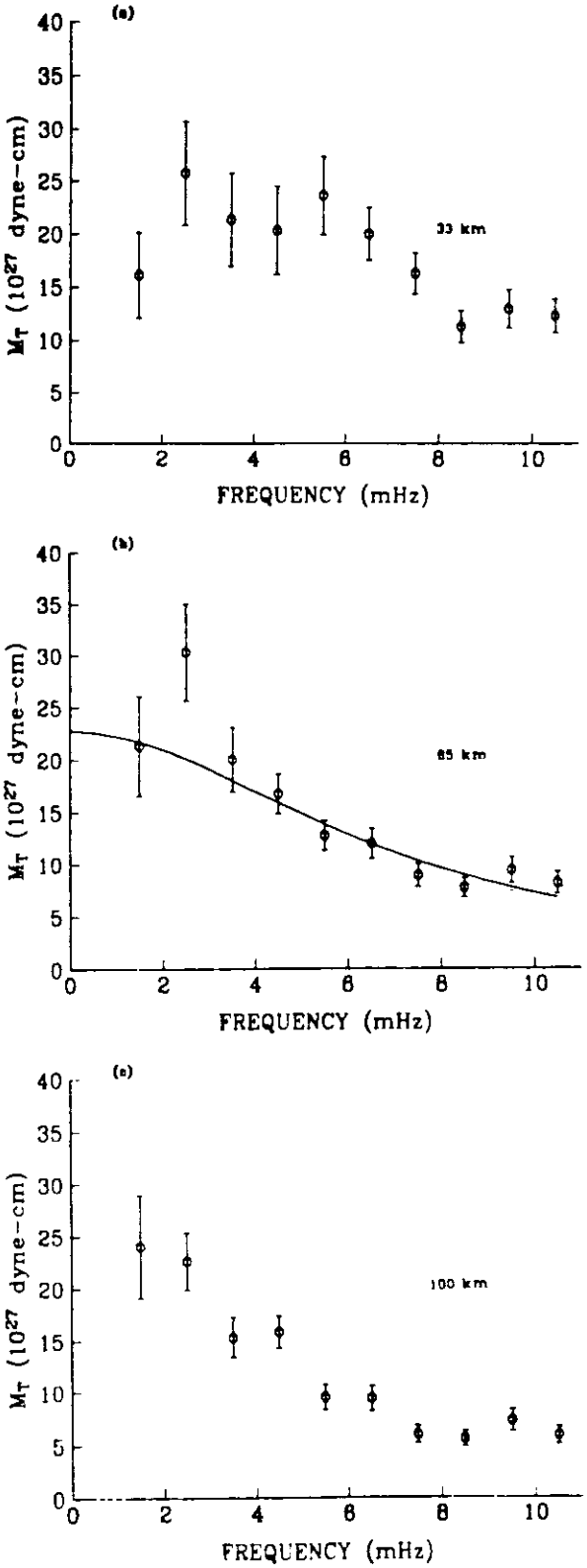

Fig. 12. Estimates of total moment averaged over 1-mHz bands for the Tonga earthquake of June 22, 1977, assuming focal depths of 33 km (*a*), 65 km (*b*), and 100 km (*c*). Error bars represent one standard deviation. The curve in Figure 11*b* corresponds to $M_T^f = 23$ A and $\tau_c = 66$ s.

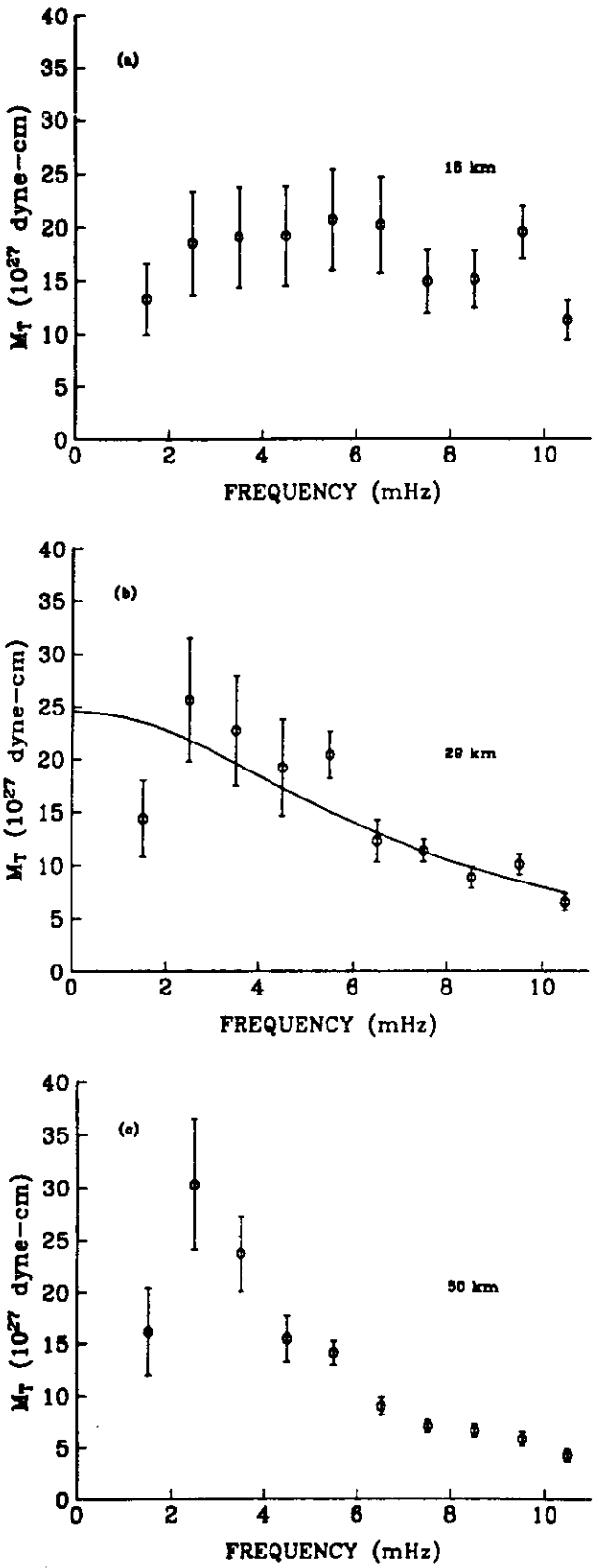

Fig. 13. Estimates of total moment averaged over 1-mHz bands for the Tumaco, Colombia, event of December 12, 1979, assuming focal depths of 15 km (*a*), 29 km (*b*), and 50 km (*c*). Error bars represent one standard deviation. The curve in Figure 13*b* corresponds to of $M\mathfrak{f} = 25$ A and $\tau_c = 65$ s.

energetic in this band. The static moment obtained from the spectrum in Figure 13*b* is $M\mathfrak{f} = 25 \pm 2$ A, and the characteristic time is $\tau_c = 65 \pm 2$ s. *Kanamori and Given* [1981] retrieved the moment tensor for this event using a depth of 33 km and obtained results in general agreement with ours. They find a value of $M\mathfrak{f} = 29$ A and nearly the same source duration, $\tau_c = 66$ s.

There is some indication from the aftershock study of C. Mendoza and J.W. Dewey, (manuscript in prepartion, 1982) that the depth of the low-frequency centroid was somewhat less than 29 km. They locate most of the shocks shallower than the main event and closer to the trench, suggesting an upward component of rupture along the plate boundary toward the trench axis. Putting the source centroid at 15 km yields the moment estimates shown in Figure 13*a*, which show a much diminished frequency dependence. However, the hypothesis that significant faulting may have taken place deeper than 29 km cannot be entirely ruled out. In the first 7 days after the main event, the ISC located more than 10 aftershocks in the depth range 40–75 km which were not assigned depths by C. Mendoza and J.W. Dewey (manuscript in preparation, 1982). To investigate how a deeper source centroid would affect the moment estimates, we reinverted the data, using a depth of 50 km. The results in Figure 13*c* show a spectrum with an increased frequency dependence in comparison to Figures 13*a* and 13*b*, yielding a reduction in moment of about 80% between 2 and 11 mHz. Given the fact that aftershocks occurred both above and below the initial hypocenter, we prefer the centroid depth of 29 km and have used the corresponding values of $M\mathfrak{f}$ and τ_c in Table 3.

The aftershocks also indicate that the Tumaco event ruptured unilaterally as much as 250 km to the northeast (C. Mendoza and J.W. Dewey, manuscript in preparation, 1982). The NEIS epicenter for this event, used to generate the transfer functions, presumably represents the point of rupture initiation and could thus be more than 100 km away from the low-frequency centroid. To examine the possible effect on moment of this rather sizeable error, we inverted synthetic data generated using the mechanism in Table 2 and an epicenter 115 km to the northeast of the location listed in Table 1. The resulting errors in total moment were no more than about 10% and would not significantly bias the estimates of $M\mathfrak{f}$ and τ_c.

Honshu

The Honshu earthquake of March 7, 1978, was a deep-focus ($h = 439$ km) event occurring 250 km west of the Bonin Islands. At the latitude of this event (32°N) the seismic zone is fairly continuous from the surface down to a depth of about 450 km, where seismicity ceases [*Katsumata and Sykes*, 1969]; the Honshu event is thus near the bottom of this zone. As commonly observed for deep-focus events [e.g., *Fukao*, 1972; *Sasatani*, 1980], the earthquake was a complex event, with a small foreshock preceding the main rupture sequence by about 7 s. This event has been previously examined by SJ (Figure 14). The best fitting theoretical spectrum yields a zero-frequency moment of $M\mathfrak{f} = 0.52 \pm 0.04$ A and a characteristic duration of $\tau_c = 32 \pm 4$ s. The moment estimates in Figure 14 are in reasonable agreement with other inves-

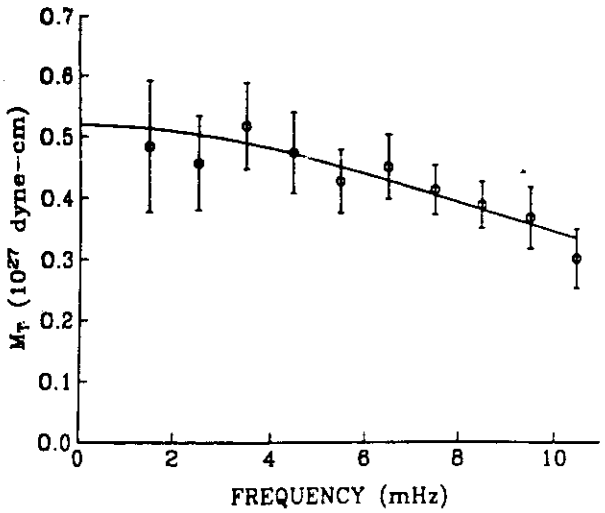

Fig. 14. Estimates of total moment averaged over 1-mHz bands for the Honshu event of March 7, 1978. Error bars represent one standard deviation. The curve corresponds to $M\hat{f} = 0.52$ A and $\tau_c = 32$ s.

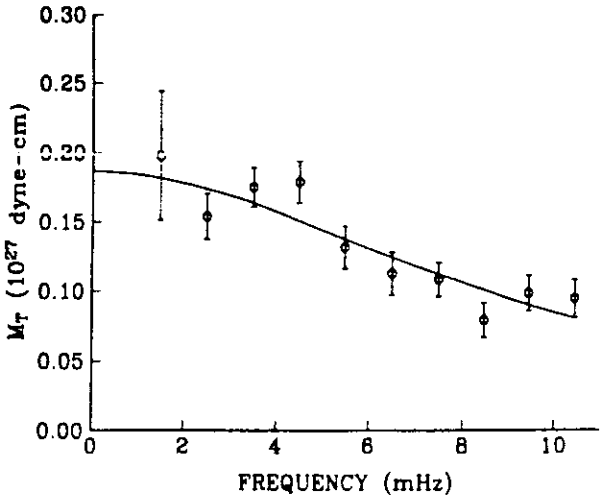

Fig. 16. Estimates of total moment averaged over 1-mHz bands for the Argentina event of October 22, 1977. Error bars represent one standard deviation. The curve corresponds to $M\hat{f} = 0.19$ A and $\tau_c = 43$ s; first point of diagram was not used in its determination.

tigations of this event. For example, G. Masters and F. Gilbert (unpublished material, 1982) obtained $M_T = 0.64$ A in the interval 2–5 mHz. At a somewhat higher frequency (16 mHz), *Dziewonski et al.* [1981] obtained a total moment of 0.40 A using body waves from the SRO network, consistent with the estimates at the high end of our band.

Banda Sea

The Banda Sea event of February 21, 1978, took place in one of the most tectonically complex regions of the world. Based on the spatial distribution of seismicity, *Cardwell and Isacks* [1978] proposed the existence of two lithospheric plates descending beneath the Banda Sea. One of these plates represents a laterally continuous slab being simultaneously subducted beneath the east-west trending Java Trench and Timor Trough and the north-south trending Aru Trough, with a lateral bend of about 90° at the juncture of these two sections. The second plate dips to the southwest and is associated with subduction under the Seram Trough. The Banda Sea event is located near the northern boundary of the first plate at a depth of 510 km, where the plate dips shallowly to the west [cf. *Cardwell and Isacks*, 1978, Figure 5]. The event represents normal faulting (G. Masters and F. Gilbert, unpublished material, 1982) with the tension axis trending north-south, parallel to the local strike of the slab. *Cardwell and Isacks* [1978] suggested that the events in this part of the slab are related to the lateral bending of the plate and state that such bending would lead to the generation of stresses consistent with the direction of the tension axis for this earthquake. The Banda Sea event was preceded by a foreshock ($m_b = 5.9$) by about 50 s.

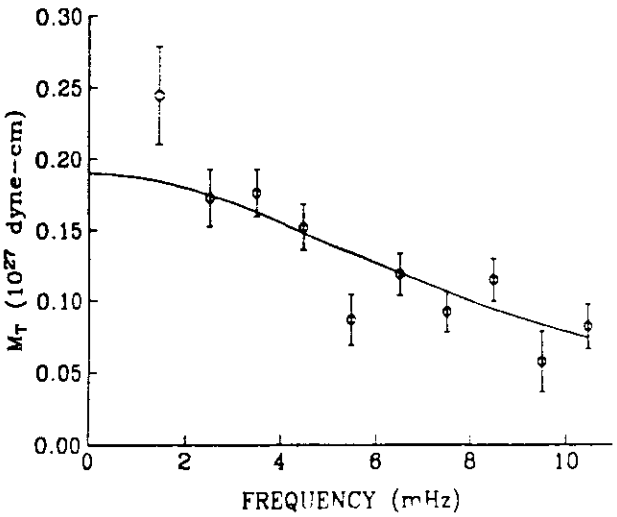

Fig. 15. Estimates of total moment averaged over 1-mHz bands for the Banda Sea event of February 21, 1978. Error bars represent one standard deviation. The curve corresponds to $M\hat{f} = 0.19$ A and $\tau_c = 54$ s; first point of diagram was not used in its determination.

The moment estimates are plotted in Figure 15. Although there is some scatter, evidently due to the low SNR, a fairly rapid decrease in moment across the frequency band is apparent, corresponding to a long source duration of $\tau_c = 54 \pm 3$ s. We obtain a static moment of $M\hat{f} = 0.19 \pm 0.01$ A, in agreement with the value of $M_T = 0.19$ A between 2-5 mHz found by G. Masters and F. Gilbert (unpublished material, 1982).

Argentina

The deep-focus seismicity in South America is restricted to two linear zones trending north-south: one beneath western Brazil and one beneath western Argentina. The event of October 22, 1977, occurred in the latter. Like the Honshu and Banda Sea events, it was preceded by a small foreshock ($m_b = 5.3$) 150 s before the main event. The moment spectrum plotted in Figure 16 exhibits a fairly strong frequency dependence, rolling off by nearly a factor of 2 across the band. We obtain a characteristic time of $\tau_c = 43 \pm 4$ s and a static moment of $M\hat{f} = 0.19 \pm 0.02$ A.

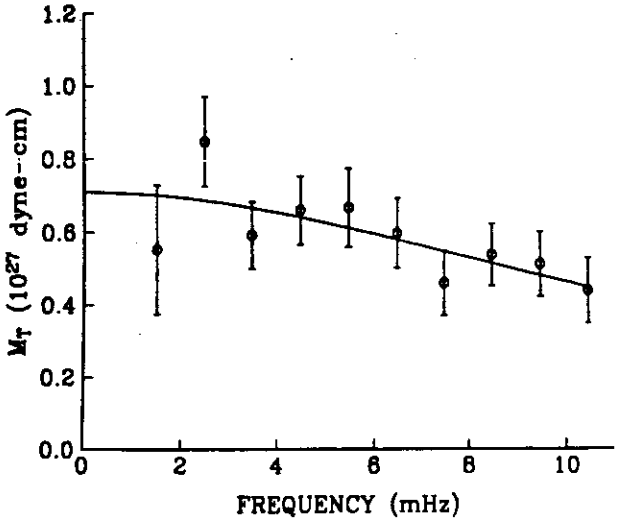

Fig. 17. Estimates of total moment averaged over 1-mHz bands for the Colombia event of November 23, 1979. Error bars represent one standard deviation. The curve corresponds to $M_0^f = 0.71$ A and $\tau_c = 33$ s.

Colombia

This intermediate-focus, oblique-normal-faulting event [*Dziewonski et al.*, 1981] occurred in the Cauca segment of the oceanic lithosphere subducting beneath Colombia; the seismic zone is characterized by an abrupt cessation of seismicity around 200-km depth. Its moment spectrum, presented in Figure 17, shows a gradual decrease with frequency, representing about 35% drop across the band. The best fit of (22) to the moment estimates gives a characteristic time of $\tau_c = 33 \pm 5$ s and a static moment of $M_0^f = 0.71 \pm 0.06$ A. *Dziewonski et al.* [1981] examined this event using body wave data from the SRO network. Their static-moment estimate of $M_0^f = 0.81$ A, made at 16 mHz but corrected back to zero frequency using the directivity model of *Ben-Menahem* [1961], is in agreement with our value; however, their estimate of source duration, $\tau_c = 14$ s, is significantly less than ours.

Miyagi-Oki

The Miyagi-Oki earthquake of June 12, 1978, was a shallow focus thrust [*Kanamori and Given*, 1981] located off the Pacific coast of the Miyagi prefecture in northeastern Japan. *Seno et al.* [1980] found that it comprised two shocks of roughly equivalent size, separated by 11 s. Our results are shown in Figure 18. The moment estimates decrease with frequency, dropping by about 30% across the band. Although the points between 1 and 5 mHz have relatively large errors, the decrease appears to be real; we obtain a source duration of $\tau_c = 32 \pm 6$ s and a zero-frequency moment of $M_0^f = 2.1 \pm 0.3$ A. The latter compares well with the static moment of 1.9 A obtained by *Kanamori and Given* [1981], although their preferred value for the source duration ($\tau_c = 19$ s) is somewhat smaller than ours. *Seno et al.* [1980] also estimated the moment of this event using surface waves from WWSSN stations in the frequency interval 5-10 mHz, obtaining 3.1 A, significantly larger than our estimates.

Iran

The Iran earthquake of 1978 yielded an unusual moment spectrum. As seen in Figure 19, it is more-or-less flat between 2 and 6 mHz but falls off by about a factor of 2 between 6 and 9 mHz. The reason for the very low moment estimate between 1 and 2 mHz is not entirely clear, although the SNR in this band is much less than in any of the others; this point was not used in the estimation of M_0^f and τ_c.

There is some disagreement about the depth of this event. The ISC gives a value of 34 km based on *pP-P* times; however, *Berberian et al.* [1979] found that all of the aftershocks they located fell between 2 and 24 km depth with the highest concentration between 5 and 10 km. The hypocentral depth used for the estimates in Figure 19 is 7 km, roughly corresponding to the aftershock centroid. Using 33 km yields a less physical spectrum with a prominent peak between 4 and 6 mHz, suggesting that the 7-km depth is more appropriate.

The best fitting theoretical spectrum corresponds to a static moment of $M_0^f = 1.3 \pm 0.2$ A and a characteristic time of $\tau_c = 43 \pm 5$ s. *Niazi and Kanamori* [1978] investigated this using IDA surface wave data at 4 mHz; they determined a static moment of $M_0^f = 1.5$ A, in good agreement with our results. Also in agreement is *Berberian's* [1979] value of $M_T = 1.3$ A, derived from field observations. *Niazi and Kanamori* [1981] made a moment estimate using body waves from six WWSSN long-period instruments and found $M_T = 0.82$ A, roughly a factor of 2 smaller than their determination of static moment. This high-frequency value is consistent with our estimates above 7 mHz.

DISCUSSION

We have chosen to represent the basic information contained in the low-frequency moment spectrum by the static moment and characteristic duration of the seismic process. While these two parameters are potentially useful in constraining the kinematic and the dynamic properties

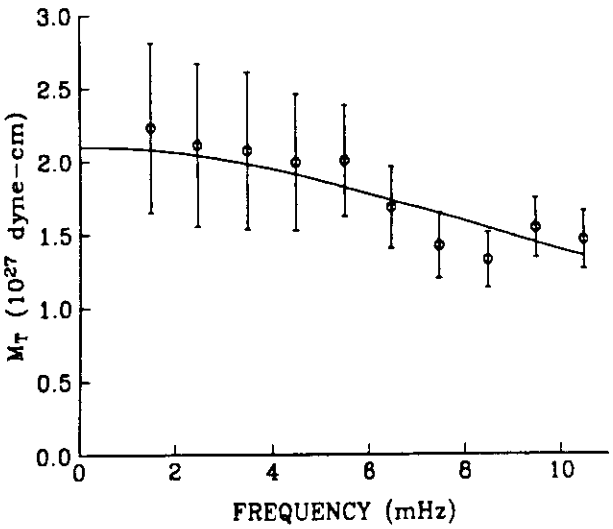

Fig. 18. Estimates of total moment averaged over 1-mHz bands for the Miyagi-Oki Japan event of June 12, 1978. Error bars represent one standard deviation. The curve corresponds to $M_0^f = 2.1$ A and $\tau_c = 32$ s.

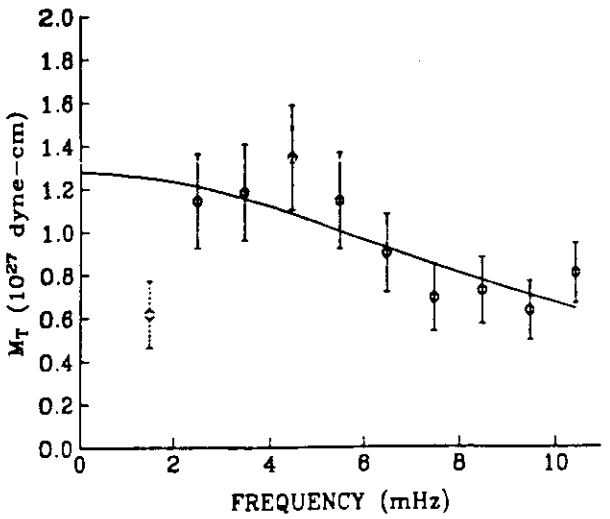

Fig. 19. Estimates of total moment averaged over 1-mHz bands for the Tabas, Iran, event of September 16, 1978. Error bars represent one standard deviation. The curve corresponds to $M_T^0 = 1.3$ A and $\tau_c = 43$ s; first point of diagram was not used in its determination.

of the source, it is important to understand the possible sources of bias in their estimation. *Patton and Aki* [1979] have examined this problem in the context of moment tensor retrieval, and most of the same error processes affect the determination of scalar moment as well. We have attempted to account for some of the important errors directly in the inversion algorithm: ambient seismic noise, incorrect transfer functions (because of lateral heterogeneity), and incomplete knowledge of the source mechanism. These have been used to place standard errors on the bias-corrected moment estimates, as discussed by SJ, and ultimately to determine the uncertainties in M_T^0 and τ_c.

Certain types of the errors not explicitly considered are more serious than others. Error processes which are uncorrelated from one frequency band to the next tend to roughen the spectrum; these should not greatly affect the estimates of M_T^0 and τ_c, which depend on the smoother properties of the spectrum. The error bars derived from the inversion procedure seem to adequately account for the fluctuations in estimates of M_T from one band to the next, as shown in the plots of moment spectra presented in the previous section. However, sources of bias highly correlated in frequency can substantially bias the estimates of static moment and source duration, and these must be assessed before attempting an interpretation of our results.

The utilization of an incorrect radial earth model (i.e., one which differs from the spherically averaged earth) will induce errors in the degenerate frequency $\bar{\omega}$, excitation amplitude A, and quality factor Q of each normal mode of vibration. While the moment estimates made by our procedure are insensitive to perturbations in $\bar{\omega}$, the relative errors in M_T are approximately proportional to the relative errors in A and Q (SJ); i.e.,

Error in A

$$\Delta M_T/M_T \sim \Delta A/A \tag{24}$$

Error in Q

$$\Delta M_T/M_T \sim \Delta Q/2Q \tag{25}$$

Estimates of the error in A are difficult to obtain from observations, since the amplitude of a mode peak depends on many factors, including the source mechanism and moment of the event. We can, however, get an indication of the size of this effect by comparing the amplitudes predicted by various published earth models; numerical experiments suggest that this error is probably not more than 5%. The relative error in moment due to Q is probably small as well. The Q model used in this study [*Masters and Gilbert*, 1983] is based on a large, high-quality, fundamental mode data set and should be able to predict average fundamental mode Q's to within 5%. The overtone modes, which make a significant contribution to the seismograms of the three deep-focus events above 6 mHz, have Q's which are less well known, but comparisons between the *Masters and Gilbert* [1983] model and the available overtone Q measurements suggest that $\Delta Q/2Q$ is probably less than 10% for the majority of these modes. It is unlikely that a large frequency-dependent bias in total moment would result from errors of this magnitude, especially because the most uncertain quality factors are associated with high-Q modes whose contributions to the seismogram are small and whose decay times are generally longer than the record lengths used in this study (10 hour).

The variations in the frequencies, amplitudes, and quality factors caused by aspherical heterogeneity are much larger than those attributable to an incorrect radial structure, but their effects on total-moment estimates can be reduced to a considerable degree by properly averaging over the station network. We have explicitly accounted for such fluctuations in formulating our optimization algorithm and assigning bias corrections and nominal errors to our moment estimates (SJ). Despite these efforts, the effects of aspherical heterogeneity on the seismogram are complex and not well understood, so we cannot preclude the possibility that some frequency-dependent bias remains.

An advantage of our method is that the estimates of the total moment, and hence source duration, are independent of the temporal centroid of the event (SJ). However, an incorrect spatial centroid can lead to bias in the moment spectrum. Our estimates are made assuming a source centroid obtained from other studies, usually a first-motion location (NEIS or ISC) representing the initiation of rupture. As discussed by *Dziewonski et al.* [1981], this does not necessarily correspond to the low-frequency centroid, which is an average of the entire seismic process. Errors in epicentroidal location will cause 'dephasing' of the cross spectra $U_{pq}(p \neq q)$ with respect to the transfer functions which will, on the average, lead to an apparent roll-off in the moment spectrum. In contrast, the power spectra U_{pp} are insensitive to this kind of error. The synthetic experiment mentioned in our discussion of the Tumaco event indicates that a rather sizeable error of 115 km in the epicentroid would give rise to only a 10% drop in moment across the 1-11 mHz band, much less than the 70% drop

observed for this event. Hence, the overall effect of epicentroidal mislocation appears to be small.

The effect of an incorrect hypocentroidal depth is much more important and probably represents the most serious source of bias not explicitly considered in the inversion procedure. When an incorrect depth leads to a nonphysical moment spectrum, as in the case of Sumbawa (event 5), this sensitivity can be used to constrain the centroid. However, in other cases (e.g., Kuril, 6; Tonga, 7; Tumaco, 8) the shape of the spectrum does not provide a depth discriminant. As discussed in the previous section, we performed an inversion using our best estimate of the low-frequency centroid (derived from the aftershock distribution, detailed source studies, etc.) and then varied the depth to ascertain the sensitivity of the parameters M_T^0 and τ_c to this assumption. For these larger events, the uncertainties are, of course, substantially increased over the nominal values quoted in Table 3. For the rest of the events, location does not appear to be as much of a problem because of stronger constraints on the depth or reduced sensitivity. For example, a perturbation of ± 20 km in the assumed depth of the three deep-focus events produced no significant change in their static moments or source durations.

For us to be able to determine a moment spectrum reliably from IDA data in the band 1-11 mHz, an earthquake must be effective in exciting the earth's free oscillations. In our experience this places a lower limit of about $M_T = 0.1$ A on the event's size. Below this level we begin to have problems with SNR, and our error estimates no longer adequately reflect the bias and variance of the total-moment estimates. The two smallest events in the survey, Banda Sea (event 10) and Argentina (event 11) ($M_T^0 = 0.19$ A), approach this limit and do, in fact, show a larger scatter than to the other events studied. However, for events smaller than 0.1 A, it is often still possible to retrieve single-band moment estimates in the interval 3-5 mHz, where the SNR is typically highest. As an example, we calculated $M_T = 0.08 \pm 0.02$ A in this band for the October 15, 1979, Imperial Valley earthquake, a value consistent with other studies [e.g., *Olson*, 1982; F. Wyatt, unpublished manuscript, 1982].

A final problem with bias has to do not so much with the estimates of the spectral parameters M_T^0 and τ_c as with their nominal uncertainties, listed in Table 3. In the regression fit of (22) to the observed moment spectra we have assumed that the errors in individual moment estimates are uncorrelated. Although the cross-spectral integrals (14) are taken over disjunct 1-mHz bands, this is not in general true, primarily because the mean squared modeling error defined by (21) involves the statistics of the source mechanism, which are assumed to be the same for all estimates from a particular event. To the extent that the matrices $\tilde{\mathbf{C}}$ are slowly varying from band to band, these modeling errors, and hence the errors in $\tilde{M}_T$, will be correlated. Evidence for this correlation can be seen directly in the total-moment spectra: with some exceptions (e.g., event 10), the scatter in the estimates is not as large as might be expected from their assigned errors. Consequently, the errors in M_T^0 and τ_c will tend to be underestimated; especially the errors associated with large value of τ_c because these depend more strongly on the variations with frequency. A quantitative assessment of the relative contribution of modeling error to the total error suggests that for $\tau_c > 30$ s the errors in τ_c should be multiplied by at least a factor of 2. Of course, even with this adjustment, these errors do not account for the possible sources of frequency-dependent bias discussed above.

INTERPRETATION OF FREQUENCY DEPENDENCE

By basing our definition of the total-moment spectrum on a frequency-dependent moment rate tensor $\mathbf{M}(\omega)$, we have implicitly assumed that the seismic source is localized in space but not in time. The low-frequency roll-off of the moment spectrum is thus interpreted in terms of the interference of seismic waves excited at different times, and the parameter τ_c is interpreted as a measure of the event's duration. *Backus* [1977*a*, *b*] has pointed out that a consistent representation of the seismic source should allow for extension in both the temporal and spatial coordinates; the interference of signals excited at different points on a fault of finite length can produce a frequency dependence even in the (unphysical) case of an instantaneous event. Hence, our procedures determine only an apparent source duration, $\tilde{\tau}_c$, which measures both the temporal and spatial extent of the earthquake process.

This problem is addressed in the appendix through an analysis of the second central moments of the glut-rate tensor $\dot{\Gamma}(\mathbf{r},t)$. For a long, thin fault modeled as a horizontal line source of characteristic length L_c whose excitation is dominated by surface waves with phase velocity c, we obtain the asymptotic result (equation (A19))

$$\tilde{\tau}_c = (\tau_c^2 + L_c^2/2c^2)^{1/2}$$

Rewriting this expression in terms of a characteristic velocity (apparent rupture velocity) $\nu_c \equiv L_c/\tau_c$ (equation (A20)),

$$\tilde{\tau}_c = \tau_c\,(1 + \nu_c^2/2c^2)^{1/2}$$

we see that, for 'fast' events ($\nu_c \simeq c$), the apparent source duration exceeds the characteristic time by only 20% or so. For 'slow' events, corresponding to large values of τ_c, the effect is even less. Therefore in the interpretation of apparent source duration, the contributions of higher spatial moments arising from the horizontal extent of the source appear to be relatively unimportant.

The analysis of vertical propagation is not so straightforward and must be addressed by numerical methods. Order-of-magnitude calculations are discussed in the appendix for the Kuril Islands and Tonga earthquakes, two events whose aftershocks distributions suggest faulting over a substantial depth range (~100 km) and whose moment spectra show significant roll-off (Figures 9 and 11). We estimate that the decrease in moment from 1 to 11 mHz directly attributable to the vertical extent of these sources is only about 10%, much less than the 60 — 70% observed.

The results of our analysis suggest the difference between $\tilde{\tau}_c$ and τ_c can be ignored, at least for the preliminary comparisons made in this paper. The characteristic

time τ_c is plotted against the logarithm of static moment M_T^s in Figure 20. In addition to the 14 events presented here, we have included the 1970 Colombia and 1963 Peru-Bolivia deep-focus events analyzed by *Gilbert and Dziewonski* [1975], whose observed moment spectra and best fitting theoretical spectra are displayed in Figure 1. (The error bars in Figure 20 are the standard errors taken from Table 3, but as discussed in the previous section, the nominal uncertainties attached to τ_c are likely to be biased to low values for events with large characteristic times.) We have also included on this plot an empirical relation between τ_c and M_T^s derived from Table III of *Kanamori and Given* [1981]. This empirical relation is based on the proportionality between M_T^s and the characteristic source volume and assumes a scaling velocity of 3.3 km/s. We use this curve as a convenient, albeit somewhat arbitrary, demarkation between 'fast' and 'slow' earthquakes.

It is interesting to note that while shallow and intermediate-focus events fall on both sides of the empirical curve, all five of the deep-focus earthquakes (events 9–11, PB, C) lie well within the slow field. This could be explained by a depth-dependent bias in the moment estimation procedures (which would have to apply to *Gilbert and Dziewonski*'s [1975] method as well as ours), but the hypothesis that deep events typically have large characteristic times merits consideration.

Each of the three deep-focus events analysed in this report was preceded by a foreshock, so we might inquire whether their large characteristic times are simply explained by this fact. A multiple earthquake comprising two instantaneous events with similar mechanisms separated by a time Δt has the spectrum

$$M_T(\omega) = M_T^s(1 + 2\epsilon \cos\omega\Delta t + \epsilon^2)^{1/2} \qquad (26)$$

where the static moment of the larger event is M_T^s and that of the smaller event is ϵM_T^s $(0 \leqslant \epsilon \leqslant 1)$. For the Honshu earthquake (event 9), $\Delta t \simeq 7$ s, which is too short an interval to explain the observed characteristic time of 32 ± 4 s. If the relatively small foreshock ($m_b = 5.3$) 150 s before the Argentina event were important, we would expect a prominent peak in moment a $1/\Delta t = 6.7$ mHz, but this is not observed. The somewhat more energetic foreshock ($m_b = 5.9$) occurring 50 s before the Banda Sea event would be expected to reduce the moment spectrum by an amount $2\epsilon/(1+\epsilon)$ at 10 mHz, compared to the static value. From the moment magnitude relation of *Hanks and Kanamori* [1979] we estimate $\epsilon \simeq 0.05$, which implies a drop in moment of less than 10% across the band — much less than the observed drop of nearly 50%. It does not appear therefore that the large characteristic times estimated for these deep-focus earthquakes can be explained solely by the foreshock activity.

The main rupture sequence of deep-focus events has been studied at high frequencies by many authors [e.g., *Wyss and Molnar*, 1972; *Strelitz*, 1975; *Sasatani*, 1980]. They have generally found short source durations and rapid rupture velocities. Our results and those of *Gilbert and Dziewonski* [1975] suggest that there may be a slow component to these events not detected at higher frequencies. For example, *Furumoto* [1977] performed a multiple-event analysis of the 1970 Colombia deep-focus earthquake using WWSSN body wave data and concluded that it comprised a sequence of seven shocks terminating abruptly after 47 s. If the rupture process involved a uniform moment release, the implied characteristic time is only $3^{-1/2} \times 47$ s $= 27$ s, nearly a factor of 4 less than that estimated from *Gilbert and Dziewonski*'s [1975] moment spectrum ($\tau_c \simeq 100$ s). A similar discrepancy exists for *Chandra*'s [1970] multiple-event analysis of the 1963 Peru-Bolivia event.

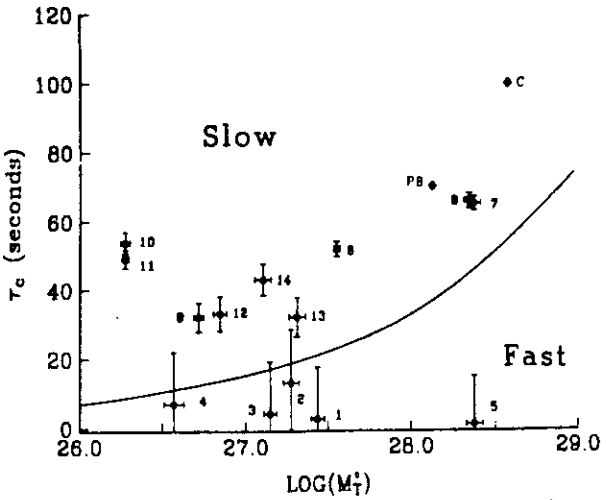

Fig. 20. Characteristic source time τ_c versus the garithm of static moment M_T^s. Solid circles with error bars represent the 14 events studied in this paper (Table 3); numbers correspond to those in Table 1. Solid diamonds represent the Colombia (C) and Peru-Bolivia (PB) earthquakes analyzed by *Gilbert and Dziewonski* [1975], whose moment spectra are displayed in Figure 1. The curve separating 'fast' and 'slow' fields is based on an empirical relationship between moment and source duration proposed by *Kanamori and Given* [1981].

A slow, perhaps precursive, component to the deep-focus rupture process is not implausible; indeed, *Dziewonski and Gilbert* [1974] and *Gilbert and Dziewonski* [1975] detected precursive, compressive strain release for both events they studied. We are currently investigating the isotorpic part of the deep-focus mechanism using algorithms designed to measure the isotropic moment M_I defined in (2). The tentative detection of an isotropic component to the 1978 Honshu event was reported by SJ.

The four largest events in this survey — Sumbawa (event 5, $M_T^s = 24 \pm 3$ A), Kuril Islands (event 6, $M_T^s = 3.6 \pm 0.2$ A), Tonga (event 7, $M_T^s = 23 \pm 2$ A), and Tumaco (event 8, $M_T^s = 25 \pm 2$ A) — span a wide range of characteristic times. The Sumbawa earthquake is fast ($\tau_c = 1 \pm 14$ s), whereas the other three are slow ($\tau_c = 52$–66 s). An interesting comparison among these events can be made in terms of their characteristic velocities v_c. The aftershock distribution for Sumbawa indicates a total fault length of about 100 km [*Fitch et al.*, 1981] or $L_c \simeq 60$ km; assuming that $\tau_c < 20$ s we find v_c is at least 3 km/s. The aftershock distributions for Tonga (Figure 11) and Tumaco C. Mendoza and J.W. Dewey, (manuscript in preparation, 1982) on the other hand, both suggest fault lengths of ~250 km, yielding $L_c = 144$ km and $v_c \simeq 2.2$ km/s. Finally, from a fault dimension of ~100 km for the Kuril Islands earthquake (Figure 10), we

calculate $v_c \simeq 1.2$ km/s, nearly a factor of 3 lower than Sumbawa.

The explanation of these differences in characteristic velocities is not well understood but invites speculation. The fastest event, Sumbawa, appears to have its spatial centroid above a depth of 25 km, suggesting that the rupture was confined to the upper, more brittle part of the oceanic lithosphere. The slowest event, Kuril Islands, occurred in an oceanic plate of comparable age and presumably thermal structure, but its aftershocks indicate a much greater penetration of the rupture downward into the lower, more ductile part of the lithosphere (Figure 10). The Tonga earthquake has nearly the same static moment as Sumbawa, yet a much greater characteristic time; it too appears to have ruptured through a substantial portion of the subducted oceanic plate and could represent a lithospheric-normal-faulting event of the type discussed by *Kanamori* [1971] and *Uyeda and Kanamori* [1979]. Hence, there may be a correlation between the time constants and depths of rupture for large earthquakes, the duration being generally greater for ruptures which propagate through the hot, ductile, lower lithosphere. Such a hypothesis is consistent with the observation that some transform fault earthquakes are slow events [*Kanamori and Stewart*, 1976], since they occur in regions where the lithosphere is thin and rupture into the more ductile portion of the plate is more likely.

APPENDIX

In this section we consider the influence of the spatial extent of the source on the moment spectrum $M_T(\omega)$ and, in particular, on the derived estimates of the characteristic time τ_c. For an arbitrary, indigenous, buried source, we can express a component of the seismogram at the p th station by

$$u_p(\omega) = \sum_{l,n,m} {}_nC_l(\omega)\ {}_ns_{lp}^m \int_V {}_n\mathbf{E}_l^{m*}(\mathbf{r}) : \dot{\Gamma}(\mathbf{r},\omega)\ d\mathbf{r} \qquad \text{(A1)}$$

$\dot{\Gamma}(\mathbf{r},\omega)$ is the Fourier transform of the stress glut rate tensor $\dot{\Gamma}(\mathbf{r},t)$ [*Backus and Mulcahy*, 1976*a*, *b*]; ${}_n\mathbf{E}_l^m(\mathbf{r})$ is the strain tensor of the normal mode identified by the indices n (radial order), l (angular order), and m (azimuthal order); ${}_ns_{lp}^m$ is its displacement eigenfunction evaluated at the pth station, and ${}_nC_l(\omega)$ is its resonance shape function. Contributions to the displacement arising from source tractions on surfaces of discontinuity, including the free surface, are ignored. If the source region is small compared to the wavelengths of interest, we can approximate $\dot{\Gamma}(\mathbf{r},t)$ by its zeroth-order spatial moment

$$\mathbf{M}(t) \equiv \mathbf{M}^{(0)}(t) = \int_V d\mathbf{r}\ \dot{\Gamma}(\mathbf{r},t) \qquad \text{(A2)}$$

giving us the familiar point-source approximation

$$u_p(\omega) = \sum_{k,m} C_k(\omega) s_{kp}^m \mathbf{E}_k^{m*}(\mathbf{r}_o) : \mathbf{M}(\omega) \qquad \text{(A3)}$$

where $\mathbf{r}_o$ is the source centroid and k represents the index pair (n,l).

Horizontal Line Source

For a sufficiently large source region, the higher spatial moments of the stress glut must be taken into account to represent the seismogram adequately, a point emphasized by *Backus* [1977*a*, *b*]. We initially consider the case of a source region extended in one horizontal direction but without appreciable depth extent. A convenient representation, employed by *Dziewonski and Romanowicz* [1977], is a line source taken to be a section of the equator of a spherical coordinate system (r,θ,ϕ) with centroid at the point $(r_o,\pi/2,0)$. Since the strain tensor $\mathbf{E}_l^m(\mathbf{r})$ depends on the variable ϕ only through an exponential factor $e^{im\phi}$, the seismogram for a horizontal line source can be written

$$u_p(\omega) = \sum_{km} C_k(\omega) s_{kp}^m\ \mathbf{E}_k^{m*}(\mathbf{r}_o)$$

$$: \sum_\eta \frac{1}{\eta!}\,(im)^\eta \mathbf{M}^{(\eta)}(\omega) \qquad \text{(A4)}$$

where $\mathbf{M}^{(\eta)}(\omega)$ is the ηth spatial moment of $\dot{\Gamma}(\mathbf{r},\omega)$,

$$\mathbf{M}^{(\eta)}(\omega) \equiv \int_V d\mathbf{r}\ \dot{\Gamma}(\mathbf{r},\omega)\ (\mathbf{r}-\mathbf{r}_o)^\eta \qquad \text{(A5)}$$

and $(\mathbf{r}-\mathbf{r}_o)^\eta$ is the outer product matrix

$$(\mathbf{r}-\mathbf{r}_o)\ (\mathbf{r}-\mathbf{r}_o)\cdots(\mathbf{r}-\mathbf{r}_o) \qquad \text{(A6)}$$

(η times). If $l >> n$, it is possible to approximate the sum over m in (A4) by the stationary phase method [*Jordan*, 1978], yielding the asymptotic formula

$$u_p(\omega) \simeq \sum_k \mathbf{G}_{kp}(\mathbf{r}_o,\omega)$$

$$: \sum_\eta \frac{1}{\eta!}(il\cos\Phi_p)^\eta\ \mathbf{M}^{(\eta)}(\omega) \qquad \text{(A7)}$$

where Φ_p is the angle between the line source and the great circle connecting the source centroid and the p th receiver, and

$$\mathbf{G}_{kp}(\mathbf{r}_o,\omega) \equiv \sum_m C_k(\omega) s_{kp}^m\ \mathbf{E}_k^m(\mathbf{r}_o)$$

is the tensor-valued transfer function appropriate to the point-source approximation (A3). The temporal moments of $\dot{\Gamma}(\mathbf{r},t)$ are generated by expanding each $\mathbf{M}^{(\eta)}(\omega)$ in a Taylor series about $\omega = 0$:

$$u_p(\omega) \simeq \sum_k \mathbf{G}_{kp}(\mathbf{r}_o,\omega)$$

$$: \sum_{\eta,\nu} \frac{(i)^{(\eta+\nu)}}{\eta!\nu!}(l\cos\Phi_p)^\eta\ \omega^\nu\ \mathbf{M}^{(\eta,\nu)} \qquad \text{(A8)}$$

Since we are considering long-period seismic waves, we keep only terms for which $\eta + \nu \leqslant 2$. The moments $\mathbf{M}^{(2,0)}$ and $\mathbf{M}^{(0,2)}$ contain information about the spatial and temporal extent of the source, respectively. It is convenient to consider a special class of source models which satisfy

$$\mathbf{M}^{(\eta,\nu)} = \mathbf{M}\,\mu^{(\eta,\nu)};\ \eta + \nu \leqslant 2 \tag{A9}$$

That is, the six independent components of $\dot{\Gamma}(r,t)$ have the same zeroth, first, and second moments; we refer to such an event as a synchronous source of degree 2. A special case of a synchonous source is one in which the source mechanism (taken here to be the normalized stress glut rate tensor $\dot{\Gamma}(\mathbf{r},t)/\|\dot{\Gamma}(\mathbf{r},t)\|$) is a constant function of position and time. The quantities $\mu^{(\eta,\nu)}$ in (A.9) are then the polynomial moments of the scalar function

$$f(\mathbf{r},t) \equiv \mathbf{M} : \dot{\Gamma}(\mathbf{r},t)/\|\mathbf{M}\|^2 \tag{A10}$$

which is a normalized measure of the spatial and temporal stress concentration in the source region [cf. *Backus*, 1977*a*]. Let a circumflex denote the moments taken with respect to the spatial and temporal centroids; i.e., $\hat{\mu}^{(1,0)} = \hat{\mu}^{(0,1)} = 0$. Then we can write the frequency averaged cross spectrum U_{pq} as

$$U_{pq} = U^o_{pq}\,\chi_{pq} \tag{A11}$$

where U^o_{pq} is the cross spectrum obtained for an instantaneous point source $\mathbf{M}^{(0,0)}$ and χ_{pq} includes the contributions of the second-order spatial and temporal moments:

$$\chi_{pq} = 1 - \omega^2\,\hat{\mu}^{(0,2)} - l\omega(\cos\Phi_p + \cos\Phi_q)\hat{\mu}^{(1,1)}$$

$$- \frac{1}{2}l^2\,(\cos^2\Phi_p + \cos^2\Phi_q)\hat{\mu}^{(2,0)} \tag{A12}$$

Here we have assumed the dominant contribution to U_{pq} is from a mode of angular order l. Approximating l by $\omega a/c$, where a is the radius of the earth and c is phase velocity, we can express (A12) in terms of the characteristic time

$$\tau_c = 2(\hat{\mu}^{(0,2)})^{1/2} \tag{A13}$$

a characteristic source length

$$L_c = 2a(\hat{\mu}^{(2,0)})^{1/2} \tag{A14}$$

and a 'directivity' parameter

$$D_c = a\hat{\mu}^{(1,1)} \tag{A15}$$

by writing

$$\chi_{pq} = 1 - \omega^2\{\frac{\tau_c^2}{4} + (\cos\Phi_p + \cos\Phi_q)\,\frac{D_c}{c}$$

$$+ (\cos^2\Phi_p + \cos^2\Phi_q)\,\frac{L_c^2}{8c^2}\} \tag{A16}$$

The expression for squared moment is

$$M_T^2 = \sum_{p,q} a_{pq}\,U_{pq} = \sum_{p,q} a_{pq}\,U^o_{pq}\chi_{pq} \tag{A17}$$

To estimate the effect for a station array uniformly distributed on the sphere, we average χ_{pq} over azimuth, assuming that Φ_p and Φ_q are uncorrelated. The terms proportional to D_c average to zero, and we obtain

$$M_T(\omega) = M_T^0\,\{1 - \frac{\omega^2}{4}\,(\tau_c^2 + L_c^2/2c^2)\}^{1/2}$$

$$\simeq M_T^0\{1 - \frac{\omega^2}{8}(\tau_c^2 + L_c^2/2c^2)\} \tag{A18}$$

Comparing with (22), we see that the effective source duration is approximately

$$\tilde{\tau}_c = (\tau_c^2 + L_c^2/2c^2)^{1/2} \tag{A19}$$

which can also be expressed in terms of a characteristic, or apparent rupture, velocity $v_c \equiv L_c/\tau_c$:

$$\tilde{\tau}_c = \tau_c(1 + v_c^2/2c^2)^{1/2} \tag{A20}$$

Equation (A20) illustrates that the effective source duration $\tilde{\tau}_c$ will be larger than the characteristic time τ_c by an amount which depends on the ratio v_c/c. For spheroidal modes in the band 1-11 mHz, $c \geqslant 4$ km/s. If we assume $v_c \leqslant 4\,km/s$, then an upper bound on the spatial contribution is given by

$$\tilde{\tau}_c = (3/2)^{1/2}\tau_c = 1.22\,\tau_c \tag{A21}$$

Thus $\tilde{\tau}_c$ could exceed τ_c by as much as 20% for a 'fast' event; in this case, however, the total-moment spectrum will be relatively flat, and τ_c will be small. The observational uncertainties associated with the characteristic times of fast events are typically much larger than 20% (Table 3). For slower events, such as the Tumaco earthquake (event 8) for which we estimate $v_c \leqslant 2.5$ km/s, $\tilde{\tau}_c$ will exceed τ_c by only 10% or less. The horizontal spatial extent of a source has, therefore, a relatively small effect on the estimation of characteristic times.

Vertical Line Source

The effect of a vertical source extent on $M_T(\omega)$ is less straightforward than in the simple horizontal case discussed above because the radial derivatives of the strain

tensor $\mathbf{E}_f^n(\mathbf{r})$ must be evaluated numerically. We write the integrated cross spectrum U_{pq} as the sum

$$U_{pq} = U_{pq}^o + \delta U_{pq}^{(0,2)} + \delta U_{pq}^{(1,1)} + \delta U_{pq}^{(2,0)} \quad \text{(A22)}$$

where $\delta U_{pq}^{(\eta,\nu)}$ is the perturbation associated with the (η,ν) th moment. The last term has the expression

$$\delta U_{pq}^{(2,0)} = \hat{\mu}^{(2,0)}\, \mathbf{m}^* \cdot \mathbf{H}_{pq}^{(2)} \cdot \mathbf{m} \quad \text{(A23)}$$

where, in analogy with (16),

$$\mathbf{H}_{pq}^{(2)} \equiv \tfrac{1}{2} \int_{\omega_a}^{\omega_b} [\partial_r^2\, \mathbf{g}_p^*(\mathbf{r}_o,\omega)\mathbf{g}_q(\mathbf{r}_o,\omega)$$

$$+ \mathbf{g}_p^*(\mathbf{r}_o,\omega)\partial_r^2 \mathbf{g}_q(\mathbf{r}_o,\omega)]\, d\omega \quad \text{(A24)}$$

The derivatives ∂_r^2 are evaluated at the spatial centroid $\mathbf{r}_o$. The effect of this term on the total moment estimated from a global array can be approximated by again averaging over all receiver positions on the surface of the sphere; we denote this average by $< \delta U_{pq}^{(2,0)} >$. As a measure of its magnitude we have computed the power spectrum ratio $< \delta U_{pf}^{(2,0)} > / 2 < U_{pp}^o >$ for the fundamental spheroidal modes using the source parameters of the Kuril Islands (event 6) and Tonga (event 7) events listed in Tables 1 and 2. Assuming that these events can be approximated by a vertical line source with a depth extent of 100 km, we find a drop in moment of about 6% for the former and 13% for the latter, which is much less than the decrease actually observed.

Acknowledgements. We thank members of the project of IDA team for high-quality data used in this study, particularly G. Masters and F. Gilbert, who provided us with edited time series and their unpublished moment-tensor estimates as well as codes for generating transfer functions. T.H.J. is an Alfred P. Sloan Foundation Fellow. This research was sponsored by the National Science Foundation under grants EAR80-07823 and EAR81-21866.

REFERENCES

Aki, K., Generation and Propagation of G waves from the Niigata earthquake of June 16, 1964, 2, Estimation of earthquake moment, released energy, and stress-strain drop from the G wave spectrum, *Bull. Earthquake Res. Inst., Univ. Tokyo, 44, 23-88*, 1966.

Aki, K., Scaling law of seismic spectrums, *J. Geophys. Res., 72*, 1217–1231, 1967.

Backus, G., Interpreting the seismic glut moments of total degree of two or less, *Geophys. J. R. Astron. Soc., 51*, 1–25, 1977*a*.

Backus, G., Seismic sources with observable glut moments of spatial degree two, *Geophys. J. R. Astron. Soc., 51*, 27–45, 1977*b*.

Backus, G., and F. Gilbert, Uniqueness in the inversion of inaccurate gross earth data, *Philos. Trans. R. Soc. London, Ser. A., 266*, 123–192, 1970.

Backus, G., and M. Mulcahy, Moment tensors and other phenomenological descriptions of seismic sources, I, Continuous displacements, *Geophys. J. R. Astron. Soc., 46*, 341–361, 1976*a*.

Backus, G., and M. Mulcahy, Moment tensors and other phenomenological descriptions of seismic sources, II, Discontinuous displacements, *Geophys. J. R. Astron. Soc., 47*, 301–329, 1976*b*.

Ben-Menahem, A., Radiation of seismic surface waves from finite moving sources, *Bull. Seismol. Soc. Am., 51*, 401–435, 1961.

Berberian, M., Earthquake faulting and bedding thrust associated with the Tabas-e-Golshan (Iran) earthquake of September 16, 1978, *Bull. Seismol. Soc. Am., 69*, 1861–1887, 1979.

Berberian, M., I. Asudeh, R. G. Bilham, C. H. Scholz, and C. Soufleris, Mechanism of the main shock and the aftershock study of the Tabas-e-Golshan (Iran) earthquake of September 16, 1978: A preliminary report, *Bull. Seismol. Soc. Am., 69*, 1851–1859, 1979.

Brune, J. N., Tectonic stress and the spectra of seismic shear waves from earthquakes, *J. Geophys. Res., 75*, 4997–5009, 1970.

Cardwell, R. K., and B. L. Isacks, Geometry of the subducted lithosphere beneath the Banda Sea in eastern Indonesia from seismicity and fault plane solutions, *J. Geophys. Res., 83*, 2825–2838, 1978.

Chael, E. P., and G. S. Stewart, Recent large earthquakes along the Middle American Trench and their implications for the subduction process, *J. Geophys. Res., 87*, 329–338, 1982.

Chandra, U., The Peru-Bolivia border earthquake of August 15, 1963, *Bull. Seismol. Soc. Am., 60*, 639–646, 1970.

Console, R., and P. Favali, Study of the Montenegro earthquake sequence (March-July 1979), *Bull. Seismol. Soc. Am., 71*, 1233–1248, 1981.

Dziewonski, A. M., and F. Gilbert, Temporal variation of the seismic moment tensor and the evidence of precursive compression for two deep earthquakes, *Nature, 247*, 185–188, 1974.

Dziewonski, A. M., and B. A. Romanowicz, An exact solution to the problem of excitation of normal modes by a propagating fault, in *Seismic Discrimination Semiannual Technical Summary*, Lincoln Laboratory, Massachusetts Institute of Technology, Cambridge, 1977.

Dziewonski, A. M., T. A. Chou, and J. H. Woodhouse, Determination of earthquake source parameters from waveform data for studies of global and regional seismicity, *J. Geophys. Res., 86*, 2825–2852, 1981.

Fitch, T. J., R. G. North, and M. W. Shields, Focal depths and moment tensor representations of shallow earthquakes associated with the great Sumbawa earthquake, *J. Geophys. Res., 86*, 9357–9374, 1981.

Fukao, Y., Source process of a large deep-focus earthquake and its tectonic implications — The western Brazil earthquake of 1963, *Phys. Earth Planet. Inter., 5*, 61–76, 1972.

Furumoto, M., Spacio-temporal history of the deep Colombia earthquake of 1970, *Phys. Earth Planet. Inter., 15*, 1–12, 1977.

Furumoto, M., Initial phase analysis of *R* waves from great earthquakes, *J. Geophys. Res., 84*, 6857–6874, 1979.

Gilbert, F., and A. M. Dziewonski, An application of normal mode theory to the retrieval of structural parameters and source mechanisms from seismic spectra, *Philos. Trans. R. Soc. London, Ser. A, 278*, 187–269, 1975.

Given, J. W., and H. Kanamori, The depth extent of the 1977 Sumbawa, Indonesia, earthquake (abstract), *Eos Trans. AGU, 61*, 1044, 1980.

Hanks, T. C., Deviatoric stresses and earthquake occurrence at the outer rise, *J. Geophys. Res., 84*, 2343–2347, 1979.

Hanks, T. C., and H. Kanamori, A moment magnitude scale, *J. Geophys. Res., 84*, 2348–2350, 1979.

Hartzell, S., Analysis of the Bucharest strong ground motion record from the March 4, 1977, Romanian earthquake, *Bull. Seismol. Soc. Am., 69*, 513–530, 1979.

Haskell, N. A., Total energy and energy density of elastic wave radiation from propagating faults, *Bull. Seismol. Soc. Am., 54*, 1811–1841, 1964.

Herd, D. G., T. L. Youd, H. Meyer, J. L. Arango, C. W. J. Person, and C. Mendoza, The great Tumaco, Colombia, earthquake of 12 December 1979, *Science, 211*, 441–445, 1981.

Isacks, B., and P. Molnar, Distribution of stresses in the descending lithosphere from a global survey of focal mechanism solutions of mantle earthquakes, *Rev. Geophys. Space Phys., 9*, 103–174, 1971.

Jordan, T. H., A procedure for estimating lateral variations from low-frequency eigenspectra data, *Geophys. J. R. Astron. Soc., 52*, 441–455, 1978.

Kanamori, H., Seismological evidence for lithospheric normal faulting – The Sanriku earthquake of 1933, *Phys. Earth Planet. Inter.*, *4*, 289–300, 1971.

Kanamori, H., and J. Cipar, Focal process of the great Chilean earthquake May 22, 1960, *Phys. Earth Planet. Inter.*, *9*, 128–136, 1974.

Kanamori, H., and J. W. Given, Use of long-period surface waves for rapid determination of earthquake-source parameters, *Phys. Earth Planet. Inter.*, *27*, 8–31, 1981.

Kanamori, H., and K. C. McNally, Variable rupture mode of the subduction zone along the Ecuador-Colombia Coast, *Bull. Seismol. Soc. Am.*, *72*, 1241-1253, 1982.

Kanamori, H., and G. S. Stewart, Mode of the strain release along the Gibbs Fracture Zone, Mid-Atlantic Ridge, *Phys. Earth Planet. Inter.*, *11*, 312–332, 1976.

Katsumata, M., and L. R. Sykes, Seismicity and tectonics of the western Pacific: Izu-Mariana-Caroline and Ryukyu-Taiwan regions, *J. Geophys. Res.*, *74*, 5923–5948, 1969.

Leeds, A. R., Lithospheric thickness in the Western Pacific, *Phys. Earth Planet. Inter.*, *11*, 61–64, 1975.

Masters, G., and F. Gilbert, Attenuation in the earth at low frequency, *Philos. Trans. R. Soc. London, Ser. A*, 308, 479–522, 1983.

Meyer, R. P., W. D. Mooney, A. L. Hales, C. E. Helsely, G. P. Woollard, D. M. Hussong, L. W. Kroenke, and J. E. Ramirez, Project Narino III: Refraction observation across a leading edge, Malpelo Island to the Colombian Cordillera Occidental, in *The Geophysics of the Pacific Ocean Basin and Its Margin, Geophys. Monogr. Ser.*, vol. 19, edited by G.H. Sutton et al., pp. 105–132, AGU, Wasington, D.C.,1976.

Mitronovas, W., B. Isacks, and L. Seeber, Earthquake locations and seismic wave propagation in the upper 250 km of the Tonga Island arc, *Bull. Seismol. Soc. Am.*, *59*, 1115–1135, 1969.

Müller, G., K. P. Bonjer, H. Stöckl, and D. Enescu, The Romanian earthquake of March 4, 1977, I, Rupture process inferred from fault-plane solution and multiple event analysis, *J. Geophys.*, *44*, 203–218, 1978.

Niazi, M., and H. Kanamori, Source parameters of the 1978 Tabas and 1979 Qainat, Iran, earthquakes from long-period surface waves, *Bull. Seismol. Soc. Am.*, *71*, 1201–1213, 1981.

Oike, K., On the nature of the occurrence of intermediate and deep earthquakes. 3. Focal mechanisms of multiplets, *Bull. Disaster Prev. Res. Inst., Kyoto Univ.*, *21* (part 2), 153–178, 1971.

Olson, A. H., Forward simulation and linear inversion of earthquake ground motions, Ph.D. dissertation, Univ. of Calif., San Diego, La Jolla, 1982.

Patton, P., and K. Aki, Bias in the estimate of seismic moment tensor by the linear inversion method, *Geophys. J. R. Astron. Soc.*, *59*, 479–495, 1979.

Sacks, I. S., S. Suyehiro, A. T. Linde, and S. A. Snoke, Slow earthquakes and stress redistribution, *Nature*, *275*, 599–602, 1978.

Sacks, I. S., A. T. Linde, J. A. Snoke, and S. Suyehiro, A slow earthquake sequence following the Izo-Oshima earthquake of 1978, in *Earthquake Prediction: An International Review, Maurice Ewing Ser.*, vol. 4, edited by D.W. Simpson and P. G. Richards, pp. 617–628, AGU, Washington, D.C., 1981.

Sasatani, T., Mechanism of mantle earthquakes near the junction of the Kurile and Northern Honshu arcs, *J. Phys. Earth*, *24*, 341–354, 1976.

Sasatani, T., Source parameters and rupture mechanism of deep-focus earthquakes, *J. Fac. Sci. Hokkaido Univ., Ser. 7*, *6*, 301–384, 1980.

Seno, T., K. Shimazaki, P. Somerville, K. Sudo, and T. Eguchi, Rupture process of the Miyagi-Oki, Japan earthquake of June 12, 1978, *Phys. Earth. Planet. Inter.*, *23*, 39–61, 1980.

Silver, P. G., and T. H. Jordan, Optimal estimation of scalar seismic moment, *Geophys. J. R. Astron. Soc.*, *70*, 755–787, 1982.

Stauder, W., and L. Mualchin, Fault motion in the larger earthquakes of the Kurile-Kamchatka Arc and of the Kurile-Hokkaido corner, *J. Geophys. Res.*, *81*, 297–308, 1976.

Stewart, G. S., E. P. Chael, and K. C. McNally, The November 29, 1978 Oaxaca, Mexico, earthquake—A large simple event, *J. Geophys. Res.*, *86*, 5053–5060, 1981.

Strelitz, R. A., The September 5, 1970 Sea of Okhotsk earthquake: A multiple event with evidence of triggering, *Geophys. Res. Lett.*, *2*, 124–127, 1975.

Talandier, J., and E. A. Okal, Human perception of *T* waves: The June 22, 1977 Tonga earthquake felt on Tahiti, *Bull. Seismol. Soc. Am.*, *69*, 147581486, 1979.

Uyeda, S., and H. Kanamori, Back arc openning and the mode of subduction, *J. Geophys. Res.*, *84*, 1049–1061, 1979.

Veith, K. F., The relationship of island arc seismicity and plate tectonics, Ph.D. dissertation, South. Methodist Univ., Dallas, Tex., 1974.

Wyss, M., and P. Molnar, Source parameters of intermediate and deep focus earthquakes in the Tonga Arc, *Phys. Earth Planet. Inter.*, *6*, 279–292, 1972.

Yoshii, T., Regionality of group velocities of Rayleigh waves in the Pacific and thickening of the plate, *Earth Planet. Sci. Lett.*, *25*, 305–312, 1975.

(Received July 23, 1982;
revised December 8, 1982;
accepted December 17, 1982.)

GEOPHYSICAL RESEARCH LETTERS, VOL. 13, NO. 6, PAGES 609-612, JUNE 1986

MOMENT-TENSOR SPECTRA OF THE 19 SEPT 85 AND 21 SEPT 85 MICHOACAN, MEXICO, EARTHQUAKES

Mark A. Riedesel

Institute for Geophysics, University of Texas, Austin, TX 78751

Thomas H. Jordan and Anne F. Sheehan

Department of Earth, Atmospheric and Planetary Sciences, MIT, Cambridge, MA 02139

Paul G. Silver

Department of Terrestrial Magnetism, Carnegie Institution, Washington, D.C. 20015

Abstract. IDA records of the 19 Sept 85 Michoacan earthquake and its large aftershock of 21 Sept 85 have been used to estimate source-mechanism spectra $\hat{\mathbf{M}}(\omega)$ and total-moment spectra $M_T(\omega)$ in 1-mHz bands over the frequency interval 1-11 mHz. Source mechanisms, obtained by the phase-equalization method of Riedesel and Jordan, show no significant frequency dependence and no significant non-double-couple components. The best average double-couple solution has a strike, dip and rake of 289° ± 4°, 19° ± 15° and 76° ± 5° for the main event, and 293° ± 3°, 24° ± 12° and 73° ± 4° for the aftershock. Total-moment spectra, obtained by the power-spectral method of Silver and Jordan, are parametrized by a total integrated moment M_T^0 and a characteristic time τ_c. For the main event, we obtain M_T^0 = (10.7 ± 2.0) × 10^{20} N-m and τ_c = 49 ± 7 s; the corresponding parameters for the aftershock are M_T^0 = (2.6 ± 0.6) × 10^{20} N-m and τ_c = 30 ± 11 s. Both events are relatively slow; in particular, the aftershock has a larger characteristic time than either the fast-rupturing 29 Nov 78 Oaxaca or the 14 Mar 79 Petalan earthquakes, although the static moments are about the same. Our results support the model of the main shock as a multiple-rupture event with moment release occuring as long as 100 s after the initial break.

Introduction

The Michoacan earthquake of 19 Sept 1985 and its large aftershock of 21 Sept 1985 were well recorded on the International Deployment of Accelerometers (IDA) network of long-period gravimeters. We have employed the data from 13 IDA stations to study the low-frequency source properties of these events. The spectrum of a moment-rate tensor $\dot{\mathbf{M}}(\omega)$ can be factored into a total scalar moment $M_T(\omega)$ and a source mechanism $\hat{\mathbf{M}}(\omega)$, a second-rank tensor with unit euclidean norm [Silver and Jordan, 1982]:

$$\mathbf{M}(\omega) = \sqrt{2}\, M_T(\omega)\, \hat{\mathbf{M}}(\omega) \qquad (1)$$

We have estimated the source-mechanism spectrum $\hat{\mathbf{M}}(\omega)$ by the moment-tensor inversion method of Riedesel and Jordan [1985] and the total-moment spectrum $M_T(\omega)$ by the technique of Silver and Jordan [1982, 1983].

Twelve stations were employed for each event, with eleven common to both. The data were edited to eliminate nonlinearities in the initial body waves, the R_1 surface-wave packets, and, in some cases, R_2 surface waves. All stations recorded R_3 and later wave groups without any apparent nonlinear distortion. Five hours of record following the first good time point were used in the analysis. Transfer functions relating the moment-rate tensor to acceleration were generated from model 1066A [Gilbert and Dziewonski, 1975] assuming the centroid latitudes, longitudes and depths reported by Harvard [G. Ekström, personal communication, 1986]: 17.97°N, 102.07°W, 22km for the main event and 17.61°N, 101.48°W, 22 km for the aftershock. For these large events, our analysis is not sensitive to the exact location used, and the NEIS parameters yield virtually identical results.

Paper number 6L6133.
0094-8276/86/006L-6133$03.00

Source-Mechanism Spectra

The data functionals employed by the moment-tensor inversion method of Riedesel and Jordan [1985] are integrals of the complex acceleration spectra over narrow frequency bands (0.1 mHz in this study) centered on the fundamental spheroidal modes. The frequency-domain averaging reduces the sensitivity of the estimates to attenuation and splitting [Gilbert, 1973; Jordan, 1978]. The algorithm involves a nonlinear phase-equalization procedure to compensate for centroid time shifts, the effects of unmodeled earth structure, and station timing errors. In this study, estimates $\hat{\mathbf{M}}(\omega_n)$ are obtained over the frequency interval 1-11 mHz by inverting the integrals in discrete 1-mHz bands centered on the frequencies $\omega_n = (n + 1/2)$ mHz; $n = 1, 2, \ldots 10$. This interval contains 101 fundamental modes, about ten per millihertz, so that for the Michoacan earthquakes, approximately 120 complex numbers are used to derive the moment-rate tensor in each 1-mHz band. Riedesel [1985] has demonstrated that this procedure yields reliable narrow-band estimates of the source-mechanism spectrum to frequencies as high as 11 mHz and that the errors derived for the estimates adequately model the uncertainties induced by noise in the data, including signal-generated noise.

Good measures of estimation error are essential in testing for the frequency dependence of the source spectrum and the existence of non-double-couple components, but these have generally not been available in the standard procedures for moment-tensor inversion [Dziewonski et al., 1981; Sipkin, 1982]. Part of the problem is simply the difficulty in manipulating and displaying the autocovariance of a second-rank tensor. Riedesel and Jordan [1982] have devised a graph of the source-mechanism tensor $\hat{\mathbf{M}}$ which facilitates the visualization of its uncertainties and their use in hypothesis testing, and we employ this diagram here. The graph is based on the eigenvector expansion $\hat{\mathbf{M}} = \sum \lambda_i \hat{\mathbf{e}}_i \hat{\mathbf{e}}_i$. Assuming the eigenvectors are ordered such that $\lambda_1 \geq \lambda_2 \geq \lambda_3$, we construct the unit vector $\hat{\lambda} = \sum \lambda_i \hat{\mathbf{e}}_i$. A plot of $\hat{\lambda}$, $\hat{\mathbf{e}}_1$, $\hat{\mathbf{e}}_2$ and $\hat{\mathbf{e}}_3$ on the unit focal sphere is isomorphic to $\hat{\mathbf{M}}$, and thus completely characterizes the source mechanism. On such a plot the three vectors $\hat{\mathbf{d}} = (\hat{\mathbf{e}}_1 - \hat{\mathbf{e}}_3)/\sqrt{2}$, $\hat{\mathbf{l}} = (\hat{\mathbf{e}}_1 - 1/2\,\hat{\mathbf{e}}_2 - 1/2\,\hat{\mathbf{e}}_3)/\sqrt{3/2}$, and $\hat{\mathbf{i}} = (\hat{\mathbf{e}}_1 + \hat{\mathbf{e}}_2 + \hat{\mathbf{e}}_3)/\sqrt{3}$ represent the values of $\hat{\lambda}$ for a pure double-couple, a pure compensated linear vector dipole, and a pure dilatation, respectively. The great

circle containing $\hat{\mathbf{d}}$ and $\hat{\mathbf{l}}$ is the locus of all purely deviatoric mechanisms in the eigenvector reference frame. The fact that the eigenvalues λ_i are stationary with respect to small perturbations in the eigenvectors $\hat{\mathbf{e}}_i$ ensures that, to first order, the uncertainties in $\hat{\boldsymbol{\lambda}}$ are uncorrelated with the errors in the eigenvectors and can thus be expressed in the reference frame $(\hat{\mathbf{d}}, \hat{\mathbf{l}}, \hat{\mathbf{i}})$. These uncertainties are plotted as a 95%-confidence ellipse about $\hat{\boldsymbol{\lambda}}$ on the focal sphere, which allows various hypotheses regarding the source mechanism to be tested by inspection. For example, the hypothesis that $\hat{\mathbf{M}}$ is a double-couple ($\hat{\boldsymbol{\lambda}} = \hat{\mathbf{d}}$) is rejected if $\hat{\mathbf{d}}$ falls outside the $\hat{\boldsymbol{\lambda}}$ confidence ellipse. The marginal uncertainties in the principal axes can be similarly calculated using first-order perturbation theory, and they are also plotted as 95%-confidence ellipses. Therefore, on a single focal sphere we display the source mechanism $\mathbf{M}$, including its non-double-couple components, and a complete representation of its uncertainties, except for the covariances between the principal axes.

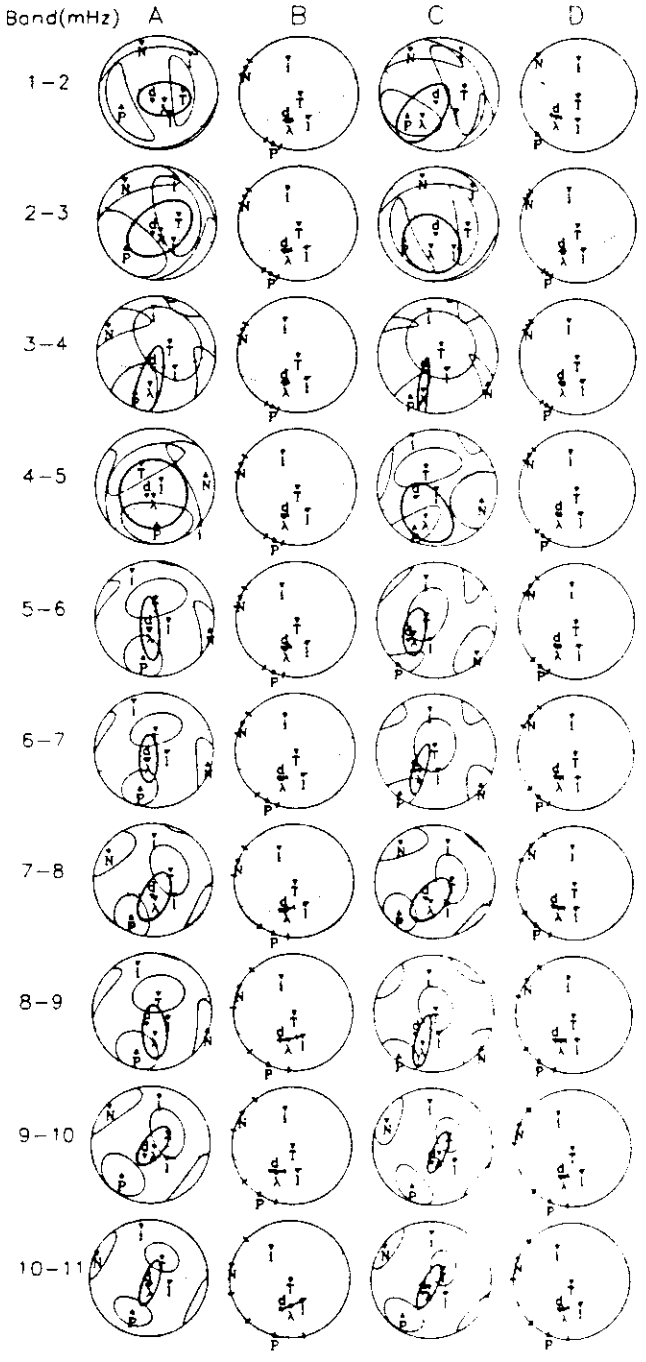

The source-mechanism spectra for the Michoacan earthquakes are shown in Figure 1. Two sets of mechanisms were calculated for each event. In the first (spectra *A* and *C*), all elements of $\mathbf{M}$ were retained in the solution. The error ellipses for the $\hat{\boldsymbol{\lambda}}$ vector and the principal axes are large at low frequencies, reflecting the poor resolution of the long-period data in determining $M_{r\theta}$ and $M_{r\phi}$ for shallow-focus sources [Kanamori and Given, 1981, 1982] and $tr\,\mathbf{M}$ in general [Mendiguren and Aki, 1978]. To examine the constraints on the other components of the source mechanism, we computed a second set of spectra, columns *B* and *D* of Figure 1, where the trace of $\mathbf{M}$ and its $r\theta$ and $r\phi$ components were treated as "nuisance parameters" and projection operators were applied to annihilate the dependence of the data equations on these components [Riedesel, 1985]. The error-normalized equations are solved by a generalized inverse, so that the projected components in spectra *B* and *D* are set equal to zero; in particular, the axis corresponding to the maximum eigenvalue is vertical, and the $\hat{\boldsymbol{\lambda}}$ vector is constrained to lie on the deviatoric great circle. It should be emphasized that this solution is not the same as obtained by the standard procedure of fixing $tr\,\mathbf{M}$, $M_{r\theta}$ and $M_{r\phi}$ to be zero [e.g., Kanamori and Given, 1982], since the estimation errors on the unprojected elements of $\mathbf{M}$ calculated by the Riedesel-Jordan method are not conditional on the values of the nuisance parameters. In the projected spectra, the estimation errors are generally largest at high frequency and obtain a minimum in the 3–4-mHz band, where the signal-to-noise ratio of the normal-mode data is highest.

None of the spectra in Figure 1 show any significant frequency dependence or any significant non-double-couple behavior. Among the twenty unprojected mechanisms in columns *A* and *C* of Figure 1, for example, the 95% confidence ellipse of $\hat{\boldsymbol{\lambda}}$ contains $\hat{\mathbf{d}}$ in all cases but one, as would be expected from random errors. The mechanisms obtained by averaging the variance-weighted, unprojected spectra are listed in Table 1 and displayed in Figure 2. Neither has a significant non-double-couple component. The strike and dip of the best-fitting fault plane are somewhat greater for the aftershock than the main event (Table 1), but

Fig. 1. Source-mechanism spectra $\hat{\mathbf{M}}(\omega)$ for the Michoacan earthquake of 19 Sept 85 (columns *A* and *B*) and its large aftershock of 21 Sept 85 (columns *C* and *D*) over the frequency interval 1-11 mHz. Each circle is a focal-sphere plot of the normalized moment tensor $\hat{\mathbf{M}}(\omega)$ in a 1-mHz band derived from 12 IDA records by the normal-mode method of Riedesel and Jordan [1985]. Columns *A* and *C* are unprojected mechanisms for the main event and aftershock, respectively, whereas columns *B* and *D* are projected mechanisms for which $tr\,\hat{\mathbf{M}}$, $\mathbf{M}_{r\theta}$, and $\mathbf{M}_{r\phi}$ have been annihilated by the orthogonalization procedure described in Riedesel [1985]. Each $\hat{\mathbf{M}}$ is represented by the source-mechanism diagram introduced by Riedesel and Jordan [1982]. The three principal axes $\hat{\mathbf{e}}_1$, $\hat{\mathbf{e}}_2$ and $\hat{\mathbf{e}}_3$, corresponding to eigenvalues $\lambda_1 \geq \lambda_2 \geq \lambda_3$, are plotted as T, N and P on a stereographic projection of the lower focal hemisphere with their marginal 95% confidence ellipses (thin lines). The mechanism is characterized by the unit vector $\hat{\boldsymbol{\lambda}} = \sum \lambda_i \hat{\mathbf{e}}_i$ and its 95% confidence ellipse (thick line), which can be compared with the canonical unit vectors $\hat{\mathbf{d}}$, $\hat{\mathbf{l}}$, and $\hat{\mathbf{i}}$, representing a pure double-couple, a pure compensated linear vector dipole, and a pure dilatation, respectively. The dashed line shows the locus of all deviatoric mechanisms. Vectors are plotted as ∇ if they are on the lower focal hemisphere and as a Δ if they are projected from the upper hemisphere.

TABLE 1. Source parameters for the Michoacan earthquakes.

Source Parameters	19 Sept 85	21 Sept 85
Mechanism:		
$\hat{M}_{rr}$	.489 ± .114	.406 ± .107
$\hat{M}_{\theta\theta}$	−.288 ± .071	−.441 ± .053
$\hat{M}_{\phi\phi}$	−.059 ± .031	−.218 ± .027
$\hat{M}_{r\theta}$	.457 ± .062	.343 ± .049
$\hat{M}_{r\phi}$	−.331 ± .055	−.351 ± .040
$\hat{M}_{\theta\phi}$	.137 ± .035	.237 ± .024
Slip vector azimuth:	33° ± 6°	40° ± 5°
Best double couple:		
Strike	289° ± 4°	293° ± 3°
Dip	19° ± 15°	24° ± 12°
Rake	76° ± 5°	73° ± 4°
Total Moment Spectrum:		
M_T^0 (10^{20} N-m)	10.7 ± 2.0	2.6 ± 0.6
τ_c (s)	49 ± 7	30 ± 11

Source mechanism parameters correspond to the variance-weighted averages of Figure 2. Total scalar moments and characteristic times are obtained from fits of equation (2) to the total-moment spectra of Figure 3.

given their uncertainties, the two mechanisms are not significantly different at the 95% confidence level (chi-square of 5.9 against a critical value of 11.1). Although there is a trade-off between strike and rake of the best-fitting double couple, both mechanisms show a significant left-lateral strike-slip component, which is consistent with other thrust earthquakes along this section of the Middle America Trench [Chael and Stewart, 1982]. The slip-vector azimuth is N33°E ± 6° for the main event and N40°E ± 5° for the aftershock, which compares with N37°E ± 3° predicted by the RM2 plate-motion model [Minster and Jordan, 1978].

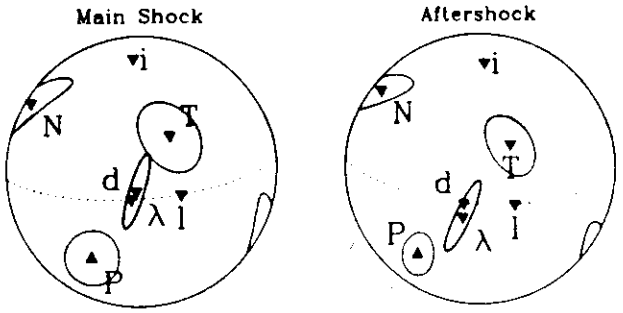

Fig. 2. Source mechanisms for the Michoacan earthquake of 19 Sept 85 (left) and its large aftershock of 21 Sept 85 (right) obtained by averaging the spectra A and C of Figure 1, weighted by their covariance matrices. Plotting conventions are the same as in Figure 1. At the 95% confidence level corresponding to the error ellipses, the mechanism vectors $\hat{\lambda}$ are not significantly different from the double-couple vectors $\hat{d}$, and the hypothesis that the two events have the same double-couple mechanism cannot be rejected. The source parameters for these average solutions are listed in Table 1.

Total-Moment Spectra

The size of an earthquake is measured by a total integrated moment $M_T^0 \equiv M_T(0)$, and its duration is measured by a characteristic time $\tau_c = 2(\mu^{(2)}/\mu^{(0)})^{1/2}$, where $\mu^{(n)}$ is the n^{th} central moment of the source time function [Silver and Jordan, 1983]. Following Silver and Jordan [1983], we derive estimates of τ_c and M_T^0 by fitting total-moment observations with a spectrum of the form

$$M_T(\omega) = M_T^0 (1 + \omega^2 \tau_c^2/8)^{-1}. \quad (2)$$

To obtain unbiased estimates of the total-moment spectrum, we have applied the scalar-moment estimation algorithm of Silver and Jordan [1982, 1983]. Their algorithm employs frequency-averaged power and cross spectra from a set of seismograms to derive an optimal estimate of M_T conditional on a probability distribution assumed for $\hat{M}$.

For the Michoacan earthquakes, we constructed a gaussian approximation to the $\hat{M}$ distribution from the estimates and uncertainties given in Figure 2 according to equation (4.67) of Silver and Jordan [1982]. We specialized the total-moment estimation algorithm to power spectra, which were integrated over disjunct 1-mHz bands in the interval 1-11 mHz. The resulting total-moment spectra are plotted in Figure 3, and the parameters derived by fitting equation (2) to these spectra are listed in Table 1.

The static moment of the Michoacan main event is (10.7 ± 2.0) × 10^{20} N-m, consistent with the single-station CMT

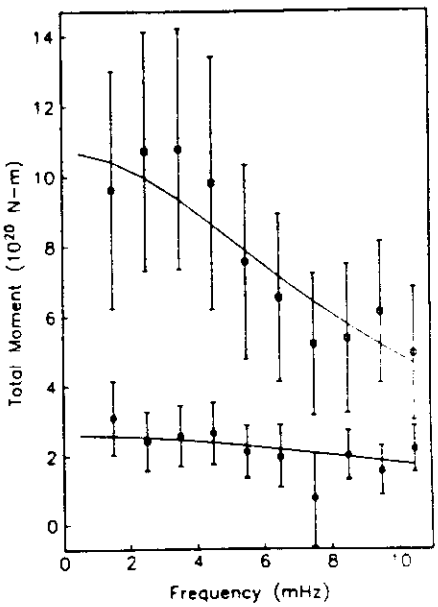

Fig. 3. Total-moment spectra over the frequency interval 1-11 mHz for the Michoacan earthquake of 19 Sept 85 (squares) and its large aftershock of 21 Sept 85 (circles). The spectral estimates and their one-sigma error bars were computed from 1-mHz averages of IDA power spectra using the method of Silver and Jordan [1982, 1983]. Estimation errors are correlated from band to band by uncertainties in the source mechanisms of Figure 2. Solid lines are theoretical spectra obtained by fitting equation (2) to the observations; the parameters are $M_T^0 = (10.7 \pm 2.0) \times 10^{20}$ N-m and $\tau_c = 49 \pm 7$ s for the main event, and $M_T^0 = (2.6 \pm 0.6) \times 10^{20}$ N-m and $\tau_c = 30 \pm 11$ s for the aftershock.

value of 13×10^{20} N-m obtained by Ekström et al. [1986]. The large correlated uncertainties in total-moment estimates of Figure 3 reflect their sensitivity to the nodal-plane orientation of the assumed mechanism. A dip of 19° is obtained by averaging $\hat{\mathbf{M}}$ over the entire 1-11 mHz band (Table 1), but this dip could be biased high by our inability to resolve $M_{r\theta}$ and $M_{r\phi}$ at low frequencies. Decreasing the dip to 10° would increase the moment to about 19×10^{20} N-m, in general agreement with the conclusions of Eissler et al. [1986]. M_T^0 for the aftershock is about a factor of four less than the main event, which is the average amplitude ratio observed on the IDA seismograms.

The characteristic time τ_c estimated by the Silver-Jordan method is 49 ± 7 s for the main event and 30 ± 11 s for the aftershock. We can compare these times with the difference Δt between the temporal centroid of the earthquake and its origin time measured by high-frequency P waves. Using the temporal centroids from our moment-tensor inversions and origin times from the NEIS, we obtain $\Delta t = 34 \pm 5$ s and 24 ± 5 s for the main shock and aftershock, respectively. Assuming the rate of moment release is constant over the duration of faulting (in which case, $2\Delta t$ is the "source process time" of Kanamori and Given [1981]), we can relate the centroid time shift to the characteristic time by the equation $\tau_c = 2\Delta t/\sqrt{3}$; this gives $\tau_c = 39 \pm 6$ s and 28 ± 6 s. Hence, two independent estimators of characteristic time, one based on spectral roll-off and one based on centroid time shift, yield similar results.

Although not statistically significant at the error levels quoted, the fact that our two estimators of τ_c differ by 10 s for the main event could be an indication that the moment release is not constant during the rupture process, but concentrated towards the origin time. The source time functions obtained by Ekström et al. [1986] and Houston and Kanamori [1986, Figure 4] show that the moment release for the main shock took place in a series of discrete pulses at intervals of about 25 s, with amplitudes diminishing in time. Houston and Kanamori's [1986, Figure 5] representative source time function is characterized by moment release up to 100 s after the initial break, although the uncertainties in their estimates are such that only the first 70 seconds are considered significant [H. Houston, personal communication, 1986]. The duration parameters calculated from the first 70 s of this time function are $\Delta t = 29$ s and $\tau_c = 37$ s, whereas the full 100 s yield $\Delta t = 33$ s and $\tau_c = 46$ s, in better agreement with our measurements. This comparison suggests the existence of some activity beyond 70 s after the origin time. Both the main event and the aftershock plot in the slow-earthquake field of Silver and Jordan [1983, Figure 20]. In particular, the aftershock apparently has a larger characteristic time than either the fast-rupturing 29 Nov 78 Oaxaca or the 14 Mar 79 Petalan earthquakes studied by Silver and Jordan [1983], although its static moment is about the same.

Acknowledgements. We thank Duncan Agnew for providing us with the IDA data in advance of the normal distribution date. Justin Revenaugh assisted in the generation of transfer functions. Guy Masters gave us programs to compute normal-mode eigenfunctions and to manipulate IDA data on Apollo computers. We thank the Caltech group for their preprints. This work was supported by DARPA under AFGL contract #F19628-85-K-0024.

References

Chael, E.P., and G.S Stewart, Recent large earthquakes along the Middle American Trench and their implications for the subduction process, *J. Geophys. Res.*, *87*, 329-338, 1982.

Dziewonski, A.M., T.A. Chou, and J.H. Woodhouse, Determination of earthquake source parameters from wave-form data for studies of global and regional seismicity, *J. Geophys. Res.*, *86*, 2825-2852, 1981.

Eissler, H., L. Astiz, and H. Kanamori, Tectonic setting and source parameters of the September 19, 1985 Michoacan, Mexico earthquake, *Geophys. Res. Lett.*, this issue.

Ekström, G., A.M. Dziewonski, and J. Steim, Single station CMT; application to the Michoacan, Mexico, earthquake of September 19, 1985, *Geophys. Res. Lett.*, *13*, 173-176, 1986.

Gilbert, F., Derivation of source parameters from low-frequency spectra, *Phil. Trans. R. Soc. Lond., Ser. A*, *274*, 369-371, 1973.

Gilbert, F., and A.M. Dziewonski, An application of normal mode theory to the retrieval of structural parameters and source mechanisms from seismic spectra. *Phil. Trans. R. Soc. Lond., Ser. A*, *278*, 187-269, 1975.

Houston, H., and H. Kanamori, Source characteristics of the 1985 Michoacan, Mexico earthquake at short periods, *Geophys. Res. Lett.*, this issue.

Jordan, T.H., A procedure for estimating lateral variations from low-frequency eigenspectra data, *Geophys. J. R. Astr. Soc.*, *52*, 441-455, 1978.

Kanamori, H., and J.W. Given, Use of long-period surface waves for fast determination of earthquake source parameters, *Phys. Earth Planet. Inter.*, *27*, 8-31, 1981.

Kanamori, H., and J.W. Given, Use of long-period surface waves for fast determination of earthquake source parameters 2. Preliminary determination of source mechanisms of large earthquakes ($M_S > 6.5$) in 1980, *Phys. Earth Planet. Inter.*, *30*, 260-268, 1982.

Mendiguren, J.A., and K. Aki, Source mechanism of the deep Colombian earthquake of July 31, 1970 from the free oscillation data, *Geophys. J. R. Astr. Soc.*, *55*, 539-556, 1978.

Minster, J.B., and T.H. Jordan, Present-day plate motions, *J. Geophys. Res.*, *83*, 5331-5354, 1978.

Riedesel, M.A., and T.H. Jordan, Display and assessment of source mechanisms with non-double-couple components, *EOS*, *63*, 1027-1028, 1982.

Riedesel, M.A., Seismic moment tensor recovery at low frequencies, Ph.D. dissertation, Univ. of Calif., San Diego, La Jolla, 1985.

Riedesel, M.A., and T.H. Jordan, Multiple-band estimates of moment tensors at low frequencies and their uncertainties, *EOS*, *66*, 301, 1985.

Silver, P.G., and T.H. Jordan, Optimal estimation of scalar seismic moment, *Geophys. J. R. Astr. Soc.*, *70*, 755-787, 1982.

Silver, P.G., and T.H. Jordan, Total-moment spectra of fourteen large earthquakes, *J. Geophys. Res.*, *88*, 3273-3293, 1983.

Sipkin, S.A., Estimation of earthquake source parameters by the inversion of waveform data: synthetic waveforms, *Phys. Earth Planet. Inter.*, *30*, 242-259, 1982.

(Received March 28, 1986;
accepted April 22, 1986.)

JOURNAL OF GEOPHYSICAL RESEARCH, VOL. 95, NO. B3, PAGES 2485–2510, MARCH 10, 1990

Searching for Slow and Silent Earthquakes Using Free Oscillations

GREGORY C. BEROZA AND THOMAS H. JORDAN

Department of Earth, Atmospheric and Planetary Sciences
Massachusetts Institute of Technology, Cambridge

Our knowledge of Earth structure can be used to distinguish far-field seismic signals from near-field noise. In particular, earthquakes excite ground motion at the eigenfrequencies of the Earth's normal modes. By observing the spectral levels in small bands centered on the known frequencies of the normal mode resonance peaks and comparing them to the spectral levels of ambient noise, it is possible to detect earthquakes at low frequencies without knowing anything about them at high frequencies. We have used this fact to develop an earthquake detection algorithm that compares the signal level in the mode bands, as measured by the modulus of zeroth-order moment of the Fourier spectrum, with that in the noise bands using an F test. The excitation of each mode over a global network of stations and of all the modes over the network is evaluated from a summed-score statistic using a binomial test and a Markov test, respectively, which are robust with respect to deviations from the Gaussian noise model. We apply the technique to the Earth's fundamental spheroidal modes ${}_0S_8$-${}_0S_{43}$ as recorded by the IDA network for the 2-year interval 1978-1979. We calculate the level of excitation at 3-hour intervals using a time domain integration technique designed to optimize the signal-to-noise ratio for each mode. The algorithm detects 50% of all teleseismic earthquakes having seismic moments $M_0 \geq 1 \times 10^{18}$ N m ($M_w \geq 6.0$), and it detects all events having $M_0 \geq 3 \times 10^{18}$ N m ($M_w \geq 6.3$). Slow earthquakes, i.e., those having anomalously large characteristic durations, are observed to be enriched in low-frequency mode excitation relative to other events of comparable magnitude. Using this criterion, we have found a number of slow earthquakes that had not been previously identified as anomalous. Most of these newly identified slow earthquakes occurred on oceanic transform faults. In addition to the cataloged normal and slow earthquakes, we observe 27 episodes of substantial mode excitation that are reasonably well isolated from significant earthquakes. Such anomalies may represent "silent earthquakes," events with propagation velocities sufficiently low that they do not generate globally detectable wave trains on high-frequency seismometers.

INTRODUCTION

Although motion in the Earth's interior presumably is accomplished by quasi-steady creep, the nonelastic deformation of the lithosphere tends to occur as discrete events localized about some space-time centroid $(\mathbf{r}, t)$. The finite size of a deformation event can be measured by a characteristic length L_c and characteristic duration τ_c, defined in terms of the second central moments of the stress-glut-rate tensor [*Backus and Mulcahy*, 1976*a*,*b*; *Backus*, 1977*a*,*b*; *Silver and Jordan*, 1983, equations (A13)-(A14)]. The ratio of these dimensions defines a characteristic rupture velocity,

$$v_c = L_c/\tau_c \tag{1}$$

The most obvious deformation events are ordinary earthquakes: elastodynamic cracks propagating close to the shear-wave velocity (kilometers per second). However, deformation events occur over a broad spectrum of temporal and spatial scales, some having characteristic velocities orders of magnitude less than fast elastodynamic ruptures (Figure 1).

In addition to ordinary earthquakes, seismologists distinguish two other types of seismic events: slow earthquakes and silent earthquakes. Like an ordinary earthquake, a slow earthquake includes one or more episodes of high-speed rupture propagation, so that it produces an ordinary train of high-frequency body waves; however, its overall duration is unusually long relative to ordinary events of comparable total moment, and its level of low-frequency excitation is anomalously high [*Benioff and Press*, 1958; *Kanamori*, 1972; *Kanamori and Stewart*, 1979]. Documented examples include the 1946 Aleutian Islands earthquake ($v_c \approx$ 200 m/s), which generated a strong tsunami [*Kanamori*, 1972; *Abe*, 1973]; several events on the Gibbs fracture zone [*Kanamori and Stewart*, 1976]; the June 6, 1960, Chilean transform event, which ruptured for about an hour as a series of earthquakes of relatively small seismic moment (~5 × 10^{20} N m) [*Kanamori and Stewart*, 1979]; the Izu-Oshima earthquake of January 14, 1978 [*Sacks et al.*, 1981]; several oceanic transform fault earthquakes [*Okal and Stewart*, 1982; *Stewart and Okal*, 1983]; and the Banda Sea event of February 21, 1978 [*Silver and Jordan*, 1983].

Silent earthquake is the oxymoron used to designate a slow event with no episodes of high-velocity rupture propagation, so that it does not generate teleseismically detectable high-frequency radiation [*Dziewonski and Gilbert*, 1974; *Gilbert and Dziewonski*, 1975; *Yamashita*, 1980; *Bonafede et al.*, 1983]; hence it is not identified during the routine construction of earthquake catalogs. The documented examples of silent earthquakes include creep episodes along the San Andreas fault in California [*Scholz et al.*, 1969; *King et al.*, 1973], low-frequency signals observed at the Trieste tide station preceding the 1976 Friuli earthquake [*Bonafede et al.*, 1983], and deformation events detected by strain meters in the near field in Japan [*Sacks et al.*, 1978; *Linde et al.*, 1988].

Figure 1 summarizes the distribution of deformation events on a plot of characteristic length versus characteristic time. We arbitrarily choose v_c = 1 km/s to distinguish slow earthquakes from normal events. Slow earthquakes identified from near-field data exhibit apparent rupture velocities as low as 20 m/s. The characteristic velocities of silent earthquakes determined from near-field observations range from ~10 m/s for the Friuli precursors [*Bonafede et al.*, 1983] to ~10 mm/s for San Andreas creep events [*Scholz et al.*, 1969; *King et al.*, 1973]. Deformation

Paper number 90JB00035.
0148-0227/90/90JB-00035505.00

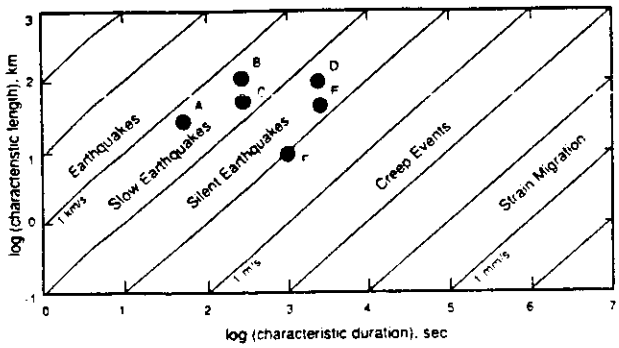

Fig. 1. A plot of the characteristic time versus characteristic length for lithospheric deformation events. "Ordinary earthquakes" occur at characteristic rupture velocities that are a substantial fraction of the shear wave velocity. Creep events on the San Andreas fault occur at ~ 1 m/s and strain migration events occur at ~ 1 mm/s. Between main sequence earthquakes and creep events are some documented examples of slow and silent earthquakes. They are A, the February 21, 1978, Banda Sea earthquake [*Silver and Jordan*, 1983]; B, the 1896 Sanriku earthquake [*Kanamori*, 1972]; C, the 1946 Aleutian Islands earthquake [*Kanamori*, 1972; *Abe*, 1973]; D, the June 6, 1960, Chilean earthquake [*Kanamori and Stewart*, 1979]; E, the January 14, 1978, Izu-Oshima earthquake [*Sacks et al.*, 1981]; and F, precursors to the 1976 Friuli earthquake [*Bonafede et al.*, 1983].

events with lower characteristic velocities, as low as 1 mm/s, are estimated to be typical of strain migration [*Kasahara*, 1973; *Rundle*, 1978]. Apparently, deformation of the lithosphere is episodic and complex, with characteristic velocities varying by 6 orders of magnitude or more. At present, the constitutive equations that govern slow deformation events are not well understood, and the spatial and temporal relationships between slow deformation and fast seismic ruptures are obscure.

To observe phenomena at the very low end of the velocity spectrum requires near-field strainmeter and geodetic data, but slow earthquakes, and perhaps some silent earthquakes, can be studied using low-frequency seismic waves recorded by global networks of seismometers. The International Deployment of Accelerometers (IDA) network, which has been producing a continuous stream of high-quality digital data for over 10 years [*Agnew et al.*, 1986], is well-suited for this purpose. Although data from IDA and other low-frequency networks have been used to investigate specific events, including slow earthquakes [*Kanamori and Given*, 1981; *Okal and Stewart*, 1981; *Silver and Jordan*, 1982, 1983; *Dziewonski and Woodhouse*, 1983], there have thus far been no systematic attempts to catalog slow earthquakes or to observe silent earthquakes using the excitation of the Earth's normal modes at frequencies less than 10 mHz.

Among the available compilations of source properties derived from long-period waveform data, the Harvard Centroid Moment Tensor (CMT) catalog [*Dziewonski et al.*, 1981, 1987*a*,*b*; *Dziewonski and Woodhouse*, 1983] is the most complete. The CMT catalog includes source parameters measured in a band centered at about 15 mHz for most events well recorded by the Global Digital Seismic Network (GDSN). Among the source parameters routinely compiled by the Harvard group are the centroid time shift Δt and the seismic moment M_0. Δt is defined to be the difference between the temporal centroid of seismic moment release and the high-frequency origin time; it is a measure of earthquake duration, whereas M_0 is a measure of earthquake size. Slow earthquakes are expected to have a larger Δt than other earthquakes of comparable M_0, which provides a method for identifying slow earthquakes in the CMT catalog [*Dziewonski and Woodhouse*, 1983]. However, this interpretation assumes that the origin time of low-frequency radiation coincides with the origin time measured from high-frequency radiation. *Dziewonski and Gilbert* [1974] and *Jordan et al.* [1988; manuscript in preparation, 1990] have presented evidence that slow deformation precedes the high-frequency origin time for some earthquakes. In such a situation the centroid time shift Δt can be arbitrarily less than $\tau_c/2$, the true half duration of moment release [*Jordan et al.*, 1988], which biases the method against the detection of slow events.

In this paper, we systematize the identification of slow and silent earthquakes by constructing a detector sensitive to low-frequency (1-5 mHz) free oscillations. We apply this detector to seismograms recorded by the IDA network for the 2-year period 1978-1979. We use it to construct a catalog of mode-excitation events and attempt to associate these excitation events with known earthquakes. Slow earthquakes are identified as those having anomalously strong mode excitations relative to their CMT magnitudes; we confirm their anomalously long durations by computing τ_c using the moment-spectrum technique of *Silver and Jordan* [1983]. We have been unable to associate some low-frequency excitation events with significant earthquakes ($M \geq 5.4$) in the standard high-frequency catalogs, and we speculate that these may be slow events that do not initiate fast seismic ruptures of significant size; they may be silent, or at least quiet, earthquakes.

THE DETECTION ALGORITHM

Our knowledge of Earth structure can be used to distinguish far-field seismic signals from near-field noise. At low frequencies, a teleseismically recorded earthquake will excite ground motion with energy concentrated in narrow bands centered on the eigenfrequencies of the Earth's normal modes, whereas local ground noise will be more uniformly distributed in frequency. We use these properties to develop an algorithm for detecting any event that excites the fundamental spheroidal modes above the background noise level. Specifically, we test the null hypothesis that the energy levels in the fundamental spheroidal mode bands observed on a global network are due to random noise against the alternative hypothesis that they are due to a seismic event. We begin by outlining this hypothesis-testing algorithm in its general form, deferring the details of its application to IDA network data to the following section.

We consider a particular station in this network having a vertical-component time series $u(t)$ whose complex Fourier transform over a time interval $[t, t+T]$ is $u(\omega)$. As a measure of the spectral level over a bandwidth $2w_l$ centered at frequency ω_l, we employ $|\mu_0(\omega_l)|^2$, the squared modulus of the zeroth-order moment of the Fourier spectrum. The zeroth-order moment is a complex number defined by the integral

$$\mu_0(\omega_l) = \int_{\omega_l - w_l}^{\omega_l + w_l} u(\omega)\, d\omega \qquad (2)$$

As an observable it has several desirable qualities. Spectral averaging enhances coherent signals relative to random noise. In the case of an isolated normal-mode multiplet with an eigenfrequency ω_l and a damping parameter $\omega_l/2Q_l$ whose magnitude is not much larger than w_l, $\mu_0(\omega_l)$ is proportional to the excitation amplitude of

the mode but is relatively insensitive to the distortions of the peak shape caused by attenuation [*Gilbert*, 1973] and lateral heterogeneities [*Jordan*, 1978]. Moreover, (2) can be efficiently computed as a single time-domain integral (see equation-8).

Mode detection by a single station

Suppose the time series $u(t)$ consists entirely of stationary Gaussian noise with zero mean and a power spectrum $v^2(\omega)$ which varies slowly with frequency. Then the spectral level in the lth mode band, centered at frequency ω_l, will have an expected value approximately equal to the average of the levels in two noise bands centered at nearby frequencies $\omega_l^- < \omega_l$ and $\omega_l^+ > \omega_l$. We choose the center frequencies ω_l^- and ω_l^+ to be on either side of the resonance peak of interest and compute $\mu_0(\omega_l^{\pm})$ by integrating the spectrum over the same half width w_l as in (2). When no modes are excited, the random variable

$$\gamma^2 = \frac{|\mu_0(\omega_l)|^2}{\frac{1}{2}\left(|\mu_0(\omega_l^-)|^2 + |\mu_0(\omega_l^+)|^2\right)} \quad (3)$$

will be governed by an F-distribution with 2 degrees of freedom in the numerator and 4 in the denominator. We define γ_α^2 to be the critical value for the $100\alpha\%$ upper tail of $F(2,4)$ and reject the null hypothesis $H_0 \equiv$ {the spectral level in the mode band $\omega_l \pm w_l$ is due only to random noise} in favor of the alternative $H_1 \equiv$ {the mode has been excited by a seismic event} when

$$\gamma^2 > \gamma_\alpha^2 \quad (4)$$

If our assumptions about the noise statistics are justified, then the probability of making a Type-I error (false positive) is α, and we say that H_0 is tested against H_1 at the $100(1-\alpha)\%$ confidence level. Standard tables yield $\gamma_\alpha^2 =$ 0.83, 2.00, 19.25 for the 50%, 75%, 95% confidence levels, respectively.

The probability of making a Type-I error is a parameter we are free to choose. By making simple assumptions about the behavior of γ^2 in the presence of the signal, we can also calculate (see Appendix A) the probability β of failing to detect an excitation when one has occurred; this is called a Type-II error, or false negative. In the jargon of statistics [e.g., *Wolf*, 1962], the power of a statistical test is $1-\beta$, the probability of correctly rejecting H_0 when H_1 is true.

As displayed in Figure 2, β depends strongly on the signal-to-noise ratio (snr) R, which is defined in Appendix A. For a specified value of α, we define the detectability threshold R_d to be the value of the snr at which $\beta = 0.5$; that is, R_d is the excitation level when half of the anomalous events are detected and half are not. Figure 2 shows that at the 99.9% confidence level ($\alpha = 0.001$), the detectability threshold is $R_d = 8.5$ for a single mode recorded at a single station. Reducing the confidence level to 90% decreases this threshold to 2.0.

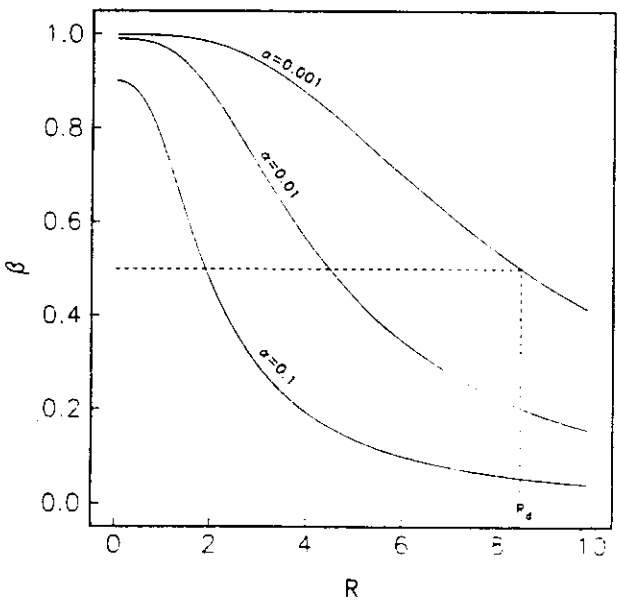

Fig. 2. The level of Type-II errors, β, versus the signal-to-noise ratio R for several assumed levels of Type-I error, α, in the test on mode detection by a single station. The detectability threshold R_d is defined as the value of R for $\alpha = 0.001$ and $\beta = 0.5$. This corresponds to making a false positive detection 0.1% of the time and a false negative 50% of the time. The detectability threshold for the detection of a single mode at a single station is $R_d = 8.5$.

Mode detection by a network

A mode-excitation detector can be made more powerful and more robust by requiring that a particular mode be simultaneously detected by a subset of seismic stations in a global network. Our algorithms for mode and event detection by a network are formulated in terms of sums across an array of zeros and ones I_{ilp}, here called the detection matrix. When a detection is registered at the $100(1-\alpha)\%$ confidence level in the lth mode band for some time interval $[t_i, t_i+T_l]$ recorded by the pth station, then I_{ilp} is assigned a value of unity; otherwise, it is set at zero.

Suppose there are N_{il} stations available for fixed i and l. If the time series is dominated by noise, then the sum

$$J_{il} = \sum_{p=1}^{N_{il}} I_{ilp} \quad (5)$$

will be a sample of a binomially distributed random variable with sample size N_{il} and success probability α. We say the network has detected the excitation of the lth mode at time t_i at the $100(1-\alpha')\%$ confidence level if J_{il} exceeds the critical value for the $100\alpha'\%$ upper tail of this binomial distribution. For example, if $N_{il} = 10$ and $\alpha = 0.1$, the critical value for $\alpha' = 0.05$ is 3, so that a mode must be detected by three or more stations at the 90% confidence level to be detected by a 10-station network at the 95% confidence level.

Because decisions are made on the basis of a summed-score statistic rather than, say, a sum over γ^2, the network mode detector is more robust with respect to nonstationarity and non-Gaussian behavior of the noise. Moreover, we place at our disposal the parameter α, which can be set at the value that minimizes the Type-II error level β' for a specified Type-I error level α' and snr R. This optimization procedure is discussed in Appendix A. As indicated in Figure A2, the minimum in the curve of β versus α is rather broad for a fixed snr near or above the detection threshold, so that in practice the precise choice of α is not critical. However, setting it to be an extreme value, either too large or too small, can substantially decrease the power of the test.

Figure 3 shows the dependence of β' on R for several different values of α' in the case of a 10-station network. Each point on these curves is calculated from the optimal value of α. For $\alpha' =$

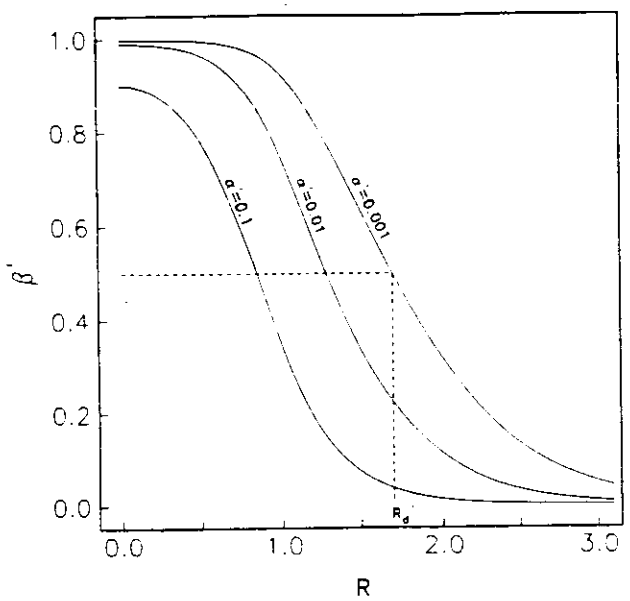

Fig. 3. The level of Type-II errors, β', versus the signal to noise ratio R for several assumed levels of Type-I error, α', for the detection of a mode by a 10-station network. The detectability threshold is reduced to $R_d' = 1.7$. The use of a global network affords 10 independent observations of the excitation level and greatly increases the power of the test.

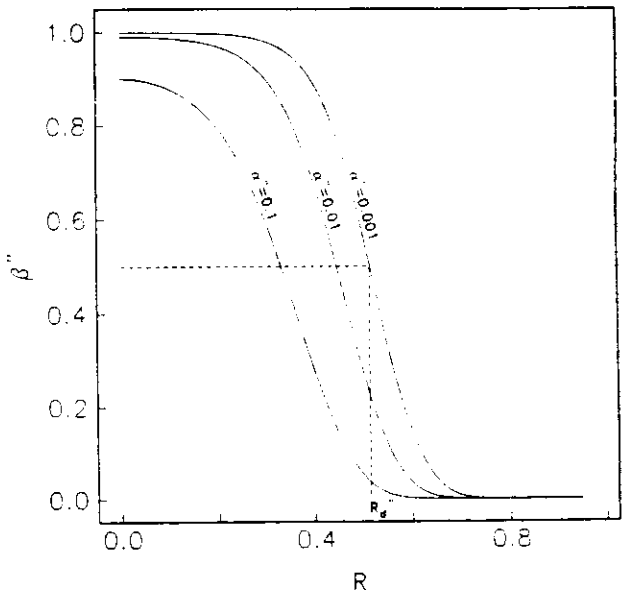

Fig. 4. The level of Type-II errors, β'', versus the signal to noise ratio R for several assumed levels of Type-I error, α'', for the detection of an excitation event by a 10-station network over a range of 36 modes. The detectability threshold is reduced to $R_d'' = 0.51$. By considering a range of modes recorded on a network of stations we increase the number of observations to 360 and obtain a substantially more powerful test. An event at the detectability threshold has a snr of 0.5 and would not necessarily be difficult to detect in a visual inspection of the time series.

0.001, the network detectability threshold for a single mode is $R_d' = 1.7$, a factor of 5 reduction from the single-station/single-mode case of Figure 2.

Event detection by a network

A time-localized seismic event will excite modes across a broad frequency spectrum. To test for significant seismic activity localized near a time t_i, we sum the detection matrix over all N_{il} stations and all observed modes between a lower cutoff $l_{\min}$ and an upper cutoff $l_{\max}$

$$K_i = \sum_{l=l_{\min}}^{l_{\max}} J_{il} = \sum_{l,p} I_{ilp} \tag{6}$$

If each element in the sum is an independent random variable, then K_i is binomially distributed with sample size

$$N_i = \sum_{l=l_{\min}}^{l_{\max}} N_{il} \tag{7}$$

and success probability α. We say the network has detected an event at time t_i at the $100(1-\alpha'')\%$ confidence level if K_i exceeds the critical value for the $100\alpha''\%$ upper tail of this binomial distribution. (As discussed in the next section, practical considerations dictate that the noise bands for adjacent modes overlap, which introduces correlations among elements of the detection matrix, and the distribution law for K_i is not binomial but must be calculated using Markov statistics. Here, for simplicity in presenting the basic concepts, we ignore this complication.)

Figure 4 shows the relation between R and β'' for different levels of α'' in the case of a 10-station network recording 36 modes with equal snr. Because the sample size is much larger than for a single mode ($N_i = 360$), the probability of making a Type-II error rolls off more rapidly with R, and the power of the test is considerably enhanced. For $\alpha' = 0.001$, the detectability threshold is $R_d'' = 0.51$. This represents a gain of 3.3 over the network/single-mode example of Figure 3 and a gain of 17 over the single-station/single-mode example of Figure 2. Hence using seismic networks of only modest size, we can detect an event having an snr less than unity with very little risk of making a false detection. An event with such a low snr would not necessarily be evident from a visual inspection of the seismograms.

DETECTOR DESIGN FOR FUNDAMENTAL SPHEROIDAL MODES RECORDED BY THE IDA NETWORK

We applied our detection algorithm to IDA data for the 2-year period 1978-1979, when the network comprised up to 11 stations (Figure 5). Editing the raw IDA data for dropouts, glitches, earthquake-associated nonlinearities, and periods of high noise levels was necessary before applying the mode-excitation detec-

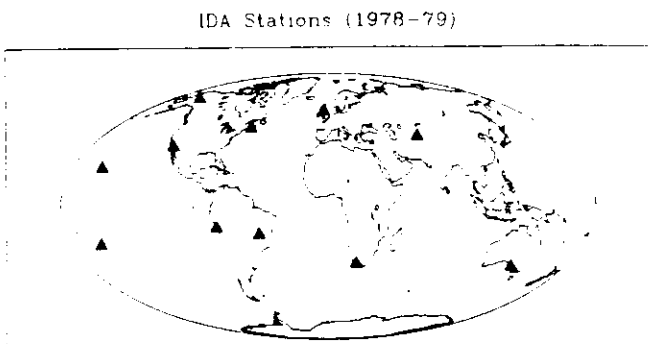

Fig. 5. Location of the International Deployment of Accelerometers (IDA) network stations (triangles) operating during the period 1978-1979.

tor. The labor of editing was reduced using a high-speed, interactive-graphics workstation, but this step still dominated the processing effort. A matched-filtering algorithm was used to remove tides from the edited records, and the resulting time series were fed to a four-headed Alliant FX/40 parallel processor for further analysis.

The detector was run on the fundamental spheroidal modes ${}_0S_l$, $2 \le l \le 43$, using time windows lagged by 3 hours, for every available station in the IDA network. (Stations lacking more than 20% of the data for a given time window were excluded from the analysis.) These modes have large excitation kernels in the crust and upper mantle, so they are sensitive to shallow sources, and their average multiplet eigenfrequencies are accurately determined [*Silver and Jordan*, 1981; *Masters and Gilbert*, 1983]. ${}_0S_l$ modes in this band are particularly convenient to use because they have relatively high quality factors and their resonance peaks are therefore well spaced in frequency (Figure 6). Moreover, the interference by overtones is relatively small, since many of the higher modes are not efficiently excited by seismic events in the crust and upper mantle.

Throughout our analysis we ignore the presence of overtones. Because the overtones generally contribute relatively more energy to the noise bands than the signal bands for any finite value of R, this decreases the power of the test and tends to bias our decisions to be "conservative;" namely we register fewer positive detections than if we explicitly accounted for overtone activity.

The normal-mode parameters used in the processing are listed in Table 1. For each angular order l, these include a center frequency ω_l, an attenuation factor $\alpha_l = \omega_l / 2Q_l$, a window length

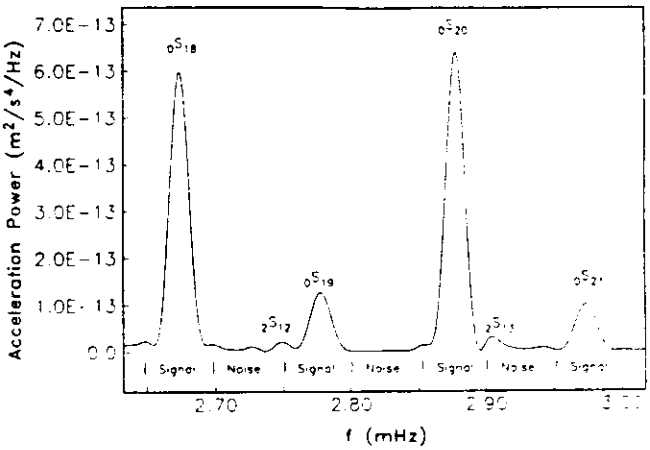

Fig. 6. Power spectral density for a 24-hour time window following the 1979 Peru-Columbia earthquake for IDA station BDF. Frequency is shown in millihertz (mHz) on the horizontal axis. The prominent spectral peaks correspond to the fundamental spheroidal modes ${}_0S_l$ for the range l = 18-21. The peak shape is influenced by lateral heterogeneity and attenuation. As Q_l decreases, the widths of the resonance peak increases. Splitting due to rotation and asphericity will also broaden the peak. We adopt a simple model in which the spectrum is divided into signal and noise bands. The signal bands are centered on the fundamental mode resonance peaks and have a width proportional to the attenuation parameter $\alpha_l = \omega_l / 2Q_l$. The noise bands are located between the resonance peaks. At higher angular orders the resonance peaks leak into the noise band and decrease the snr. Overtones such as ${}_2S_{12}$ and ${}_2S_{13}$ generally have much smaller amplitude than the fundamental modes for events in the crust and upper mantle over the frequency band 0-5 mHz.

TABLE 1. Fundamental Spheroidal Mode Parameters

Angular Degree	f_l*, mHz	α_l*, mHz	T_l, hours	w_l^{eff}, mHz	τ_l, hours
2	0.3092	0.002	436.3	0.003	157.1
3	0.4684	0.003	290.9	0.003	96.0
4	0.6465	0.005	174.5	0.003	20.9
5	0.8397	0.007	124.7	0.003	21.8
6	1.0386	0.010	87.3	0.004	17.9
7	1.2314	0.010	87.3	0.004	18.8
8	1.4124	0.012	72.7	0.005	16.4
9	1.5767	0.015	58.2	0.006	13.7
10	1.7238	0.017	51.3	0.006	12.1
11	1.8626	0.024	36.4	0.010	7.6
12	1.9909	0.020	43.6	0.009	8.9
13	2.1130	0.021	41.6	0.007	10.4
14	2.2309	0.024	36.4	0.008	9.1
15	2.3461	0.023	37.9	0.008	9.3
16	2.4582	0.027	32.3	0.010	7.9
17	2.5674	0.030	29.1	0.010	7.6
18	2.6734	0.033	26.4	0.011	7.1
19	2.7758	0.038	23.0	0.012	6.5
20	2.8766	0.036	24.2	0.012	6.7
21	2.9761	0.036	24.2	0.012	6.7
22	3.0739	0.038	23.0	0.012	6.5
23	3.1704	0.040	21.8	0.013	6.4
24	3.2651	0.042	20.8	0.014	6.1
25	3.3587	0.047	18.6	0.015	5.3
26	3.4515	0.048	18.2	0.015	5.3
27	3.5431	0.051	17.1	0.016	5.2
28	3.6343	0.054	16.2	0.017	4.8
29	3.7243	0.055	15.9	0.018	4.6
30	3.8144	0.058	15.0	0.019	4.5
31	3.9049	0.062	14.1	0.020	4.2
32	3.9942	0.063	13.9	0.020	4.2
33	4.0832	0.072	12.1	0.023	3.8
34	4.1713	0.072	12.1	0.023	3.8
35	4.2616	0.077	11.3	0.025	3.5
36	4.3511	0.076	11.5	0.024	3.5
37	4.4407	0.078	11.2	0.025	3.4
38	4.5301	0.081	10.8	0.026	3.3
39	4.6192	0.089	9.8	0.028	3.0
40	4.7080	0.091	9.6	0.029	2.9
41	4.7982	0.093	9.4	0.030	2.9
42	4.8886	0.094	9.3	0.030	2.8
43	4.9772	0.104	8.4	0.033	2.5

* ${}_0S_2$-${}_0S_7$ after *Sailor and Dziewonski* [1978]; ${}_0S_8$-${}_0S_{43}$ after *Masters and Gilbert* [1983].

T_l, an effective half width for the spectral integration, w_l^{eff}, and a window shift parameter τ_l. We set ω_l and Q_l equal to the average apparent eigenfrequencies and quality factors observed by *Masters and Gilbert* [1983]. Our definitions and specifications of the other parameters are discussed below.

Time-domain formulation

Our detector employs the modulus of the zeroth-order moment of the complex spectrum to characterize the spectral level in the mode and noise bands. Rather than Fourier transform the IDA records and integrate the spectrum in the frequency domain as in equation (2), we calculate the zeroth-order moment by a time-domain integration technique [*Riedesel et al.*, 1986]. The spectral integral in (2) can be viewed as the convolution of the complex Fourier spectrum $u(\omega)$ with a boxcar window of width $2w_l$ lagged by the center frequency ω_l of the lth mode. Hence the convolution theorem allows us to reformulate the zeroth-order moment as a time-domain Fourier integral of the form

$$\mu_0(\omega_l) = \int_{-\infty}^{\infty} F_l(t)\, u(t)\, e^{-i\omega_l t} dt \tag{8}$$

where the integration kernel is

$$F_l(t) = 2w_l \operatorname{sinc}(w_l t)\, W_l(t) \tag{9}$$

Each data functional $\mu_0(\omega_l)$ can thus be computed from a complex-valued, time-domain integration that is efficiently coded for parallel processing. A single pass through the 2-year data set involves 2×10^7 such integrations, so the computational advantage of (8) relative to (2) can be easily appreciated.

Tailoring the windows

The time-domain formulation has the additional advantage of allowing the window length to be tailored to the particular mode. We took the windowing function $W_l(t)$ to be a Hanning taper of length T_l:

$$W_l(t) = \frac{1}{2}\left[1 - \cos(2\pi t/T_l)\right] H(t) H(T_l - t) \tag{10}$$

In this expression, $H(t)$ is the Heaviside step function. By extensive numerical experimentation with real and simulated data, we found that varying T_l with the mode frequency ω_l and quality factor Q_l substantially improves the detectability of a normal mode peak. These experiments showed that a window length of Q_l cycles is close to optimal, and we adopted this scaling for our data processing. This length is twice the value of the $0.5Q_l$ cycles found by *Dahlen* [1982] to be theoretically optimal for the determination of amplitude by least squares procedures, primarily because a longer integration length is required to suppress spectral leakage from the mode signal bands to the intermode noise bands. As shown in Table 1, the integration lengths range from 436 hours for the mode ${}_0S_2$ to 8.4 hours for the mode ${}_0S_{43}$.

The spectral integration parameter w_l was also scaled according to the modal attenuation, in this case proportionally to the attenuation factor α_l. The Hanning taper in the windowing function (10) interacts with the sinc function in the time domain kernel (9) to produce a spectral integration window whose shape is not a boxcar and whose half width differs from w_l. For specified values of T_l and w_l, we calculated an effective half width w_l^{eff} from the second moment of the squared amplitude spectrum. For modes with $l > 7$, we found the best spectral window shapes and widths were obtained from the scaling $w_l^{\text{eff}} \sim 0.3\alpha_l$. At very low frequencies, we tried to compensate for the effects of multiplet splitting owing to rotation and lateral heterogeneity by increasing this scale factor, but the attempt was largely unsuccessful; the combination of splitting and increasingly high noise levels makes it very difficult to detect mode excitation for $l \leq 7$, as we shall see. For large l, the effective modal half-width is larger than one-fourth the intermodal spacing, so that adjacent mode and noise bands partially overlap, introducing a small correlation between signal and noise, which we ignore in our analysis. The precise values of w_l^{eff} are given in Table 1.

To maximize the probability of detecting an event at the fiducial time t_i, it is advantageous to shift the start times of the integration windows by an amount that depends on the angular order l. Suppose a discrete seismic event occurs exactly at t_i; then the displacement at a particular station due to the lth (unsplit) mode can be expressed

$$u_l(t) = A_l C_l(t - t_i) \tag{11}$$

where A_l is an amplitude factor that depends on the source-receiver geometry and $C_l(t)$ is the decaying cosinusoid

$$C_l(t) = H(t)\, e^{-\omega_l t/2Q_l} \cos(\omega_l t) \tag{12}$$

For a window that begins at t^*, the zeroth moment of this time series is proportional to the complex number

$$b_l(t_i - t^*) = \int_{-\infty}^{\infty} C_l(t + t^* - t_i) F_l(t)\, e^{-i\omega_l t} dt \tag{13}$$

and the detection statistic γ^2 is proportional to the nonnegative real number $|b_l(t_i - t^*)|^2$. As the lag between the event start time t_i and the window start time t^* varies, the expected value of γ^2 will vary, reaching a maximum at a unique lag time τ_l that depends only on the parameters of the lth mode. Hence the probability of detecting an event is maximized if the window start time equals $t^* = t_i - \tau_l$, which is different for each mode. In order to align these maxima and thus optimize the detection capability for an event at a fiducial time t_i, we begin the window for the lth mode at $t_i - \tau_l$. The time shifts τ_l, computed from the mode parameters by numerical quadrature, are listed in Table 1.

Refinement of detector statistics

Because the frequency spacing of the fundamental spheroidal modes is comparable to the integration width $2w_l$, the computation of γ^2 (equation (3)) was performed by overlapping the upper and lower noise bands of the l and $l+1$ modes, respectively. This introduces statistical correlations among the elements of the detection matrix I_{ilp} that must be included in computing the critical values of the statistic K_i used to assess the significance level of an excitation event.

K_i is the sum of the detection matrix I_{ilp} over modes and stations (equation (6)). For i and p fixed, the sequence $\{I_{ilp} : l = l_{\min}, l_{\min}+1, \ldots, l_{\max}-1, l_{\max}\}$ is pairwise correlated and thus forms a Markov chain [*Feller*, 1968]. The properties of this Markov chain are given by the conditional probabilities $P(I_{il+1p} \mid I_{ilp})$

which are elements of the 2 × 2 transition matrix

$$\mathbf{P} = \begin{bmatrix} P(1|1) & P(0|1) \\ P(1|0) & P(0|0) \end{bmatrix} \quad (14)$$

In the case when there is no excitation and the noise samples do not overlap, the events I_{il_p} and I_{il+1_p} are independent, and matrix elements are $P(1|1) = P(1|0) = \alpha$, and $P(0|1) = P(0|0) = 1-\alpha$, leading to a binomial distribution for K_i, as discussed in the previous section. When the noise samples do overlap, the transition probabilities must be calculated numerically. In our analysis of IDA data, the center frequencies of these noise bands were chosen to be equal, $\omega_i^+ = \omega_{i+1}^-$, and we adopted $\alpha = 0.5$. From a Monte Carlo calculation for a 1-year sample of colored noise, we obtained

$$\mathbf{P} = \begin{bmatrix} 0.548 & 0.452 \\ 0.460 & 0.540 \end{bmatrix} \quad (15)$$

Hence the probability of making a Type-I error for a given mode is greater when a Type-I error occurs for an adjacent mode (0.548) than when it does not (0.452). The Monte Carlo calculation also yielded a probability distribution for K_i, which was used to obtain critical values for testing H_0 against H_1 in the analyses of the real and simulated data sets. In subsequent sections we refer to this procedure as the Markov test.

Noise characteristics

Our noise model is that of a Gaussian random process with a frequency dependent power spectral density $\nu^2(\omega)$. To investigate the character of noise for real IDA data, we calculated power spectral densities for the 11 IDA stations operating during a 20-day period of relatively low seismic activity from November 6 to 26, 1978. The acceleration spectra of these noise samples, shown in Figure 7, have different amplitudes but similar shapes. They are fairly flat above 2 mHz but increase rapidly below this value, a behavior found in previous studies of low-frequency noise [*Agnew and Berger*, 1978].

The differences in the absolute levels reflect local environmental effects and near-field noise sources. The station with the highest noise level is Rarotonga (RAR) in the Cook Islands, which *Agnew and Berger* [1978] attributed to coastal edge waves. A sophisticated mode-excitation detector would account for systematic noise-level differences among stations. Ours does not, so that including noisy data will decrease its performance in detecting low-amplitude events. Since the noise levels at RAR are consistently much greater than at other IDA stations, we decided to exclude all records from this station in the data analysis. We also endeavored to edit out obviously noisy periods at other stations.

Figure 8 compares the network-averaged values of the squared moment $|\mu_0|^2$ for the fundamental-mode bands (points) with the values interpolated between noise bands (solid line) over the same 20-day quiet interval. The averages were normalized by the integrals for a white spectrum, so that their frequency variation represents the average of the noise spectra in Figure 7. Despite the fact that the interval was chosen to avoid significant earthquake activity, there was enough background seismicity (and/or other forcing functions of unidentified origin) to excite some of the modes with frequencies greater than 2 mHz to slightly higher levels than the noise.

In Figure 9 we apply the same procedure to the entire 1978-1979 period, which includes many large earthquakes. For this 2-year average, the mode-band and noise-band levels below about 1.4 mHz ($_0S_8$) are nearly equal to each other and only marginally

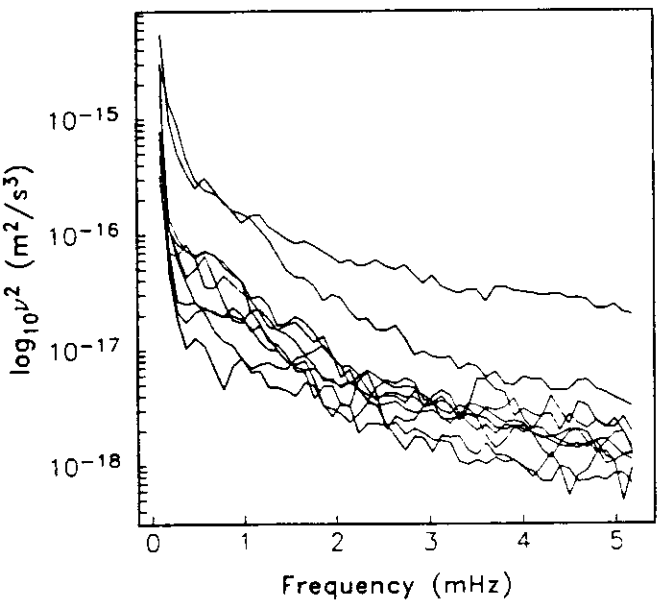

Fig. 7. Acceleration power spectral densities for the 10 IDA stations from November 6, 1978 to November 26, 1978 in the band 0-5 mHz in m^2/s^3 (m^2/s^4/Hz). Glitches, particularly noisy periods, and tides were removed from the data prior to calculation of the power spectra. Most of the stations have a relatively low noise level of about 1.4×10^{-18} m^2/s^3 above 2 mHz. Below 2 mHz the noise levels rise rapidly with decreasing frequency. The noisiest station for this time interval was RAR in the Cook Islands. This station was consistently noisy and was not used to register detections.

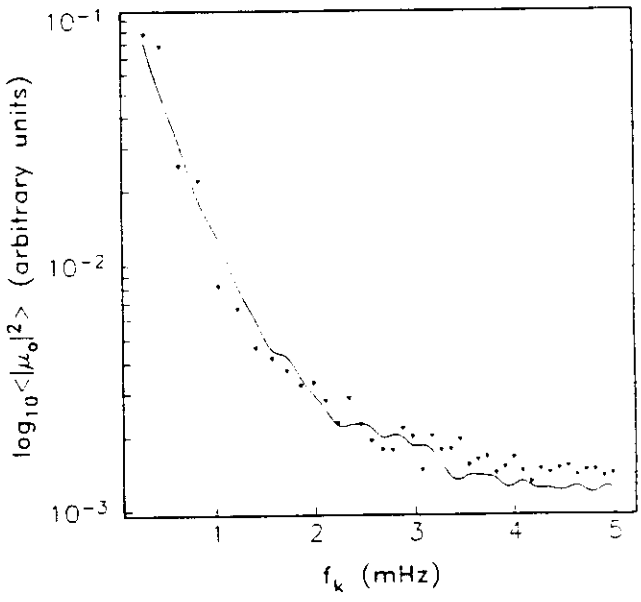

Fig. 8. Averaged values of $|\mu_0|^2$ for the noise bands for the same quiet interval used to calculate the power spectra in Figure 7 are shown with a solid line. Averaged values for the mode bands for the same interval are shown with solid triangles. The slowly varying level of the noise above 2 mHz and the rapidly increasing level of noise below 2 mHz are consistent with our measurements of the power spectra for the same period. Although the interval spans a lull in global seismic activity, there was enough activity to excite the mode bands slightly above the noise bands.

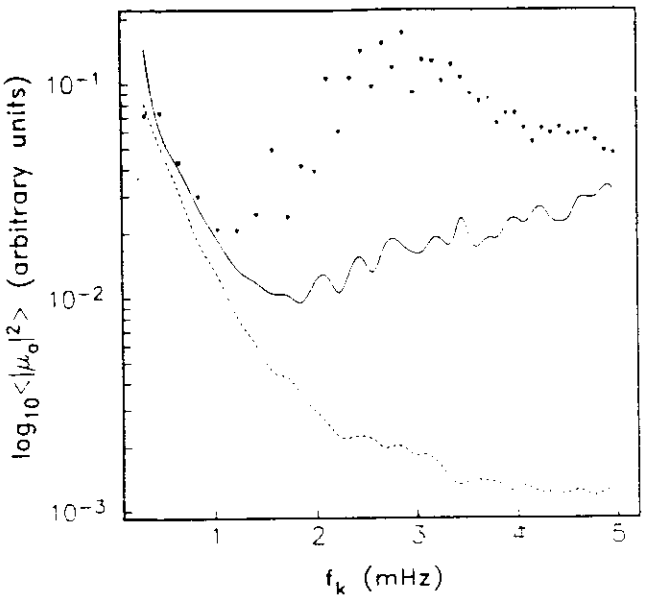

Fig. 9. Averaged values $|\mu_0|^2$ of the noise bands are plotted with a solid line as a function of frequency in mHz for the entire 2-year period 1978-1979. Plotted as a dashed line is the same quantity for the quiet period as shown in Figure 8. The level of signal above about 1.4 mHz is substantially higher than the noise. Below 1.4 mHz the signal is slightly stronger or comparable to the noise. The higher level of noise over the two year interval as compared to the 20-day quiet interval is a consequence of signal-generated noise. The sources of signal generated noise are increased instrument noise during large-amplitude oscillations in earthquakes, the presence of overtones in the noise bands, and leakage of fundamental mode resonance peaks from the signal bands into the noise bands. The latter two sources of noise are primarily responsible for the gradual increase in noise above 2 mHz.

above the quiet-period levels, reflecting the low snr at these very low frequencies. This is unfortunate because the excitation of these low-degree modes provides useful constraints on the nature of seismic sources with low characteristic rupture velocities. Because poor snr implies poor detector performance, we chose to exclude modes of angular order $l \leq 7$ in computing the K_i statistics. In the future, we should be able to improve the snr for $l \leq 7$ by formulating detectors that explicitly include free-oscillation splitting due to rotation and aspherical heterogeneity.

At frequencies above about 1.4 mHz, the levels in the signal bands are substantially higher than in the noise bands, owing to fundamental-mode excitation by large earthquakes. The signal power peaks between 2.5 and 3.5 mHz (${}_0S_{16}$-${}_0S_{27}$), known among free-oscillation afficianados as the cleanest spectral interval for measuring the properties of fundamental spheroidal modes. However, Figure 9 also shows that relative to the quiet period, the power in the noise bands increases almost exponentially out to 5 mHz, where it once again approaches the signal-band levels. This signal-generated noise is due primarily to two effects, the excitation of overtones contained within the noise bands and spectral leakage from the fundamental modes, whose attenuation half widths approach the intermode spacing (Table 1). As previously noted, this signal-generated noise, which we ignore in our formulation, does not affect the Type-I error rate, but it does increase the frequency of Type-II errors and thereby lowers the power of the detector. Again, designing a more sophisticated detector that takes better advantage of our knowledge of the free-oscillation spectrum is an easily contemplated goal for future research.

NUMERICAL EXPERIMENTS WITH SIMULATED DATA

We have tested the validity of our statistical assumptions by applying the detection algorithm to a series of carefully constructed, synthetic data sets containing simulated earthquakes as well as noise. These tests have been used to guide our theoretical development, to confirm that the detector performs as theoretically predicted when the statistics of the data conform with our statistical model, and to determine how well it works when the underlying statistics have properties that are less ideal but more representative of real data. Illustrated here are two experiments: an application of the detector to a synthetic noise sample with realistic power spectra, and a determination of the detection threshold for simulated, shallow-focus, strike-slip events on a mid-Atlantic transform fault. Our discussion of these experiments allows us to introduce the parameter values and plotting conventions employed in the application of the detector to real IDA data.

Testing the detector with simulated noise

As an example of one of these tests, we applied the detector to an entire year of Gaussian random noise samples generated from power spectra conforming to the observed spectra in Figure 7 for the 10-station network comprising the IDA instruments BDF, CMO, ESK, GAR, HAL, KIP, NNA, PFO, SUR, and TWO. (Since we dropped RAR from our data set because of its high noise levels, we also excluded it from this experiment.) As in the case of the actual data processing, the test was performed by integrating the noise samples over time windows $[t_i - \tau_l, t_i - \tau_l + T_l]$ with fiducial times spaced by 3 hours (i.e., $t_{i+1} - t_i = 3$ hours) for the modes ${}_0S_8$-${}_0S_{43}$ using the window parameters T_l and τ_l given in Table 1. The experiment resulted in a detection matrix I_{ilp} with about 2.1 million entries. An element of the detection matrix was recorded as 0 or 1 depending on whether $\gamma^2 \leq \gamma^2_{0.5}$ or $\gamma^2 > \gamma^2_{0.5}$, respectively. In other words, the excitation of individual modes at individual stations was tested at the 50% confidence level, which is nearly optimal for maximizing the power of both the J_{il} and K_i tests for snrs near the detection thresholds (Appendix A).

Figure 10 shows a 30-day sample of the results, plotted in the standard format used throughout the rest of this paper. Time increases from the top to the bottom of the plot; day of the year is listed in 10-day increments on the right-hand side. The left-hand side is a seismicity diagram where earthquakes are indicated by their origin time and magnitude; in this case it is left blank because there are no events. Network detections of individual fundamental modes registered for $\alpha' = 0.1$ are indicated by solid circles, with angular order increasing from left to right. The graph in the middle of the diagram represents the significance level for the K_i statistic, represented in terms of the Type-I error rate α'' expressed as a percent. α'' is plotted on an inverse logarithmic scale to emphasize differences at the high confidence levels we use to register detections; e.g., the line labeled 0.1% corresponds to the 99.9% confidence level for event detection by the network.

In the mode-detection segment of the plot, the number of dots should ideally be 10% of the total number of mode samples (dots plus blanks), since our convention is to test the J_{il} statistic at the 90% confidence level. The fraction calculated from this theoretical experiment is instead 5.8%. The discrepancy is easily understood: it is almost entirely due to the discreteness of the binomial probability distribution. For the 10 trials that constitute each binomial test, choosing $\alpha' = 0.1$ requires that eight modes have values of γ^2 larger than $\gamma^2_{0.5}$ for J_{il} to exceed its critical

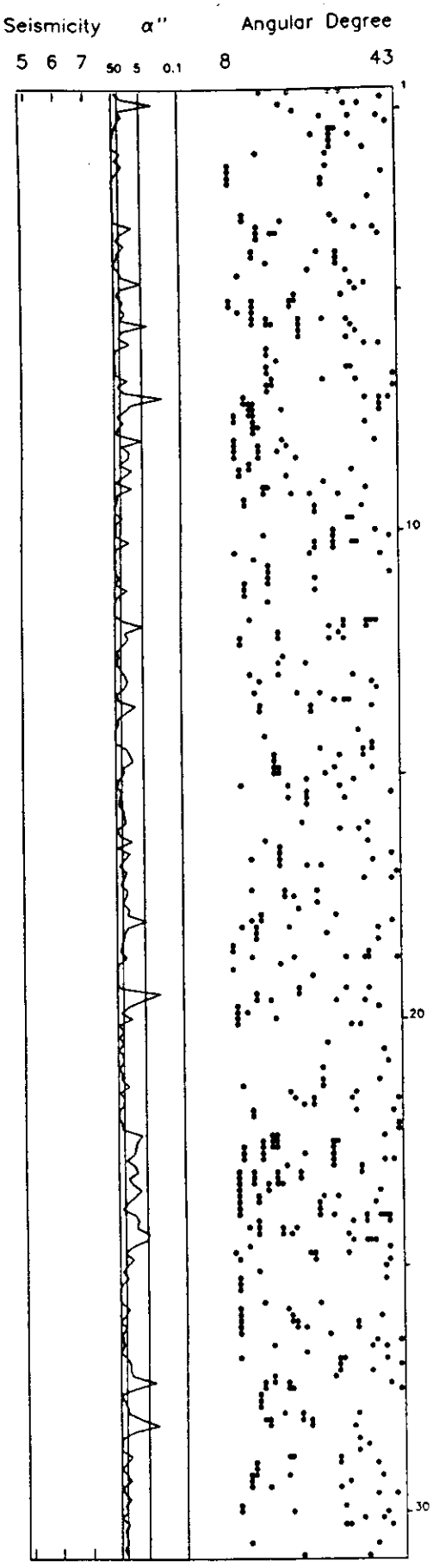

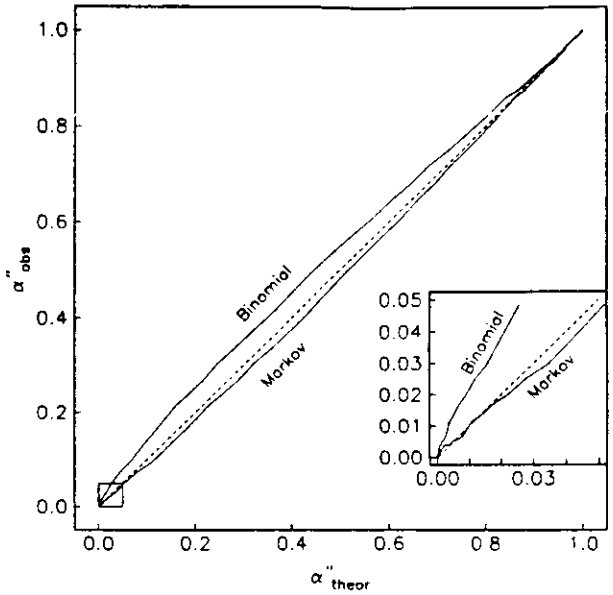

Fig. 11. A plot of the theoretical versus observed level, α'', of Type-I errors for a 1-year sample of colored, Gaussian random noise. The dashed line indicates the ideal relationship between theoretical and observed error levels. The insert shows an enlarged view of the lower left corner of the plot. The binomial test, which assumes that each observation is independent, has consistently too many false positives, whereas the Markov test, which accounts for correlations in the values of modes of adjacent angular order l, has slightly too few. We adopt the Markov test in all subsequent calculations because it is closer to the ideal relationship, is slightly conservative, and correctly accounts for known correlations.

value. However, a total of eight positive trials is also significant for Type-I error rates as low as α'=0 .055, and this lower bound is in good agreement with the numerically derived rate of 0.058. As long as the number of stations in the network remains constant, we could just redefine the significance level at this value. However, in practice, station drop-outs are common; we exclude stations where more than 20% of the data is missing or has been edited out from a given time window, so that this discreteness effect cannot be entirely avoided. We therefore retain $\alpha' = 0.1$ as our convention, and the test on J_{il} thus tends to be conservative (fewer than 10% Type-I errors).

Vertical runs of Type-I errors are evident in Figure 10, especially at lower frequencies. Since the sample separation is only 3 hours, whereas the window lengths range from 8.4 to 73 hours, the integration windows overlap and temporal correlations in γ^2, and thus in the J_{il} and K_i statistics, are expected. The correlation time in the Type-I error process for J_{il} should decrease with

Fig. 10 (opposite). A detection diagram displays the results of running the algorithm on a 30-day sample of colored noise. Time increases from top to bottom. Day of year is shown on the right-hand side of the plot with tick marks at 5-day intervals. Solid dots on the right-hand side of the figure indicate fundamental spheroidal modes excited above the noise at the 90% confidence level; mode range is ${}_0S_8$ (1.4124 mHz, 11.8 min) through ${}_0S_{43}$ (4.9772 mHz, 200 s). Detection intervals were spaced every 3 hours. Integration lengths depend on mode number (Table 1). The continuous line to the left of the mode excitation diagram is a graph of the significance level of K_i for all the modes as recorded by the entire IDA network. Seismicity, of which there is none in this test case, will be plotted on the left-hand side of the diagram.

increasing l, as observed. It is evident from Figure 10 that at the 90% confidence level used in our calculations, the correlation time for $l = 8$ is only a few samples. Because we use only modes with $l \geq 8$ in computing the K_l statistic, the effective correlation time for its Type-I error process is less than one sample at confidence levels greater than about 95%. In the absence of genuine mode-excitation events, consecutive samples where K_l exceeds its 99.9% significance level are thus expected to be extremely rare.

Figure 10 comprises 240 time samples, and the graph of α'', which is based on what we are calling the Markov test, shows seven false event detections at the 95% confidence level and none at the 99.9% confidence level, more-or-less consistent with the expected rate of Type-I errors. Figure 11 displays the comparison between the theoretical and experimental false-event error rates obtained from the 2920 samples in the entire 1-year simulation, plotted as a function of α''. Two curves are shown, one for the binomial test, which ignores the mode-to-mode correlations due to overlapping noise bands, and one for the Markov test, which includes them. At high confidence levels ($\alpha'' \leq 0.05$; see inset diagram), the binomial statistics yield Type-I error rates that are about a factor of 2 higher than those observed, whereas the predictions of the Markov statistics are very nearly correct. We employ Markov statistics in all of our subsequent calculations of event significance levels.

Testing the detector with simulated events

The sensitivity of the event detection algorithm was tested by applying it to synthetic seismograms superposed on a background of simulated IDA-network noise. We illustrate the results for a shallow-focus, strike-slip event whose location and source mechanism correspond to the March 20, 1978, slow earthquake that took place on the St. Paul transform fault in the central Atlantic Ocean. The surface-wave magnitude assigned to this event by the International Seismological Centre (ISC) was $M_S = 5.8$, and its CMT moment was $M_0 = 2.4 \times 10^{18}$ N m. Here and elsewhere in this paper it will be convenient for us to express seismic moment in terms of the unified magnitude [*Hanks and Kanamori*, 1979],

$$M_w = \frac{2}{3}\log_{10} M_0 - 6.03 \qquad M_0 \text{ in N m} \qquad (16)$$

For this event, $M_w = 6.2$.

Complete normal-mode synthetics were calculated for the 10 IDA stations assuming an instantaneous source time function. Scaled versions, corresponding to various values of M_w, were added to Gaussian noise with spectra like those in Figure 7, and the resulting time series were convolved with the instrument responses. Figure 12 is the detection diagram for the case $M_w = 6.8$ ($M_0 = 2 \times 10^{19}$ N m), which shows features typical of large

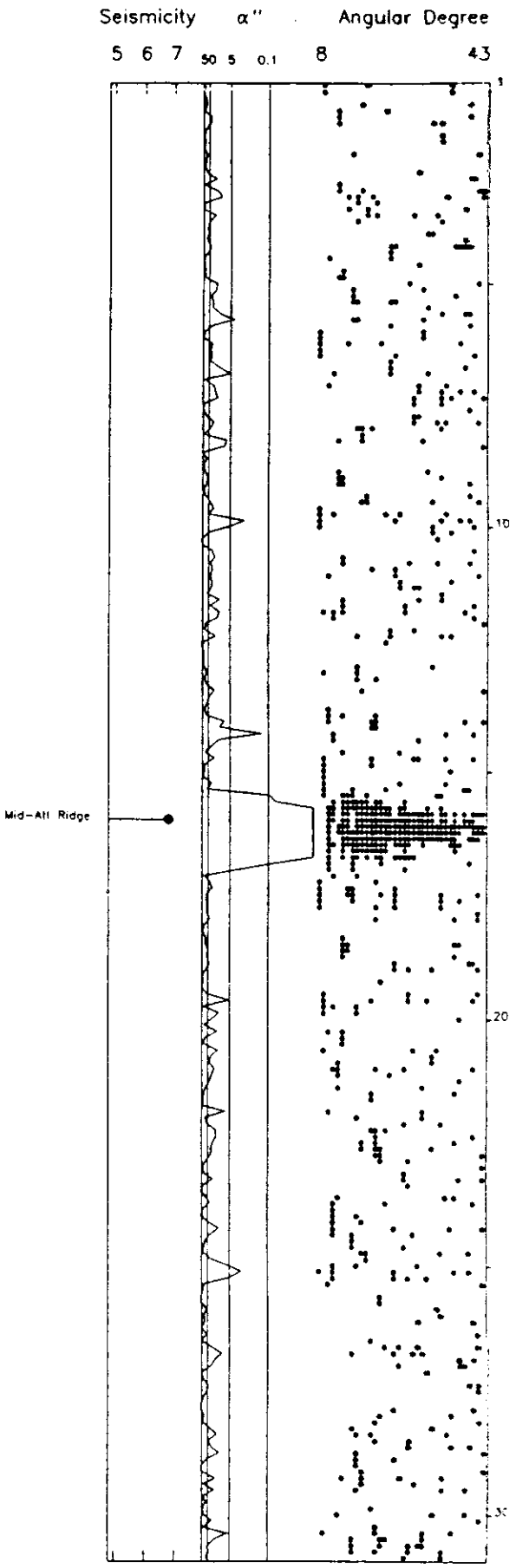

Fig. 12 (opposite). Detection diagram for a synthetic test case. Seismograms for the CMT solution for the March 20, 1978, M_S 5.8, central Mid-Atlantic Ridge earthquake were calculated by normal mode summation for each IDA station and convolved with the IDA instrument response. Amplitudes were scaled such that the event had a seismic moment of 5×10^{19} N m ($M_w = 6.8$). Gaussian random noise with the same spectral amplitude as recorded by the IDA network for the 20-day period of low seismic activity during November 1978 was added to the data. The left side of the figure shows the timing and size of the earthquake. The length of the horizontal bar indicates ISC magnitude (maximum of M_S or m_b). Plotted as a solid dot at the same scale is the moment magnitude as determined from the CMT estimate of the seismic moment [*Dziewonski et al.*, 1987*a*,*b*].

earthquakes. Individual ${}_0S_l$ modes excited by an event of this magnitude can be detected at the 90% confidence level down to 1.4 mHz ($l = 8$), with modes of lower angular order registering detections for a longer sequence of fiducial times t_i owing to their greater attenuation times and the correspondingly larger window lengths used in the time-series integration. Below 1.4 mHz, the noise levels increase rapidly (Figure 7), and the snrs of individual modes fall below the detectability threshold, which is why we use only modes with $l_{min} = 8$ in the summation to obtain event detection statistic K_i (equation (6)). This statistic registers a detection at the 99.9% confidence level for a 36-hour period extending from 15 hours prior to the event until 21 hours after it. The apparent acausality results from the finite lengths of the integration windows and backwards time shifts applied to maximize the detection probability.

Figure 13 shows the same detection diagram when the magnitude of the earthquake is reduced to 6.0 (1×10^{18} N m). Although the number of individual mode detections is much reduced, the K_i statistic still peaks above the 99.9% significance level. Repeating this experiment with many different noise samples, we find that an event of this size in this location is detected by the 10-station IDA network at the 99.9% significance level about 50% of the time. In our statistical terminology, the Monte Carlo calculation yields a Type-II error rate of $\beta'' = 0.5$ for a Type-I error rate of $\alpha'' = 0.001$, which is just our definition of the detection threshold. Expressed as an rms average of the normal-mode snrs for this simulated earthquake, we obtain $R_d'' = 0.76$. The empirical value determined for this particular source location is thus slightly larger than the theoretical detectability threshold of $R_d'' = 0.51$ obtained from Figure 4. The small discrepancy (only 0.1 unit of magnitude) is attributable primarily to the neglect of overtones and fundamental-mode leakage into the noise bands. Monte Carlo experiments with other earthquake simulations give similar results.

RESULTS: 1978-1979

Detection statistics have been calculated from IDA records for the 2-year period January 1, 1978 to December 31, 1979. The corresponding detection diagrams, comprising 5480 fiducial times sampled at 3-hour intervals, are presented in Appendix B. As an example for our discussion, the plot of a typical 30-day period, May 10, 1978 to June 8, 1978, is reproduced at an expanded time scale in Figure 14. The mode-detection statistics J_{il} (right side) and error rate α'' for the K_i statistic (center) conform to the conventions introduced in the previous section; in these respective fields, a solid circle represents a mode detection by the network at the 90% confidence level, and the vertical line labeled 0.1 represents an event detection at the 99.9% confidence level.

If the IDA time series recorded only broad-band Gaussian noise, then mode detections from an ideal 10-station IDA network would be expected 5.5% of the time (the ratio is less than 10% owing to the discreteness of the binomial distribution, as discussed previously). In fact, mode detections are registered for

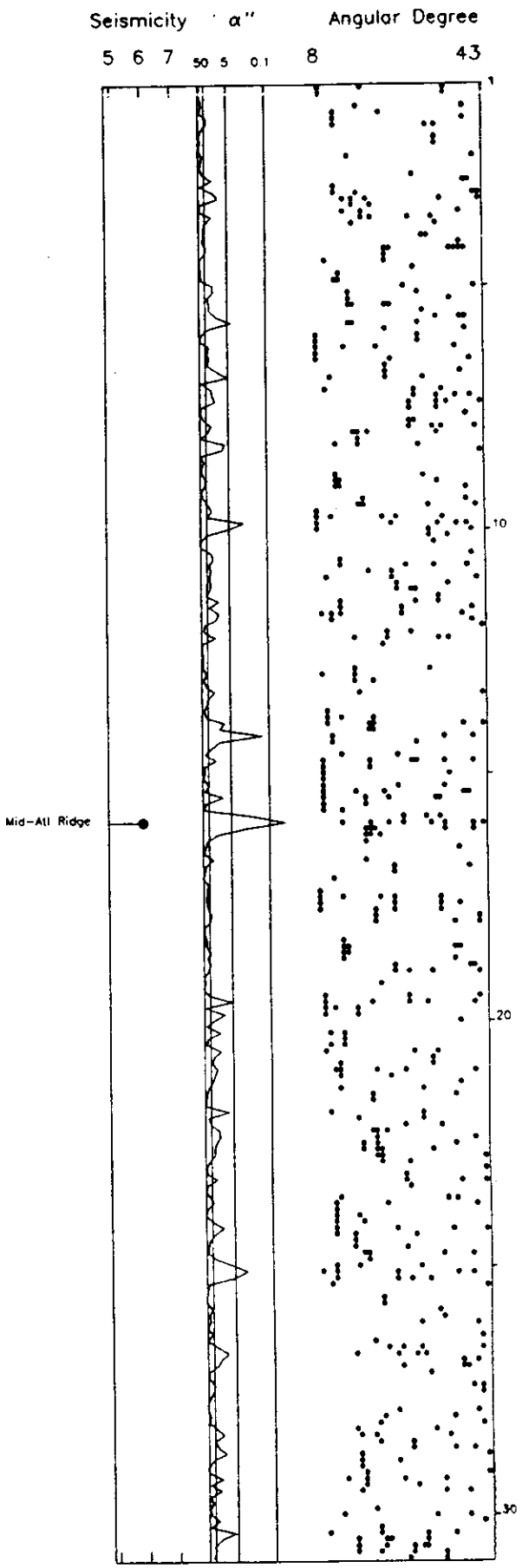

Fig. 13 (opposite). Detection diagram for an event with the same mechanism as in Figure 12. This event is at the detectability threshold ($M_0 = 1 \times 10^{18}$ N m, $M_w = 6.0$). The detectability threshold is defined as the signal strength at which a seismic event is detectable 50% of the time with a false detection only 0.1% of the time. For the particular example shown, the event is detected.

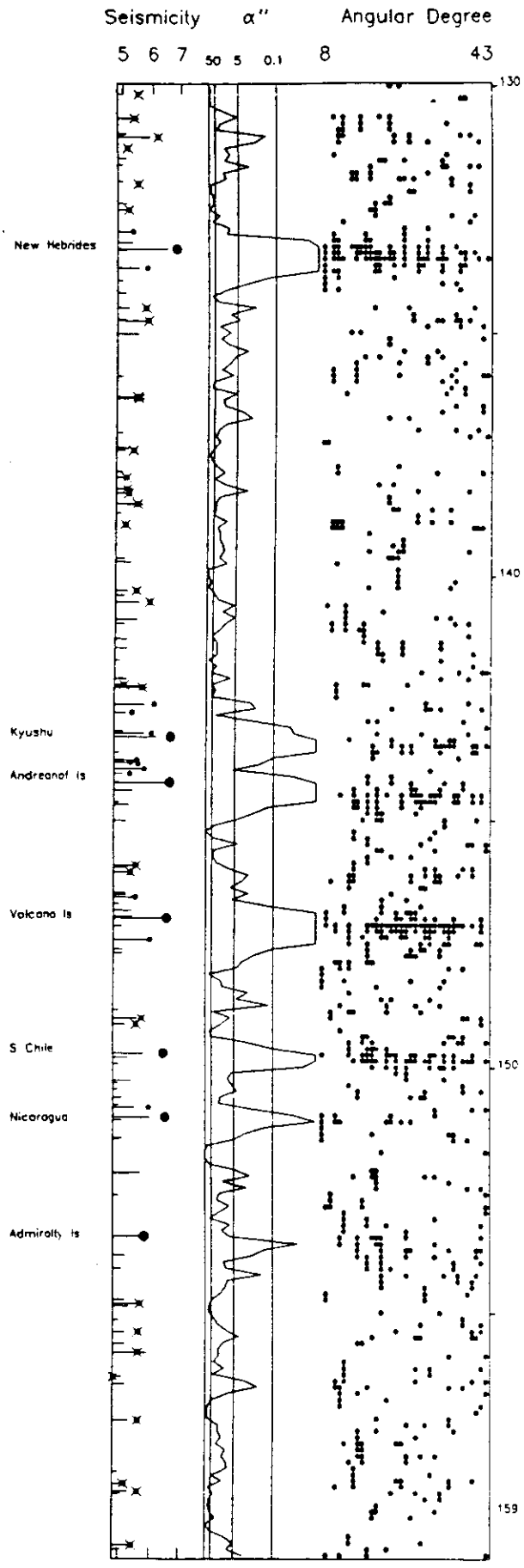

about 15% of 224,680 samples computed for the 2-year period, indicating substantial excitation of the fundamental spheroidal modes by seismic sources. The event-detection test is considerably more powerful: K_i exceeds its 95% confidence level 49% of the time and its 99.9% confidence level 23% of the time. We seek to understand to what extent this mode excitation can be explained by standard source models applied to standard earthquake catalogs.

Two such catalogs are plotted on the left side of the detection diagrams. The thin horizontal bars give the origin times and sizes of all earthquakes listed in the ISC catalog having magnitudes greater than 5.0, where the ISC magnitude is here defined as m_b or M_S, whichever is larger. The solid circles are earthquake centroid times and magnitudes taken from the Harvard CMT catalog; in this case, magnitude is computed from the CMT moment according to (16). For the 2-year period under consideration, *Dziewonski et al.* [1987a,b] list CMT solutions for 1032 events ranging in size from $M_0 = 2.0 \times 10^{16}$ ($M_w = 4.8$) to $M_0 = 6.4 \times 10^{20}$ ($M_w = 7.8$).

Association of mode excitations with earthquakes

To allow for a systematic comparison, we employ a simple algorithm for associating events detected by our method with CMT-cataloged earthquakes. In this preliminary paper, we adopt a very conservative definition of a mode-excitation event: we register the beginning of such an event when K_i rises above its 99.9% confidence level, and we terminate the event when it falls below this level for at least two consecutive 3-hour periods. Because we shift each mode window by τ_i, the time needed to align its peak response at the fiducial time t_i (Table 1), the maximum level of excitation should, in principle, occur within a sample or so of the event's centroid time. In practice, this shift can be considerably greater than ±3 hours, owing to the effects of signals from other earthquakes and data gaps. The data gaps following large earthquakes can be substantial, since the response of the IDA instruments to the large-amplitude signals in the early arriving portions of the wave trains is typically nonlinear and must be edited out. Such a gap will bias the excitation peak to a value of t_i that is greater than the centroid time. To allow for these peak shifts, we attribute each distinct mode-excitation event to the largest earthquake in the CMT catalog occurring in the time interval from 12 hours before to 8 hours after the peak excitation level. When there is no CMT event, we search the ISC catalog for earthquakes having m_b or $M_S \geq 5.4$. If no such earthquakes are found and it cannot be attributed to fluctuations in the extended coda following large earthquakes, then the mode-excitation event is designated as "unassociated," and it is flagged by its date and a question mark on the detection diagram. Twenty-seven unassociated mode-excitation events have been identified by this procedure, and they are discussed below.

Fig. 14 (opposite). A detection diagram for a 30-day sample of moderate seismic activity. There are seven mode-excitation events significant at the 99.9% confidence level, all associated with moderate-sized earthquakes in the CMT catalog. There are no unassociated mode-excitation events in this 30-day sample that are significant at the 99.9% level, and there is only one peak significant at the 99% level that does not fall within the association interval of any CMT event, at day 154, 0300. However, a couple of spurious excitation peaks can be expected to occur at this confidence level during a typical month, and we therefore dismiss these apparent mode-excitation events as insignificant.

Our association algorithm assigns every CMT earthquake to one of three catagories, each having its own plotting symbol: (1) "detected earthquakes" (large dots) are those associated with excitation events significant at the 99.9% level; (2) "undetectable earthquakes" (small unmarked dots) are those that cannot be associated because of their proximity to an excitation event already assigned to a larger CMT earthquake; and (3) "undetected earthquakes" (small dots marked by a cross) are those that show no excitation event within the search window.

A typical 30-day example

In the 30-day interval displayed in Figure 14, there are seven mode-excitation events significant at the 99.9% confidence level, all associated with moderate-sized earthquakes in the CMT catalog. The largest is an intermediate-focus earthquake in the New Hebrides ($M_w = 6.8$, $M_0 = 2.0 \times 10^{19}$ N m) occurring on May 13, 1978 at 0708:59 UT. To allow a correspondence with the day of year numbers registered on the detection diagrams, we express this origin time as day 133, 0708:59. The smallest is a shallow-focus earthquake in the Admiralty Islands at day 153, 1130:09 ($M_w = 5.8$, $M_0 = 6.0 \times 10^{17}$ N m). Only four earthquakes having $M_w \geq 6.0$ are not directly associated with mode excitations significant at the 99.9% confidence level. Two of them, a Halmahera event at day 143, 0601:06 and a Volcano Islands event at day 147, 1017:21, both with $M_w = 6.0$, occur near other, larger events; hence their modal excitations cannot be resolved as isolated peaks, and they are assigned to category 2. The other two are shallow-focus earthquakes near the Andreanof Islands (day 131, 0023:38, $M_w = 6.2$) and Bouvet Islands (day 142 1552:33, $M_w = 6.1$); although they fall below our conservative detection threshold and are thus assigned to category 3, they do have well-defined excitation peaks, significant at the 99% level.

The 9-day interval day 134 to day 142 is exceptionally quiet, both in terms of seismicity and modal activity. Only six of the 71 K_i samples peak above the 95% confidence level and only one exceeds the 99% level. The latter, at day 134, 0900, may be associated with a small earthquake near the Balleny Islands whose CMT magnitude is significantly greater than its surface-wave magnitude ($M_w = 5.8$ versus $M_S = 5.2$) and may therefore be a slow event. Overall, however, the mode-excitation statistics in this interval are consistent with random noise. The existence of such quiet periods lends credence to the statistics and our ability to distinguish true mode-excitation events from random noise at high significance levels.

In fact, there are no unassociated mode-excitation events in this 30-day sample that are significant at the 99.9% level, and there is only one α'' peak significant at the 99% level, at day 154, 0300, that does not fall within the association interval of any CMT event. An inspection of the ISC catalog reveals that it occurred at the same time as a small, deep-focus earthquake in southern Tonga ($m_b = 5.1$, $h = 634$ km, $t_0 =$ day 154, 0254:32). A spurious excitation peak can be expected to occur at the 99% confidence level during a typical month, however, and the fortuitous association of such a peak with low-level seismicity will not be uncommon. Hence we assign no significance to it.

Detection threshold

Because the CMT catalog is essentially complete for ordinary earthquakes larger than $M_w = 6.0$, we can use it to measure a detection threshold for the mode-excitation algorithm. This empirical determination can then be compared with the theoretical value as a further check on our statistical assumptions. The detection threshold is defined to be the expected value of the snr, R_d'', at which the Type-II error rate β'' equals 0.5 for a specified Type-I error rate α'', which is fixed in these experiments at 0.001 (see Figure 4). Averaging over source locations and mechanisms allows us to equate R_d'' to an event magnitude M_d''. Therefore M_d'' is the magnitude threshold at which 50% of all detectable earthquakes are identified at the 99.9% confidence level. "Detectable earthquakes" are events sufficiently isolated from other, larger events to associate with distinct mode-excitation peaks, namely, the union of categories 1 and 3 defined previously.

The top panel of Figure 15 compares a histogram of the detectable CMT earthquakes with that of events actually detected by our algorithm, and the bottom panel plots the ratio of these two histograms. The detection ratio is 100% down to $M_w = 6.4$, then drops smoothly to the threshold mark of 50% at 5.95. Hence the empirical determination of M_d'' for 1978-1979 is within a fraction of a magnitude unit of the ideal theoretical value of 5.9, derived from Figure 4, and the Monte Carlo value of 6.0, determined from the simulations exemplified in Figure 13. This agreement increases our confidence in the statistical model.

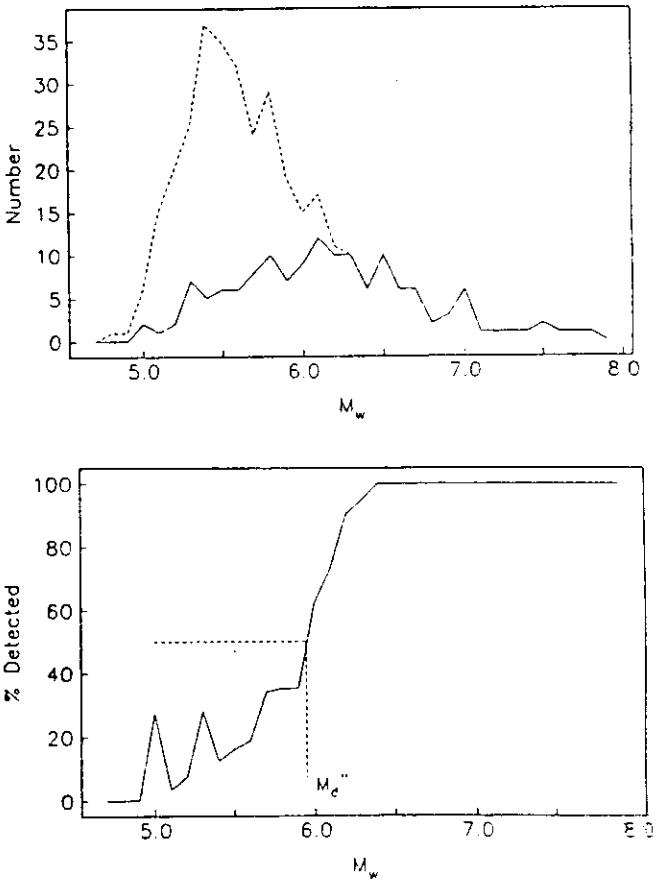

Fig. 15. The top panel shows the number of detectable events in the CMT catalog (dashed line) and the number of CMT events detected by our method (solid line) as a function of M_w for the 2-year period 1978-1979. Detectable events are defined as those events that are well enough separated from other events in the CMT catalog that they are separately detectable using our technique. The bottom panel shows the percentage of detectable events that were detected. The largest undetected event is $M_w = 6.4$. The observed detectability threshold, where 50% of the detectable events are detected, is $M_d'' = 5.95$.

Excitation anomalies associated with slow earthquakes

An examination of the detection diagrams in Appendix B reveals large qualitative differences in the mode-excitation statistics observed for earthquakes of comparable CMT magnitude. Some of these are caused by network variations (detection levels are reduced by fewer stations reporting, larger data gaps, increased noise levels, etc.), and some are due to source location and mechanism type (e.g., shallow-angle thrusts near the free surface excite modes less efficiently than deeper events; the fortuitous placement of several stations on a radiation node can reduce signal levels). However, many of the differences can be attributed to variations in the source time functions. In particular, because the CMT source parameters are determined at frequencies higher than 5 mHz, slow earthquakes will generally excite low-frequency modes more efficiently than fast ruptures of comparable CMT magnitude.

An example of this behavior is shown in Figure 16, which compares the excitation statistics for a sequence of three deep-focus Banda Sea earthquakes which occurred during a 33-min period on February 21, 1978 (day 52 0747:31) with those of a shallow-focus East Honshu event on the previous day. Although the largest of the Banda Sea events had a smaller CMT magnitude than the Honshu event (6.2 versus 6.5), the sequence was a much stronger excitor of low-degree modes. This behavior is consistent with the strong roll-off in the total-moment spectrum observed for the Banda Sea sequence by *Silver and Jordan* [1983]. Using a novel technique for estimating the total-moment spectrum from free-oscillation data [*Silver and Jordan*, 1982], they found that this event had a characteristic duration of $\tau_c = 54 \pm 3$ s, which is anomalously long relative to its total moment of $M_T^0 = (1.9 \pm 0.1) \times 10^{19}$ N m, and they identified it as a slow earthquake. Scaling the characteristic length L_c as the cube root of M_T^0 according to the empirical calibration of *Kanamori and Given* [1981] yields a characteristic velocity of $v_c \approx 0.9$ km/s (Figure 1).

To search for other slow earthquakes during the 2-year interval spanned by our analysis, we employ the network-excitation statistic K_i, defined in equation (6). For each fiducial time t_i, K_i is the total number of modes detected by stations in the network at $(1-\alpha)$% confidence level, an integer that ranges from zero to a maximum value N_i given by equation (7). As discussed in previous sections, we have calculated the distribution law for K_i as the sum over a Markov process, and its significance level α'' has been used in the detection diagrams to assess when an event has occurred. Hence a natural measure of the size of an excitation event is the ratio

$$E_i = K_i / N_i \tag{17}$$

Figure 17 is a plot of E_i versus M_w for all earthquakes associated with highly significant ($\alpha'' \leq 0.1\%$) mode-excitation events during 1978-1979. Because the test for individual mode excitation at individual stations is done with $\alpha = 0.5$, the expected value

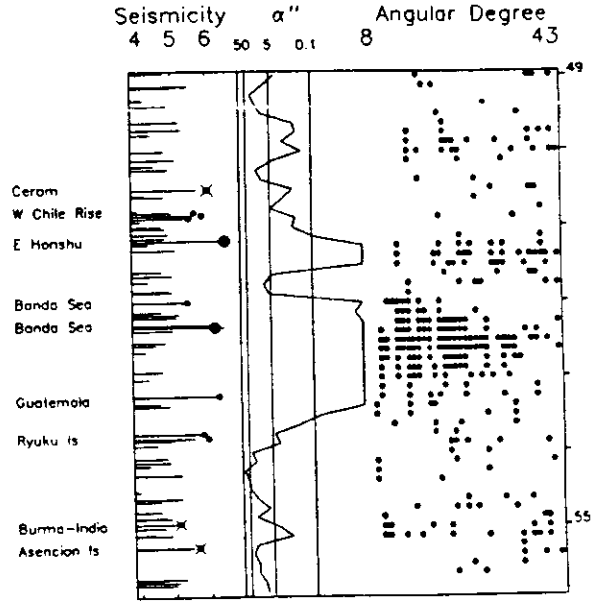

Fig. 16. An enlarged section of a detection diagram for a 6-day period surrounding the February 21, 1978, Banda Sea sequence. The Banda Sea event is an example of a slow earthquake. The East Honshu event, which occurred 1 day before the Banda Sea event, did not excite nearly as many modes. The Banda Sea event had a characteristic time of 54 ± 3 s and a total seismic moment of $1.9 \pm 0.1 \times 10^{19}$ N m, consistent with a low characteristic velocity of less than 1 km/s.

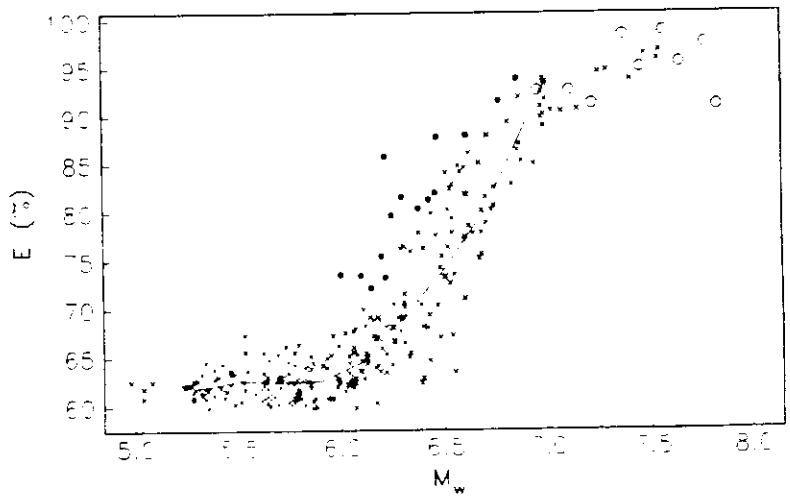

Fig. 17. Values of E_i for all excitation events attributable to events in the CMT catalog versus M_w. The median of the distribution is shown as a solid line. We selected 14 events that differ substantially from the median for further analysis on the suspicion that they are slow events. Parameters for these events are listed in Table 2. Events shown with an open circle are all other events during the 2-year time period that were analyzed by *Silver and Jordan* [1983].

TABLE 2. Analyzed Events

Event	Location	m_b	M_S	M_W*	CMT M_0, 10^{18} N m†	M_T^0, 10^{18} Nm	τ_c, s
2/21/78	Banda Sea	5.6	6.5	6.8	-	19. ± 1.0‡	54 ± 3‡
3/20/78	Mid-Atlantic Ridge	5.7	5.8	6.2	2.4	2.5 ± 0.3	20 ± 9
8/21/78	Prince Edward Islands	5.8	6.2	6.5	5.5	5.8 ± 0.7	28 ± 6
12/14/78	Molucca Passage	6.0	5.8	6.3	1.9	-	-
12/25/78	East-Pacific Rise	5.7	6.5	6.7	9.3	11. ± 1.0	28 ± 4
2/18/79	Prince Edward Islands	5.4	5.9	6.4	4.9	5.2 ± 0.5	18 ± 9
4/23/79	Macquarie Islands	5.5	6.0	6.4	3.1	-	-
5/25/79	Fox Islands	6.0	6.3	-	2.7	-	-
6/10/79	Mid-Atlantic Ridge	5.8	6.0	6.3	1.6	3.1 ± 0.4	26 ± 7
6/27/79	South of Panama	5.8	6.2	6.4	4.2	4.8 ± 0.4	36 ± 3
7/01/79	Panama-Costa Rica	5.3	6.4	6.2	2.3	-	-
8/24/79	Costa Rica	6.1	6.4	6.4	5.8	4.9 ± 0.4	21 ± 6
8/25/79	North-Atlantic Ridge	6.0	6.6	6.8	15.9	16. ± 1.0	34 ± 3
9/29/79	North Sumatra	6.2	6.8	6.9	22.1	2.8 ± 1.0	29 ± 3
12/03/79	Eltanin	4.9	6.0	6.4	-	4.0 ± 0.4	42 ± 4

* Calculated from the total scalar moment if available, otherwise from the CMT moment.
† *Dziewonski et al.* [1987a,b].
‡ *Silver and Jordan* [1983].

of the excitation ratio for random noise is 50%. For the 10-station IDA network, N_i is less than or equal to 360, and it can be calculated that K_i must be greater than 213 for an excitation to register as significant at the 99.9% confidence level. This critical value corresponds to $E_i \geq 59.2\%$. The excitation ratios plotted on Figure 17 generally increase with M_w, ranging from a low of 59.8% for a small, intermediate-focus earthquake in Tonga (1978, day 318, 0512:34; $M_w = 5.3$) to a high of 98.8% for the large, shallow-focus Tumaco, Columbia, earthquake (1979, day 346, 0759:04; $M_w = 7.6$).

Because slow earthquakes are exceptionally good mode excitors, they will generally lie on the high side of the E_i-M_w field defined by the events in Figure 17. The Banda Sea earthquake has the most anomalous position on this diagram of any examined in this study; its excitation ratio of 86% is appreciably greater than the median value of 67% observed for other earthquakes with the same magnitude.

Fourteen additional events that were selected from Figure 17 on the basis of their anomalously high excitation ratios are listed in Table 2. For each of these earthquakes, we attempted to derive moment tensors using the phase-equalization and inversion algorithm of *Riedesel and Jordan* [1989] and, based on these moment tensor estimates, to estimate the total scalar moment M_T^0 and characteristic duration τ_c using the total-moment spectrum technique of *Silver and Jordan* [1983]. (The complete procedure is discussed by *Riedesel et al.* [1986].) We rejected the results for two of the earthquakes, the April 23, 1979, Macquarie Islands event and the May 25, 1979 Fox Islands event, because their total-moment spectra were corrupted by the interference of events of similar size occurring within several hours of their origin times. We also discarded the total-moment spectra of the December 14, 1978, Molucca Passage event and the July 1, 1979, Panama-Costa Rica border event, because they were too small to yield reliable estimates. In Figure 18 we plot τ_c versus M_T^0 for the remaining 10, together with estimates for the Banda Sea earthquake and nine larger events occurring during the study period that were analyzed by *Silver and Jordan* [1983].

All of the anomalous earthquakes have characteristic velocities below 3 km/s, and three have characteristic velocities below 1 km/s. The Banda Sea event is one of the latter, and the other two are on oceanic strike-slip faults (the Panama Transform fault event of June 27, 1979, and the Eltanin Transform fault event of December 3, 1979). Six of the remaining eight anomalous events also occurred on oceanic transform faults (two near the Prince Edward Islands, two on the central Mid-Atlantic Ridge, and one each on the North Atlantic Ridge and the East Pacific Rise).

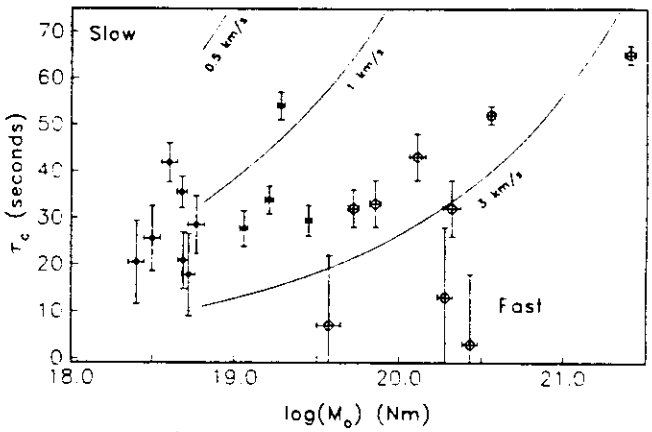

Fig. 18. The 10 events listed in Table 2, for which we obtained total-moment spectra are shown on a τ_c versus M_0 diagram with a solid circle. Also shown with a solid dot is the Banda Sea event analyzed by *Silver and Jordan* [1983]. Other events analyzed by *Silver and Jordan* [1983] that occurred during this period are shown with open circles. Also shown is an empirical relation [*Kanamori and Given*, 1981] between τ_c versus M_0 used here to distinguish between slow and fast earthquakes. We have scaled this relation to determine an approximate characteristic rupture velocity for these events. All of the events that were large enough to be analyzed are as slow or slower than the typical large events studied by *Silver and Jordan* [1983]. Several of them have characteristic velocities of less than 1 km/s.

The association of slow earthquakes with oceanic transform faults has been previously documented. *Kanamori and Stewart* [1976] found that events on the Gibbs Fracture Zone had anomalously large values of M_S relative to m_b and that the seismic moment was larger than one would expect based on an empirical relationship between surface-wave magnitude and the seismic moment. *Okal and Stewart* [1982], *Stewart and Okal* [1983], and *Prozerov and Sabina* [1984] identified slow earthquakes along other oceanic transforms. As these authors have emphasized, this behavior is plausibly explained by the more ductile nature of the hot crust and upper mantle in regions of newly formed oceanic

TABLE 3. Excitation Anomalies

Date	Time, UT	α'', %	K_i	N_i	E_i, %
2/01/78	0900	0.098	174	288	60.4
4/01/78	1500	0.086	166	272	61.0
7/30/78	0300	0.0006	181	288	62.8
8/20/78	0600	0.028	177	288	61.5
10/10/78	0900	0.076	145	235	61.7
12/02/78	1800	0.084	214	360	59.4
12/03/78	0300	0.062	215	360	59.7
12/16/78	1200	0.066	175	288	60.8
12/29/78	2100	0.082	213	357	59.7
12/31/78	0000	0.048	196	324	60.5
12/31/78	1500	0.048	196	324	60.5
1/09/79	0600	0.093	194	324	59.9
2/01/79	2100	0.003	196	309	63.4
2/02/79	1500	0.066	175	288	60.8
4/21/79	2100	0.044	216	359	60.2
5/17/79	2100	0.030	196	322	60.9
6/01/79	0900	0.002	223	360	61.9
6/03/79	1500	0.018	219	360	60.8
6/29/79	0600	0.040	195	323	60.4
7/16/79	1500	0.072	155	252	61.5
7/19/79	1500	0.005	146	228	64.0
7/28/79	0300	0.066	175	288	60.8
7/31/79	1200	0.072	155	252	61.5
8/15/79	0900	0.048	196	324	60.5
9/04/79	0600	0.046	152	245	62.0
9/21/79	0000	0.014	192	311	61.7
10/02/79	1800	0.035	171	278	61.5

lithosphere. The notion that the characteristic velocities of seismic ruptures depend on the effective constitutive parameters in the source region [e.g., *Silver and Jordan*, 1983] is reinforced by our results.

Unassociated excitation anomalies: Silent earthquakes?

Although most mode-excitation events detected at the 99.9% confidence level can be attributed to significant ($M \geq 5.4$) earthquakes in the CMT and ISC catalogs, our algorithm identifies 36 distinct excitation events as "unassociated." Nine occurred adjacent to large earthquakes and can be plausibly dismissed as statistical fluctuations during periods when the background level of excitation is increased due to these sources. The remaining 27 mode-excitation events that cannot be directly attributable to significant earthquakes are listed in Table 3. If there were no seismic mode excitations, we would expect only six false-positive detections (Type-I errors) from the 5840 samples spanning the 2-year study period. In fact, because about half of this interval is occupied by mode excitations due to known earthquakes, only about three false positives should be registered as unassociated events.

Therefore it is likely that at least some, if not most, of the unassociated events in Table 3 are true mode excitations caused by unidentified seismic sources. These could either be slow earthquakes in the ISC catalog having large low-frequency moments but body and surface wave magnitudes that fall below the 5.4 threshold employed by our association algorithm, or perhaps earthquakes with characteristic velocities so low that they radiate insufficient high-frequency energy to detect and locate by standard teleseismic procedures, i.e., "silent earthquakes."

The detection diagrams for three examples of unassociated mode-excitation episodes are illustrated at expanded scales in Figures 19-21. The first, which occurred on July 30, 1978, has two peaks, both of which are significant at the 99.99% confidence level (Figure 19). These peaks lie near the middle of a 66-hour interval that is devoid of CMT events and has no ISC events with magnitudes greater than 5.0.

The second anomalous episode is a triple peak, two occurring

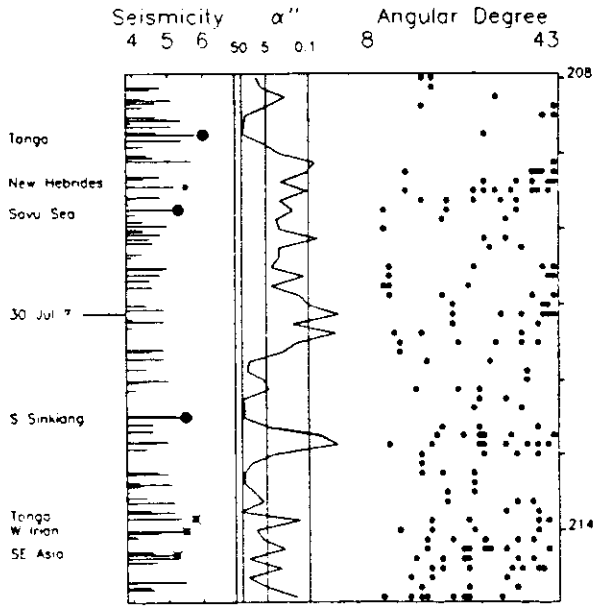

Fig. 19. A detection diagram for a 6-day period surrounding the July 30, 1978, excitation anomaly. The two peaks of the anomaly are separated by only one point below the detection threshold so that they are counted as only one anomaly. The nearest events in the CMT catalog are the Savu Sea and South Sinkiang events. The Savu Sea event is associated with a weak excitation that appears approximately six hours after the event took place, and the South Sinkiang event is associated with a stronger peak that took place about 6 hours after it. ISC-catalog seismicity is plotted down to the magnitude 4.0 level. There are no events large enough to explain the excitation anomaly.

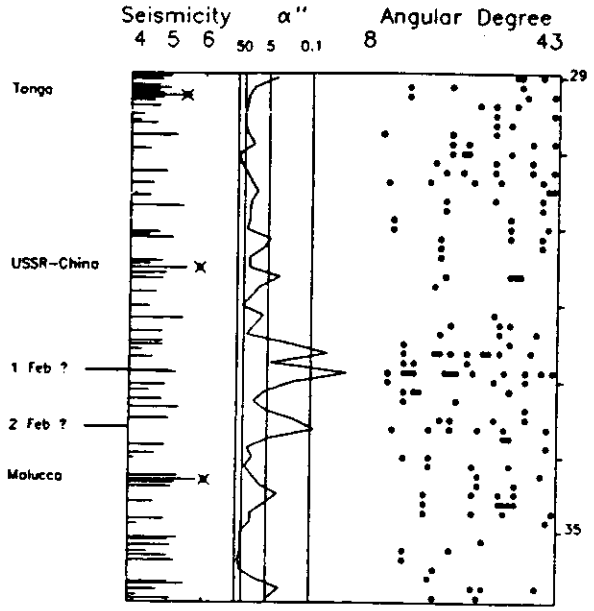

Fig. 20. A detection diagram for a 6-day period surrounding the February 1, 1979, excitation anomaly. This anomaly consists of two peaks both with small values of α'' followed on February 2, 1979, by yet another peak. There is no CMT or ISC earthquake in the vicinity of these peaks large enough to explain them. The closest events in the CMT catalog are a deep-focus event on the USSR-China border and the Molucca Sea event, neither of which are detected.

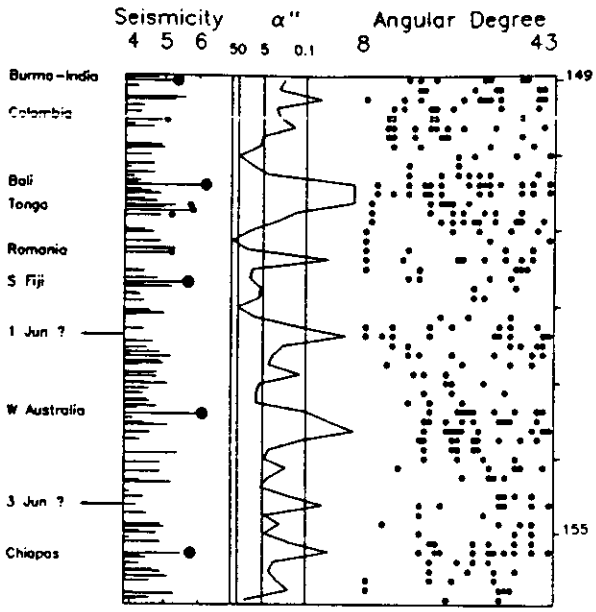

Fig. 21. A detection diagram for a 6-day period surrounding the June 1, 1979, anomaly. This event occurs during a much more seismically active period than the previous two anomalies; however, the anomaly is isolated in time from other earthquakes that have their own excitation peaks, and is significant at a very high confidence level. Another, less pronounced anomaly occurs on June 3, 1979.

on February 1, 1979, and a third on February 2, 1979 (Figure 20). All three have K_i statistics significant at the 99.9% level, and the middle one is significant at the 99.99% level. This sequence is particularly impressive because the seismicity and background noise levels are exceptionally low and each of the peaks in α'' is associated with a clearly evident "run" of fundamental spheroidal modes individually excited at the 90% confidence level. The closest events in the CMT catalog are a deep-focus earthquake on USSR-China border 25 hours before the first peak (January 31, 1979, $M_w = 5.9$) and a Molucca Passage event 17 hours after the third (February 3, 1979, $M_w = 6.1$). We note that neither of these earthquakes was large enough to register an excitation peak significant at even the 99% level.

The third example (Figure 21) shows a single, strong, unassociated excitation peak on June 1, 1979 and a somewhat weaker unassociated peak on June 3, 1979. The first is comparable in amplitude to the excitation peak registered by the M_w=6.1 Western Australia earthquake which occurred between the two unassociated peaks.

We examined the time series recorded at stations of the IDA network during the unassociated excitation episodes presented in Figures 19-21. No seismic signals were obvious. Since our algorithm is capable of detecting events whose signal-to-noise ratio on individual records is less than unity, these null observations are not inconsistent with a seismic origin of the unassociated mode-excitation events. If they are the manifestations of unidentified earthquakes, however, the rupture processes which produced them must be anomalously quiet, and their source spectra must roll-off rapidly at frequencies higher than the 5-mHz cutoff used in this study. Documenting the locations and source properties of these hypothetical, unusually slow ruptures will be one goal of our future research.

DISCUSSION AND CONCLUSIONS

Near-field noise is continuously distributed over a broad frequency band, whereas far-field radiation is concentrated in the discrete, narrow resonances of the Earth's normal-mode spectrum. Knowledge of Earth structure can thus be used to detect the low-level excitation of free oscillations without assuming any knowledge of source processes. We have implemented this simple idea in an algorithm to identify episodes of fundamental spheroidal mode excitation and to associate them with known earthquakes. This concluding section summarizes the results of our preliminary study, discusses ways to improve and generalize the detection scheme, and points to directions that could be explored in future research.

The detection algorithm

Our detector is a robust, two-stage statistical test whose false-positive and false-negative error rates have been precisely characterized by theoretical calculations and numerical experiments. In the first stage of the detection algorithm, the ratio of the energy in a particular mode band to the energy in adjacent noise bands, the variable γ^2 defined by equation (3), is tested for significance at the 50% confidence level, a calculation which requires integrating the Fourier spectrum over narrow frequency windows. By recasting the frequency-domain integrals as time-domain integrals (equation (8)), we have been able to reduce the computational effort and tailor the time series to optimize the signal-to-noise ratios of the individual spheroidal modes.

The second stage of the detection algorithm combines the first-stage results from various stations of a global network to test the null hypothesis that the energy distribution is due to noise against the alternative that a genuine mode-excitation event has occurred. The confidence level for the second-stage test is set much higher

than the first-stage test, usually at 99.9%, so that its false-positive error rate will be small. To assess the overall performance of the detector, we have introduced the concept of a detection threshold, specified to be the event magnitude at which the false-negative error rate is 50% for a false-positive error rate of 99.9%. We have shown (Appendix A) that the 50% confidence level used to flag individual mode excitations at individual stations in the first-stage test is close to the value that minimizes the detection threshold for the second-stage test.

Theoretical calculations and numerical experiments with both real and simulated data sets have indicated that fundamental spheroidal modes recorded at frequencies less than 5 mHz by a sparse (~10-station) network of vertical-component seismometers can achieve a magnitude detection threshold of $M_w \approx 6.0$, corresponding to a seismic moment of $\sim 1 \times 10^{18}$ N m. The spheroidal modes excited by an event of this magnitude have signal-to-noise ratios that are less than unity, so it is possible to detect mode-excitation events that are not obvious from a visual inspection of individual records.

Results from the IDA network

The detector has been applied at 3-hour intervals to the fundamental spheroidal modes ${}_0S_2$-${}_0S_{43}$ recorded during 1978 and 1979 by the IDA network. The detection diagrams for the full 2-year interval are displayed in Appendix B. The mode-excitation levels associated with earthquakes of a given magnitude are highly variable. Some of this variation is due to source and network geometry, but much of it appears to reflect differences in source time functions. In particular, slow earthquakes are observed to be associated with anomalously high levels of mode excitation. A plot of mode-excitation ratio against moment-magnitude (Figure 17) has been used to identify anomalous events, and those with high excitation ratios tend to have anomalously long characteristic durations (Figure 18). Most of these slow earthquakes occur on oceanic transform faults.

The majority of the mode-excitation events detected at the 99.9% confidence level can be associated with earthquakes of significant size (m_b, M_S, or $M_w \geq 5.4$) in the CMT and ISC catalogs. However, we have identified 27 mode-excitation events that are not, far more than are accounted for by random fluctuations in the ambient noise background. These unassociated events are most plausibly explained as earthquakes whose zero-frequency moments are large ($>10^{17}$ N m) but whose characteristic velocities are sufficiently low that their high-frequency magnitudes fall below the 5.4 threshold employed in our association algorithm. We are intrigued by the possibility that a few might even be "silent earthquakes" whose high-frequency radiation is too weak to be detected and located by the ISC network.

Directions for future research

The 2-year sample of IDA recordings analyzed in this preliminary study is only a small fraction of high-quality digital data now available from a growing set of low-frequency seismometer installations operated by various research groups and national agencies. For example, very-long-period stations of the French GEOSCOPE network, which currently number 20, have been recording data in the free-oscillation band since 1982 [*Romanowicz et al.*, 1984], and a new network of broad-band, high-dynamic-range stations sponsored by a group of U.S. universities, the Incorporated Research Institutions for Seismology (IRIS), is being deployed [*Smith*, 1986]. Applying our detection scheme to this entire global network should reduce the detection threshold and increase our sample of anomalous events. Because the algorithm has been automated for continuous input of a global network data stream, it should be feasible to obtain a complete catalog of mode-excitation events spanning more than a decade with relatively little effort. The properties of anomalies identified from this catalog can then be systematically studied using event-specific low-frequency techniques, such as those discussed by *Silver and Jordan* [1982, 1983] and *Riedesel and Jordan* [1989], as well as by more standard high-frequency methods.

Several improvements and variations in our detection algorithm readily suggest themselves. As previously discussed, we have paid no attention to variations in the signal-to-noise ratio from mode to mode and station to station, other than to exclude particularly noisy frequencies (e.g., those less than 1.4 mHz) and stations (e.g., RAR). A more sensible weighting scheme could be formulated. Our algorithm also considers only fundamental spheroidal modes and ignores the existence of spheroidal overtones. We could take better account of the structure of the free-oscillation spectrum.

The algorithm could be easily generalized to use other free oscillations. Because of the lower signal-to-noise ratios of horizontal-component seismographs and the lower Q of shear-dominated modes, the toroidal free oscillations are probably of limited use. However, it would be interesting to examine variations in the excitation levels of the high-Q radial modes, which are more sensitive to sources with slow isotropic components. Episodes of volumetric compression driven by phase changes in, say, the mid-mantle transition zone could provide such sources [*Benioff*, 1963; *Dziewonski and Gilbert*, 1974]. Our current algorithm takes into account only the amplitudes of the free oscillations, but it could be easily adapted to matched-filtering schemes that make use of the phase information on the seismogram. An algorithm tuned to sources with specific locations and/or mechanisms could substantially reduce the detection threshold of mode-excitation events.

The approach taken in this paper is to identify a specific mode-excitation anomaly and associate it with a specific earthquake. However the mode-excitation statistics displayed on the detection diagrams of Appendix B are themselves complicated time series whose variations must be correlated in a more sophisticated way with the earthquake time series derived from standard seismicity catalogs. For example, we have not attempted to answer the question of how often the occurrence of small, ordinary earthquakes in disparate regions of the globe, say, those of magnitude less than 5.4, might conspire to excite free oscillations to amplitudes sufficient to bias our detection statistics. We also have not evaluated whether free oscillations can be significantly excited by nonseismic sources, such as the rapid motions of large atmospheric disturbances across large lakes or continental margins. These questions should be answered before too much stock is put in silent earthquakes as an hypothesis for explaining unassociated excitation anomalies of the sort illustrated in Figures 19-21.

Towards a physical understanding of episodic strain release

The primary motivation for undertaking this investigation has been to develop new methods for identifying and cataloging the mechanisms of low-frequency seismic moment release that are complementary to standard high-frequency earthquake studies. Although seismological research on slow-earthquake phenomena

has been vigorous for over 10 years, the full variety of strain release mechanisms with characteristic velocities in the range from 10 m/s to 1 km/s has not yet been assessed (cf. Figure 1). A number of physical mechanisms have been postulated to explain the stabilization of slip at low rupture velocities, including strain-weakening effects [*Dieterich*, 1979; *Das and Scholz*, 1981], strain-hardening effects [*Rice and Cleary*, 1976; *Rice and Simons*, 1976; *Tse and Rice*, 1986; *Rudnicki and Chen*, 1988], viscoelastic mechanisms [*Yamashita*, 1980; *Bonafede et al.*, 1983], and ductile instabilities [*Hobbs et al.*, 1986]. Nondislocation sources having low characteristic velocities, such as phase changes [*Benioff*, 1963; *Dziewonski and Gilbert*, 1974] and the large-scale slumping of soft sediments or landslides [*Kanamori*, 1988; *Kawakatsu*, 1989], may also be seismologically significant.

Low-frequency studies have a particularly important bearing on the question of how earthquakes nucleate and, therefore, on the problems of earthquake prediction. Laboratory experiments have shown that stable aseismic slip precedes unstable stick-slip [*Scholz et al.*, 1972]. *Dieterich* [1978] has found that in addition to this slow aseismic slip, there is a second stage of more rapid slip occurring immediately prior to failure. Laboratory measurements of this deformation yield propagation velocities in the range 20-200 m/s, within the field of slow and silent earthquakes shown in Figure 1. If the region of nucleation is sufficiently large, creep acceleration precursory to brittle failure might excite low frequency waves tens of seconds prior to the high-frequency origin time of the earthquake. Some observations of moment-release spectra at normal-mode frequencies reported by *Jordan et al.* [1988] support this hypothesis. Silent earthquakes might occur as accelerated creep events that do not induce brittle rupture. It is hoped that the catalogs developed from the research begun in this paper will contribute to a better understanding of earthquake nucleation phenomena.

APPENDIX A: POWER OF THE STATISTICAL TESTS

There are two possible erroneous decisions in hypothesis testing: (1) Type-I error (false rejection of the null hypothesis) is to register a positive detection when no excitation occurs and (2) Type-II error (false acceptance of the null hypothesis) is to register a negative detection when an excitation does occur. Of the two, Type-I errors are considered the more serious since they require the rejection of a generally accepted hypothesis. Thus in hypothesis testing it is standard practice to fix $\alpha = P(H_1 \mid H_0)$ at a low level and design a test for which $\beta = P(H_0 \mid H_1)$ is as small as possible. This is equivalent to maximizing the power of the statistical test, where the power is defined as $1-\beta$, the probability of correctly rejecting the null hypothesis, H_0. The nontrivial aspect of this approach is to determine the probability, β, of a Type-II error. To accomplish this we use a stochastic model for the behavior of the random variable when H_1 is true.

When H_1 is true we assume that the signal consists of a chi-square distributed random variable scaled by a signal-to-noise ratio (snr) R. We rewrite the numerator, x^2, of equation (3) as

$$x^2 = |\mu_0^n(\omega_i)|^2 + R^2 |\mu_0^s(\omega_i)|^2 \qquad \text{(A1)}$$

where the superscripts n and s denote the contributions to μ_0 due to noise and signal at the normal mode eigenfrequency ω_i. Both $|\mu_0^n|^2$ and $|\mu_0^s|^2$ are assumed to be $\chi^2(2)$ distributed. If the null hypothesis is true, $R = 0$ and x^2 is governed by a χ^2 distribution with 2 degrees of freedom. If the alternative hypothesis is true, x^2 is in general not governed by a χ^2 distribution; however, we can use a χ^2 distribution to approximate its behavior by matching the lower-order moments of x^2 with those of a χ^2 distribution. The resulting detection statistic will be governed by a different F-distribution than when the null hypothesis is true.

If y^2 is a $\chi^2(\nu)$ distributed random variable, then the first and second moments of y^2 are

$$\langle y^2 \rangle = \nu \qquad \text{(A2)}$$

where $\langle y^2 \rangle$ denotes the expected value of y^2, and

$$\langle (y^2 - \langle y^2 \rangle)^2 \rangle = 2\nu \qquad \text{(A3)}$$

We scale the variable x^2 with a constant coefficient λ such that it has the same first and second moments as a χ^2 distribution. Matching the first and second moments of λx^2 with (A2) and (A3) we obtain

$$\lambda = \frac{1 + R^2}{1 + R^4} \qquad \text{(A4)}$$

We treat the variable λx^2 as $\chi^2(\nu)$ distributed, where

$$\nu = \frac{2(1 + R^2)^2}{1 + R^4} \qquad \text{(A5)}$$

Thus, in order to calculate the probability of a Type-II error, we use an $F(\nu,4)$ distribution and evaluate the cumulative left tail for the scaled random variable

$$\left(\frac{1}{1 + R^2}\right) \gamma^2 \qquad \text{(A6)}$$

When H_0 is true the scaling factor in equation (A6) is unity, the detection statistic is $F(2,4)$ distributed, and $\beta = 1-\alpha$. When H_1 is true, as R increases, β decreases rapidly to values much lower than $1-\alpha$ (Figure A1).

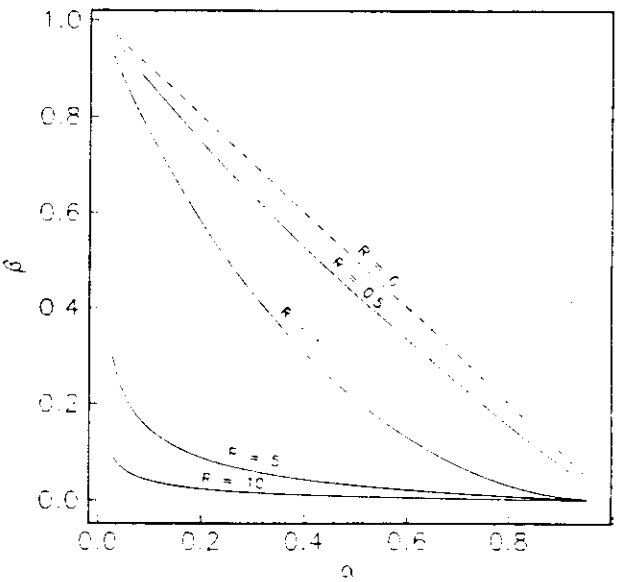

Fig. A1. The probability β of incorrectly accepting the null hypothesis, that the spectral level in the mode band is indistinguishable from the spectral level in the noise band, versus the probability α of incorrectly rejecting the null hypothesis. For signal strengths of $R = 0$, $\beta = 1-\alpha$ (dashed line). Increasing values of R reduce the probability β of making a Type-II error.

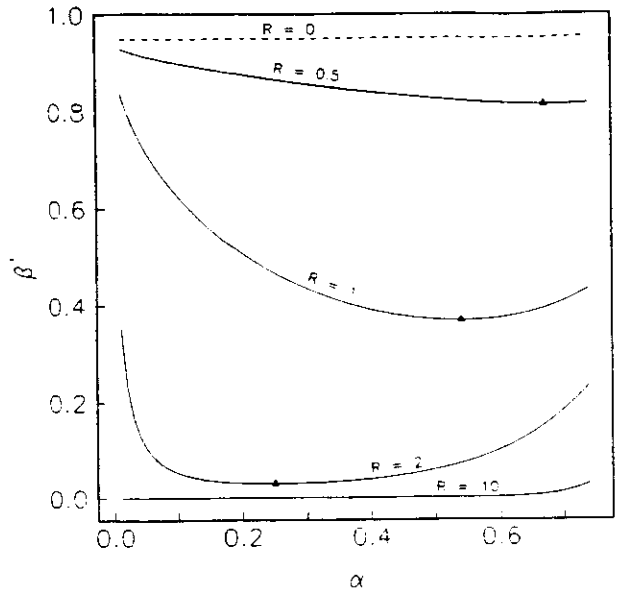

Fig. A2. For a 10-station network the probability of incorrectly rejecting the null hypothesis, that the spectral levels in the mode bands are indistinguishable from the spectral levels in the noise bands, given a confidence level of $\alpha' = 0.1$ versus the probability α of incorrectly rejecting the null hypothesis in the original F test (Figure A1). Again, for signal strengths of $R = 0$, $\beta' = 1-\alpha'$. Increasing values of R reduce the probability of making a Type-II error. For $R = 1$, the probability of making a Type-II error is reduced by a factor of 4.

The power of the F test for the detection of a single mode at a single station is governed by the snr, which we do not control. The power of the binomial tests, β' on J_{it} and β'' on K_i, however, depend on the confidence level α in the original F test. We are free to choose α such that the power is maximized.

The power of the binomial test for the detection of a single mode, tested at significance level $\alpha' = 0.1$, by a 10-station network is shown in Figure A2 for a range of signal strengths. Even at low signal strengths the power of the test with a 10-station network increases from $1-\beta' = 0.1$ for a single station to $1-\beta' = 0.8$. Thus the 10 station network decreases the probability of a Type-II error from 90% to 20%. We can also construct a trade-off curve between the probability of making a Type-I error and the probability of making a Type-II error (α' versus β'). We have done this for a relatively low assumed snr of $R = 1$ (Figure A3). For $R = 1$ the confidence level $\alpha' = 0.1$ results in a reasonably small value of $\beta' = 0.2$. We have adopted this level for plotting the J_{it} statistic.

In the test on K_i for an excitation event over all the modes by the entire network, the sample size is quite large ($N_i = 360$) and the corresponding probability, β'', of making a Type-II error, even for a relatively weak signal, is extremely low. Figure A4 shows the values of β'' versus α for the same values of R as in figure A2. For low values of R the optimal values of α are around 0.5. If we choose a value much below 0.5, we would require nearly all the stations to record nearly all of the modes. To guard against the possibility of a single station corrupting the results we adopt a value of $\alpha = 0.5$ for the test on α''.

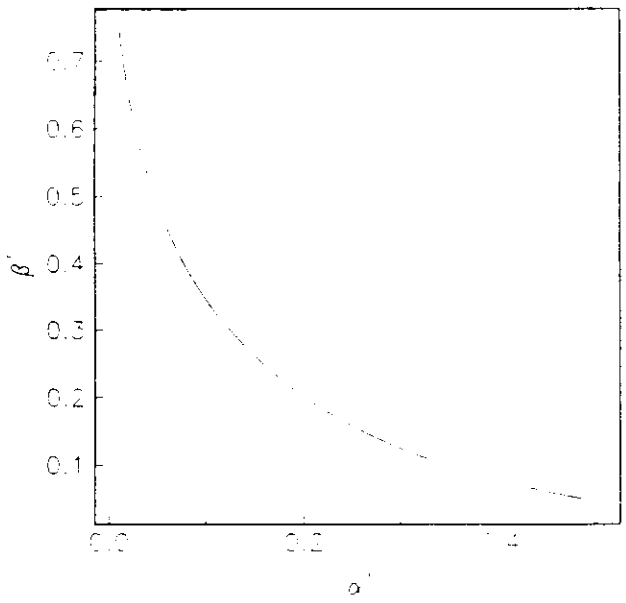

Fig. A3. The trade-off curve for the probability of making a Type-I error α' versus the probability of making a Type-II error β'. Values of α in the original F test were chosen that minimized the probability of Type-II error for the prescribed probability of a Type-I error for $R = 1$. A probability of $\alpha' = 0.1$ results in $\beta' = 0.2$.

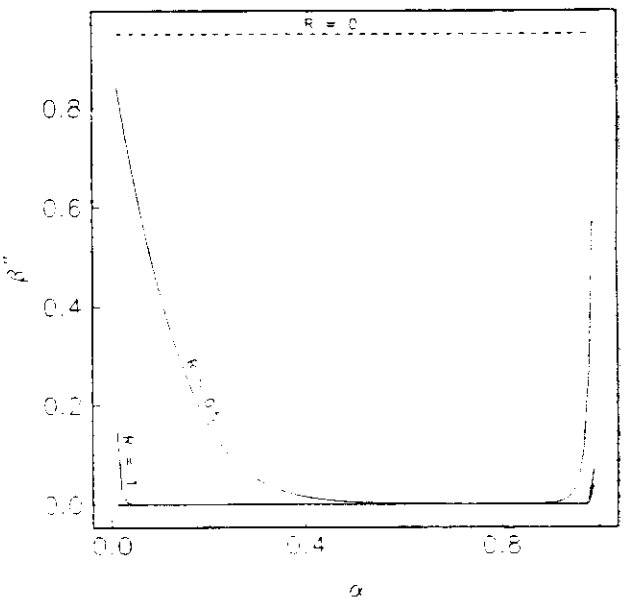

Fig. A4. The same as Figure A2 for the probability α in the original F-test versus the probability of a false negative β'' in the test over all the stations and modes. The optimal α for low snr is at a value of less than 0.5. We use a value of $\alpha = 0.5$ to decrease the sensitivity of the test to a single bad station.

APPENDIX B: DETECTION DIAGRAMS FOR THE PERIOD 1978-1979

Figure B1 shows the detection diagrams for the period 1978-1979. Each section covers a half year period of time in two 3-month panels. Time increases from top to bottom with the day of year printed beside a tick mark every 5 days on the rightmost margins of each panel. A solid circle under the heading "angular degree" denotes a mode detection by the network at the 90% confidence level for the fundamental spheroidal modes $l = 8$-43. The graph in the center of the diagram expresses α'', the Type-I error level of the K_i statistic (equation (6)), as a percentage, so

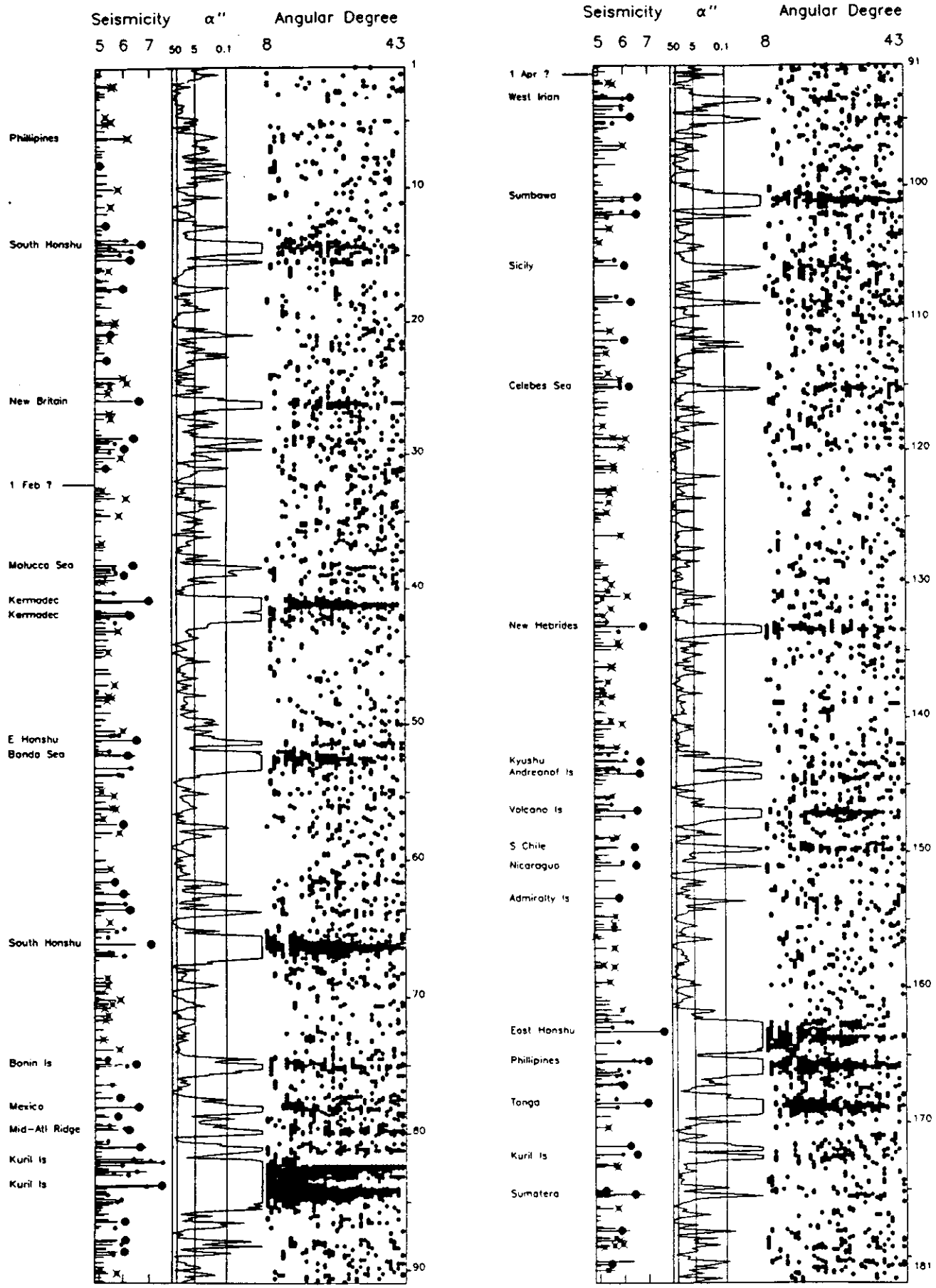

Fig. B1. Detection diagrams for the period 1978-1979.

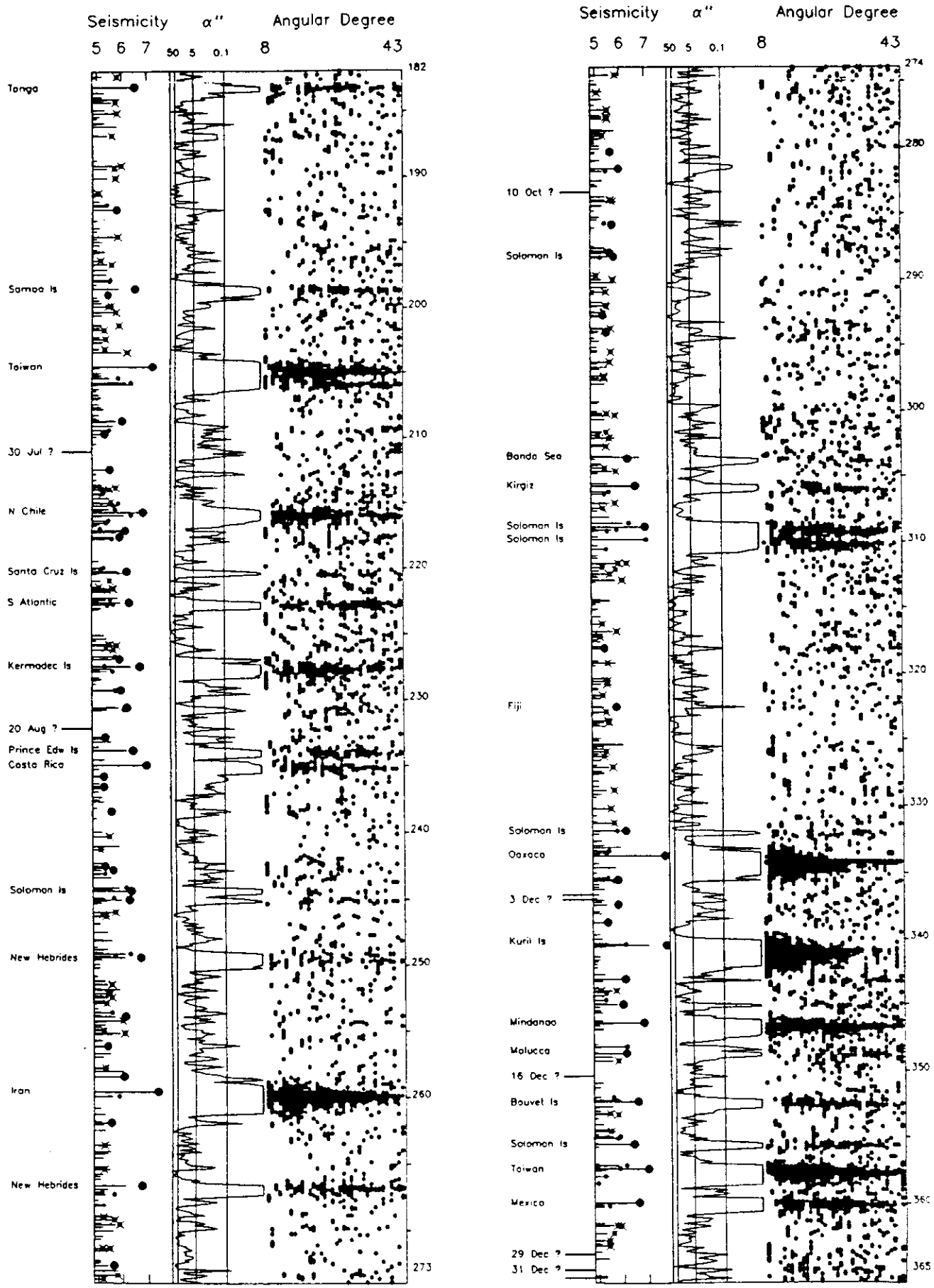

Fig. B1. (continued)

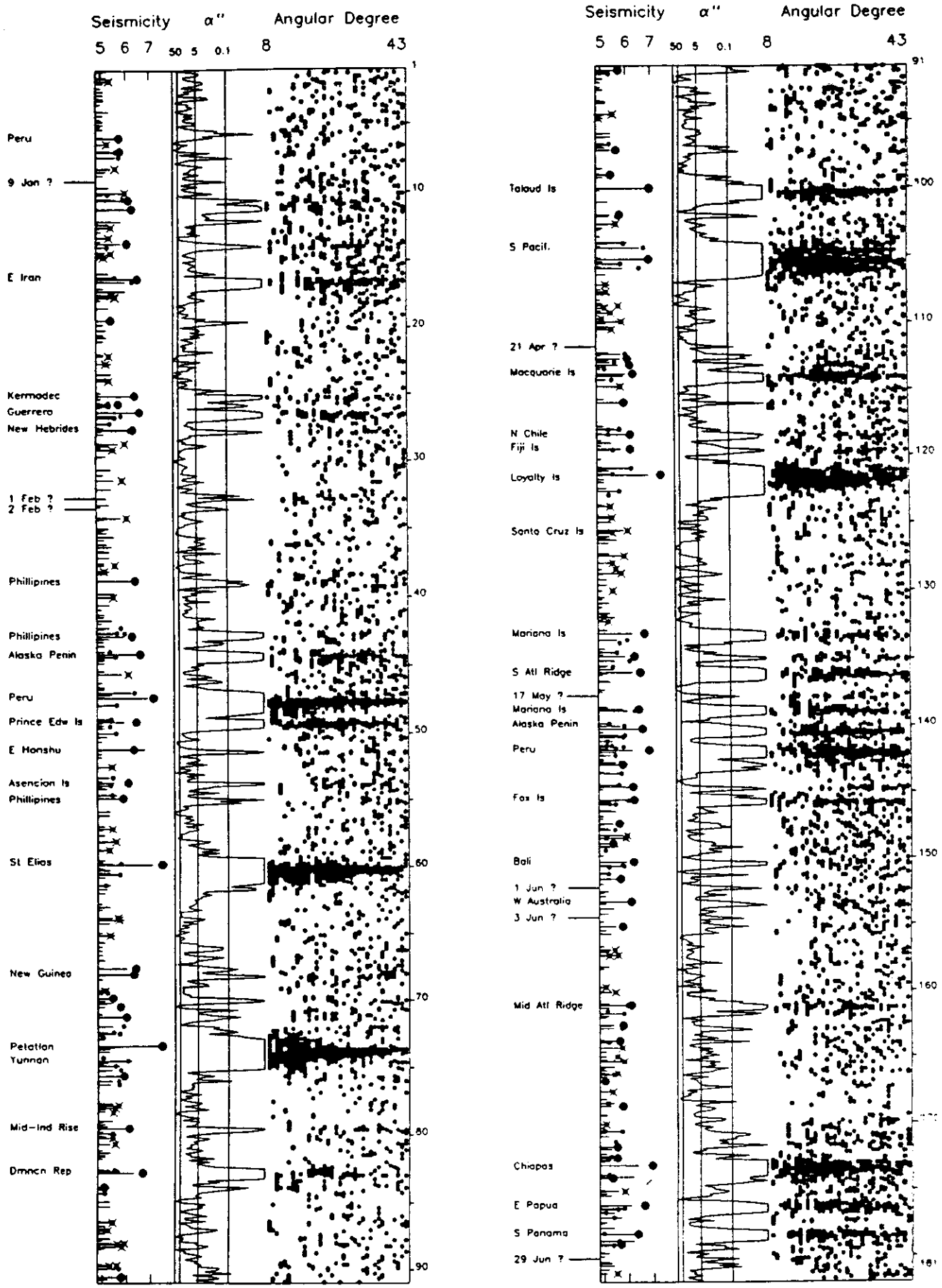

Fig. B1. (continued)

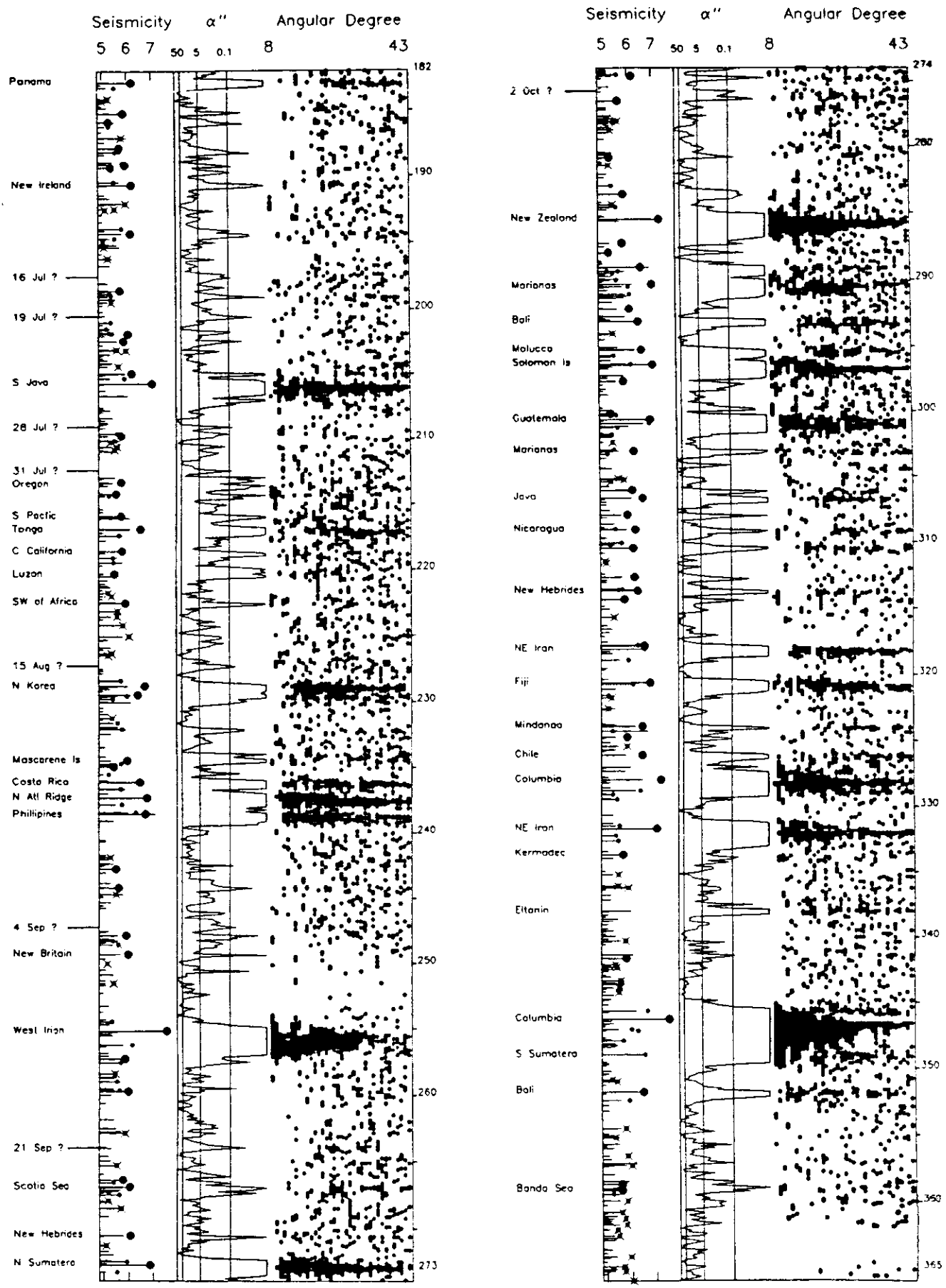

Fig. B1. (continued)

that the vertical line labeled 0.1 represents an event detection at the 99.9% confidence level, which we use to register a detection. Similar lines are shown for the 50% and 95% levels. The probability axis is plotted on an inverse logarithmic scale to emphasize differences at very high confidence levels. During large earthquakes the probability of a Type-I error becomes very small; we clip the probability plot at 0.001%. The leftmost margin of the plot consists of comments for events of interest. For unexplained excitation anomalies the date and a question mark are shown. The part of the diagram under the heading "seismicity" is a plot of seismicity from the ISC and Harvard CMT catalogs. Earthquakes in the ISC catalog with m_b or M_S greater than or equal to 5.0 are shown as lines. Events in the CMT catalog are plotted as discrete symbols by converting the Harvard moment to magnitude using (16). The three different symbols represent three catagories of CMT events: (1) "detected earthquakes" (large dots), those associated with excitation events significant at the 99.9% level; (2) "undetectable earthquakes" (small unmarked dots), those that cannot be associated because of their proximity to an excitation event already assigned to a larger CMT earthquake; and (3) "undetected earthquakes" (small dots marked by crosses), those that show no associated excitation event within the search window.

Acknowledgments. We thank Erika Anderson for help in processing the IDA network data and Anne Sheehan and Mark Riedesel for their help in calculating the moment tensors and total-moment spectra. Guy Masters provided a thoughtful review. Thanks are also due to project IDA personnel for the high-quality data used in this study. This work was supported by the National Science Foundation under grant EAR-88051874.

REFERENCES

Abe, K., Tsunami and mechanism of great earthquakes, *Phys. Earth Planet. Inter.*, *7*, 143-153, 1973.

Agnew, D. C., and J. Berger, Vertical seismic noise at very low frequencies, *J. Geophys. Res.*, *83*, 5420-5424, 1978.

Agnew, D. C., J. Berger, W. E. Farrell, J. F. Gilbert, G. Masters, and D. Miller, Project IDA: A decade in review, *Eos Trans. AGU*, 203-212, 1986.

Backus, G., Interpreting the seismic glut moments of total degree two or less, *Geophys. J. R. Astron. Soc.*, *51*, 1-25, 1977*a*.

Backus, G., Seismic sources with observable glut moments of spatial degree two, *Geophys. J. R. Astron. Soc.*, *51*, 27-45, 1977*b*.

Backus, G., and M. Mulcahy, Moment tensors and other phenomenological descriptions of earthquake sources, I, Continuous displacements, *Geophys. J. R. Astron. Soc.*, *46*, 341-361, 1976*a*.

Backus, G., and M. Mulcahy, Moment tensors and other phenomenological descriptions of earthquake sources, II, Discontinuous displacements, *Geophys. J. R. Astron. Soc.*, *46*, 301-329, 1976*b*.

Benioff, H., Source waveforms of three earthquakes, *Bull. Seismol. Soc. Am.*, *53*, 893-903, 1963.

Benioff, H., and F. Press, Progress report on long period seismographs, *Geophys. J. R. Astron. Soc.*, *1*, 208-215, 1958.

Bonafede, M., E. Boschi, and M. Dragoni, Viscoelastic stress relaxation on deep fault sections as a possible source of very long period elastic waves, *J. Geophys. Res.*, *88*, 2251-2260, 1983.

Dahlen, F. A., The effect of data windows on the estimation of free oscillation parameters, *Geophys. J. R. Astron. Soc.*, *69*, 537-549, 1982.

Dahlen, F. A., and R. V. Sailor, Rotational and elliptical splitting of the free oscillations of the Earth, *Geophys. J. R. Astron. Soc.*, *58*, 609-623, 1979.

Das, S., and C. H. Scholz, Theory of time-dependent rupture in the Earth, *J. Geophys. Res.*, *86*, 6039-6051, 1981.

Dieterich, J. H., Preseismic fault slip and earthquake prediction, *J. Geophys. Res.*, *83*, 3940-3948, 1978.

Dieterich, J. H., Modeling of rock friction, 1, Experimental results and constitutive equations, *J. Geophys. Res.*, *84*, 2161-2168, 1979.

Dziewonski, A. M., T. A. Chou, and J. H. Woodhouse, Determination of earthquake source parameters from waveform data for studies of global and regional seismicity, *J. Geophys. Res.*, *86*, 2825-2852, 1981.

Dziewonski, A. M., G. Ekstrom, J. E. Franzen, and J. H. Woodhouse, Global seismicity of 1978: Centroid-moment tensor solutions for 512 earthquakes, *Phys. Earth Planet. Inter.*, *46*, 316-342, 1987*a*.

Dziewonski, A. M., G. Ekstrom, J. E. Franzen, and J. H. Woodhouse, Global seismicity of 1979: Centroid-moment tensor solutions for 524 earthquakes, *Phys. Earth Planet. Inter.*, *48*, 18-46, 1987*b*.

Dziewonski, A. M., and F. Gilbert, Temporal variation of the seismic moment tensor and evidence of precursive compression for two deep earthquakes, *Nature*, *247*, 185-188, 1974.

Dziewonski, A. M., and J. H. Woodhouse, Studies of the seismic source using normal-mode theory, in *Earthquakes: Observation, Theory, and Interpretation*, pp. 45-137, North-Holland, New York, 1983.

Feller, W., *An Introduction to Probability Theory and Its Applications*, pp. 372-428, John Wiley, New York, 1968.

Gilbert, F., Derivation of source parameters from low-frequency spectra, *Philos. Trans. R. Soc. London, Ser. A*, *274*, 369-371, 1973.

Gilbert, F., and A. M. Dziewonski, An application of normal mode theory to the retrieval of structural parameters and source mechanisms from seismic spectra, *Philos Trans. R. Soc. London, Ser. A*, *278*, 187-269, 1975.

Hanks, T. C., and H. Kanamori, A moment magnitude scale, *J. Geophys. Res.*, *84*, 2348-2350, 1979.

Hobbs, B. E., A. Ord, and C. Teyssier, Earthquakes in the ductile regime?, *Pure Appl. Geophys.*, *124*, 309-336, 1986.

Jordan T. H., A procedure for estimating lateral variations from low-frequency eigenspectra data, *Geophys. J. R. Astron. Soc.*, *52*, 441-455, 1978.

Jordan, T. H., A. F. Sheehan, and M. A. Riedesel, Detecting slow precursors to fast seismic ruptures, *Eos Trans. AGU*, *69*, 1304, 1988.

Kanamori, H., Mechanism of tsunami earthquakes, *Phys. Earth Planet. Inter.*, *6*, 346-359, 1972.

Kanamori, H., Mechanism of low-frequency earthquakes, *Eos Trans. AGU*, *69*, 1303, 1988.

Kanamori, H., and J. W. Given, Use of long-period surface waves for rapid determination of earthquake source parameters, *Phys. Earth Planet. Inter.*, *27*, 8-31, 1981.

Kanamori, H., and G. S. Stewart, Mode of strain release along the Gibbs Fracture-Zone, Mid-Atlantic Ridge, *Phys. Earth Planet. Inter.*, *11*, 312-332, 1976.

Kanamori, H. and G. S. Stewart, A slow earthquake, *Phys. Earth Planet. Inter.*, *18*, 167-175, 1979.

Kasahara, K., Earthquake fault studies in Japan, *Philos. Trans. R. Soc. London, Ser. A*, *274*, 287, 1973.

Kawakatsu, H., Centroid single-force inversion of seismic waves generated by landslides, *J. Geophys. Res.*, *94*, 12,363-12,374, 1989.

King, C-Y., R. D. Nason, and D. Tocher, Kinematics of fault creep, *Philos. Trans. R. Soc. London, Ser. A*, *274*, 355-360, 1973.

Linde, A. T., K. Suyehiro, S. Miura, I. S. Sacks, and A. Takagi, Episodic aseismic earthquake precursors, *Nature*, *334*, 513-515, 1988.

Masters, G., and F. Gilbert, Attenuation in the earth at low frequencies, *Philos. Trans. R. Soc. London, Ser. A*, *308*, 479-522, 1983.

Okal, E. A., and L. M. Stewart, A negative search for an ultra-slow component to the source of the Yunnan earthquakes of May 29, 1976, *Phys. Earth Planet. Inter.*, *26*, 208-216, 1981.

Okal, E. A., and L. M. Stewart, Slow earthquakes along oceanic fracture zones: Evidence for asthenospheric flow away from hotspots?, *Earth Planet. Sci. Lett.*, *57*, 75-87, 1982.

Prozorov, A. G., and F. J. Sabina, Study of properties of seismicity of the Mexico region, *Geophys. J. R. Astron. Soc.*, *76*, 317-336, 1984.

Rice, J. R., and M. P. Cleary, Some basic stress-diffusion solutions for fluid-saturated elastic porous media with compressible constituents, *Rev. Geophys.*, *14(2)*, 227-241, 1976.

Rice, J. R., and D. A. Simons, The stabilization of spreading shear faults by coupled deformation-diffusion effects in fluid-infiltrated porous materials, *J. Geophys. Res.*, *81*, 5322-5334, 1976.

Riedesel, M. A., and T. H. Jordan, Display and assessment of seismic moment tensors, *Bull. Seismol. Soc. Am.*, *79*, 85-100, 1989.

Riedesel, M. A., T. H. Jordan, A. F. Sheehan, and P. G. Silver, Moment-tensor spectra of the 19 Sept 85 and 21 Sept 85 Michoacan, Mexico, earthquakes, *Geophys. Res. Lett.*, *13*, 609-612, 1986.

Romanowicz, B., M. Cara, J.-F. Fels, and D. Rouland, GEOSCOPE: A

French initiative in long period three component seismic networks, *Eos Trans. AGU, 60*, 753-754, 1984.

Rudnicki, J. W., and C. H. Chen, Stabilization of frictional slip on a weakening fault by dilatant hardening, *J. Geophys. Res., 93*, 4745-4757, 1988.

Rundle, J. B., Viscoelastic crustal deformation by finite quasi-static sources, *J. Geophys. Res., 83*, 5937-5945, 1978.

Sacks, I. S., S. Suyehiro, A. T. Linde, and J. A. Snoke, Slow earthquakes and stress redistribution, *Nature, 275*, 599-602, 1978.

Sacks, I. S., A. T. Linde, J. A. Snoke, and S. Suyehiro, A slow earthquake sequence following the Izu-Oshima earthquake of 1978, in *Earthquake Prediction, an International Review, Maurice Ewing Ser., vol. 4.*, 617-628, AGU, Washington D.C., 1981.

Sailor, R. V., and A. M. Dziewonski, Measurement and interpretation of normal mode attenuation, *Geophys. J. R. Astron. Soc., 53*, 559-582, 1978.

Scholz, C. H., M. Wyss, and S. W. Smith, Seismic and aseismic slip on the San Andreas fault, *J. Geophys. Res., 74*, 2049-2069, 1969.

Scholz, C. H., P. Molnar, and T. Johnson, Detailed studies of frictional sliding of granite and implications for earthquake mechanism, *J. Geophys. Res., 77*, 6392-6406, 1972.

Silver, P. G., and T. H. Jordan, Fundamental spheroidal mode observations of aspherical heterogeneity, *Geophys. J. R. Astron. Soc., 64*, 605-634, 1981.

Silver, P. G., and T. H. Jordan, Optimal estimation of scalar seismic moment, *Geophys. J. R. Astron. Soc., 70*, 755-787, 1982.

Silver, P. G., and T. H. Jordan, Total-moment spectra of fourteen large earthquakes, *J. Geophys. Res., 88*, 3273-3293, 1983.

Smith, S. W., IRIS: A program for the next decade, *Eos Trans AGU. 67*, 213 219, 1986.

Stewart, L. M., and E. A. Okal, Seismicity and aseismic slip along the Eltanin fracture zone, *J. Geophys. Res., 88*, 10,495-10,507, 1983.

Tse, S. T., and J. R. Rice, Earthquake instability in relation to the depth variation of frictional slip properties, *J. Geophys. Res., 91*, 9452-9472, 1986.

Wolf, F. L., *Elements of Probability and Statistics*, p. 192, McGraw-Hill, New York,, 1962.

Yamashita, T., Quasistatic crack extension in an inhomogeneous viscoelastic medium-A possible mechanism for the occurrence of aseismic faulting, *J. Phys. Earth, 28*, 309-326, 1980.

G. C Beroza and T. H. Jordan, Department of Earth, Atmospheric, and Planetary Sciences, Massachusetts Institute of Technology, Cambridge, MA 02139.

(Received February 21, 1989;
revised August 23, 1989;
accepted November 5, 1989.)